The Dissertation Committee for Sean Patrick O'Keefe Certifies that this is the approved version of the following dissertation:

Simple Thermodynamic Modeling of Liquids

Committee:

Isaac C. Sanchez, Supervisor

Thomas M. Truskett

Keith P. Johnston

Ryosuke Okuno

Simple Thermodynamic Modeling of Liquids

by

Sean Patrick O'Keefe, B.S.

Dissertation

Presented to the Faculty of the Graduate School of

The University of Texas at Austin

in Partial Fulfillment

of the Requirements

for the Degree of

Doctor of Philosophy

The University of Texas at Austin

May 2017

Simple Thermodynamic Modeling of Liquids

Sean Patrick O'Keefe, Ph.D.

The University of Texas at Austin, 2017

Supervisor: Isaac C. Sanchez

Theoretical thermodynamic models that accurately capture liquid behavior do so at the cost of ease of use, and do not explicitly reduce to simple relationships observed among liquid properties. Of these relationships, the linear response of liquid density to changes in temperature is one of the simplest and most nearly universal. At low pressures, plots of saturated liquid density vs. temperature are linear over a substantial temperature range. This behavior has been observed for liquids as diverse as monoatomic elements, small organics, molten salts and metals, and polymers. Water and liquid helium are the only known exceptions to this low pressure linearity. This observation is extended to liquid isobars at elevated pressure and to liquid mixtures.

To capture fluid relationships through easily implemented, analytical equations, a model using a Scaled Particle Theory (SPT) for mixtures of hard spheres in a mean-field approximation is developed. Thermodynamic properties are derived from the random insertion of a hard sphere (HS) chain into an HS mixture and invoking random mixing to calculate energetics. The SPT model completely characterizes pure fluids with three independent parameters that can be calculated from pure component properties. Binary mixtures require only one additional interaction parameter, which can be approximated using a geometric mean combining rule or treated as an adjustable parameter. This SPT

chain model is comparable to other thermodynamic models with mean-field configurational energies for mixtures of small, similarly-sized molecules, but yields unsatisfactory results when applied to polymer/solvent systems. The approximations the SPT model makes for the HS chain are investigated as a potential source of error. To improve on the SPT configurational energy approximation, a Quasi-Chemical Square Well (QCSW) model is developed that limits both the attractive range of a given molecular segment and the number of other segments with which it can interact. Though the SPT and QCSW models do not explicitly reduce to a simple isobaric density/temperature relationship, the QCSW model predicts a linear-like regime for saturated liquids at low pressure over an extended temperature range, and introduces promising concepts for modeling liquids.

Table of Contents

List of Tables

List of Figures

Chapter 1: Dimensionless Thermodynamics and Liquids Properties*

Contributions to the configurational entropy of simple saturated liquids correlate well with reduced density ($\rho_R \equiv \rho/\rho_c$)[2]. This correlation suggests that simple saturated liquids should have comparable thermodynamic properties at the same reduced density. The universal dependence of saturated liquid properties on reduced density would be a strong corresponding states principle (CSP); unfortunately, thermodynamic properties that have dimensions do not obey this CSP. If rendered dimensionless by the proper choice of scaling variables, plots of several dimensionless properties vs. ρ_R form "master curves" for classes of liquids, better illustrating corresponding states principles.

1.1 Dimensionless Thermodynamic Properties

A van der Waals (VDW) type model characterized by a configurational energy $(-U)$ that is directly proportional to density ρ is employed for selecting appropriate scaling variables and calculated property comparisons. Equations of state (EOS) for these models have the general form:

$$\begin{aligned} Z = \frac{P}{\rho kT} &= 1 + H_s(\rho) - \frac{U}{KT} \\ &= 1 + H_s(\rho_R) - \frac{\rho_R u}{kT} \end{aligned} \tag{1.1}$$

in which ρ_R is the reduced density $(\rho_R \equiv \rho/\rho_c)$, ρ_c is the critical density, and u is a constant. The function $H_s(\rho_R)$ is the contribution to the EOS from hard sphere repulsion. $H_s(0) = 0$, and $H_s(\rho_R > 0) > 0$. For the classical VDW EOS,

*Much of the material in this chapter was adapted with permission from the original author of: Isaac C. Sanchez, "Dimensionless Thermodynamics: A New Paradigm for Liquid State Properties," *J. Phys. Chem. B* 118 (31), 9386 (2014) [1]. For the present dissertation, Sean Patrick O'Keefe recalculated all numerical values and reorganized material to serve as an introduction to the concepts of simple thermodynamic modeling for liquids and the nearly universal corresponding states behavior of liquid properties. Only material relevant to this specific goal was adapted.

$$Z = 1 + \underbrace{\frac{\rho_R}{3 - \rho_R}}_{H_s(\rho_R)} - \frac{9\rho_R}{8T_R} \tag{1.2}$$

in which the reduced temperature $T_R \equiv T/T_c$, and T_c is the critical temperature.

1.1.1 Cohesive Energy Density

Solving (1.1) for the configurational energy of a VDW liquid gives:

$$\frac{U_{liq}}{kT} = 1 + H_s(\rho) - Z_{liq} \tag{1.3}$$

The normal liquid range (NLR) is here considered the range extending from the triple point to the normal boiling temperatures. For liquids in the NLR, the compressibility factor Z_{liq} is of order 10^{-3} or smaller, and $H_s(\rho_R)$ is of order 10. In the NLR Z_{liq} contributes negligibly to U_{liq}/kT compared to $1 + H_s(\rho_R)$, and (1.3) predicts that dimensionless configurational energy should be completely determined by the reduced density. The saturated vapor in equilibrium with a liquid in the NLR may be approximated as as an ideal gas with no configurational energy. With these approximations the dimensionless energy change of a VDW fluid in the NLR is given by:

$$\frac{\Delta U_{vap}}{kT} \simeq \frac{U_{liq}}{kT} = 1 + H_s(\rho_R) \tag{1.4}$$

For liquid/vapor equilibrium, the thermal contribution to the internal energy cancels when calculating ΔE_{vap} leaving only the contribution from configurational energy changes. The change in configurational energy on vaporization ΔU_{vap} is equal to the change in internal energy on vaporization ΔE_{vap}.

The cohesive energy density (CED or δ^2) is a thermodynamic property used in liquid mixture models. and is closely associated with the vaporization energy. δ^2 is defined as

$$\delta^2 \equiv \frac{U_{liq}}{V} \simeq \rho \Delta U_{vap} \tag{1.5}$$

(1.5) has units of pressure (δ is the well-known Hildebrand solubility parameter). Equations (1.4) and (1.5) suggest rendering the CED dimensionless with the pressure variable ρkT. The resulting dimensionless CED only depends on ρ_R for a VDW type liquid in the NLR:

$$\tilde{\delta}^2 \equiv \frac{\delta^2}{\rho kT} = 1 + H_s(\rho_R) - Z_{liq} = 1 + H_s(\rho_R) \tag{1.6}$$

This dimensionless CED decreases as temperature is increased in the NLR. Figure 1.1 plots the dimensionless CED for common organic liquids including aliphatic and aromatic hydrocarbons and fully halogenated small organics. At the normal boiling point $\tilde{\delta}^2$ reaches a value of 9.2 ± 0.6 in Figure 1.1. The corresponding experimental values of the reduced density at the normal boiling point is $\rho_R = 2.63 \pm 0.07$ for these liquids. ρ_R at the normal boiling points of elemental and very small molecule liquids lie within or nearly within this range, but $\tilde{\delta}^2$ at the normal boiling point for these species is lower. Figure 1.2 shows that $\tilde{\delta}^2$ for these species at $\rho_R = 2.63 \pm 0.07$ is $\tilde{\delta}^2 = 8.0 \pm 0.5$. All experimental data used for figures and tables in this chapter were obtained from the NIST webbook of thermophysical properties of fluid systems http://webbook.nist.gov/chemistry/fluid/ [3].

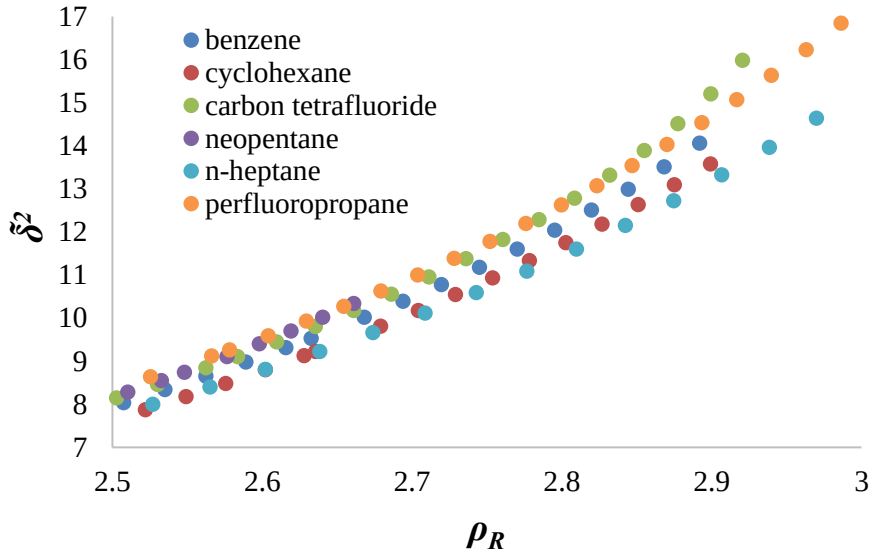

Figure 1.1: Dimensionless cohesive energy density as a function of reduced density for common organic liquids in the NLR

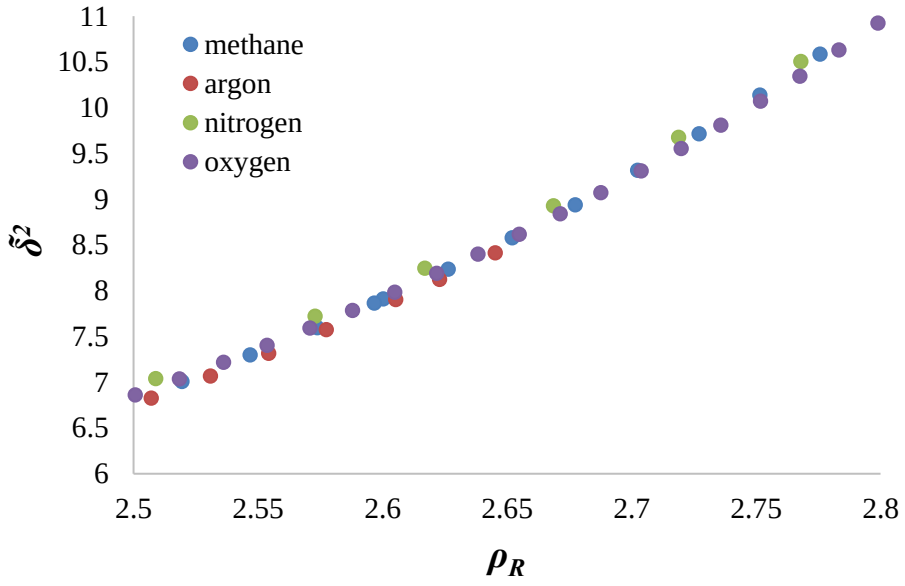

Figure 1.2: Dimensionless cohesive energy density as a function of reduced density for elemental and small molecule liquids in the NLR

1.1.2 Entropy of Vaporization and Trouton's Rule

The entropy and enthalpy of vaporization are given by

$$\frac{\Delta S_{vap}}{k} = \frac{\Delta H_{vap}}{kT} = \frac{\Delta U_{vap}}{kT} + Z_{vap} - Z_{liq} \tag{1.7}$$

In the NLR, $Z_{vap} = 1$ and $Z_{liq} \simeq 0$ so that for a VDW type liquid:

$$\frac{\Delta S_{vap}}{k} = 1 + \frac{\Delta U_{vap}}{kT} \simeq 1 + \tilde{\delta}^2 = 2 + H_s(\rho_R) \tag{1.8}$$

Substituting $\tilde{\delta}^2 = 9.2 \pm 0.6$ into (1.8) gives

$$\frac{\Delta S_{vap}}{k} = 10.2 \pm 0.6 \tag{1.9}$$

which is Trouton's rule at the normal boiling point.

Trouton's rule does not apply to two well-known classes of fluid, some hydrogen bonding liquids, and very small monoatomic and diatomic molecules. The hydrogen bonding liquid exceptions yield $\Delta S_{vap}/k > 11$, and the very small molecules yield$\Delta S_{vap}/k < 9.5$. For this reason, it is convenient to define 3 broad liquid groups by either their dimensional vaporization entropies at their normal boiling points or Trouton's constant $\left(\Delta S_{vap}/k\right)$:

$$\frac{\Delta S_{vap}}{k} = \begin{cases} 8.5 \text{ to } 9.5 & \text{Group I} \\ 9.8 \text{ to} 10.8 & \text{Group II} \\ > 11.2 & \text{Group III} \end{cases}$$

Ranges don't overlap, as some liquids do not neatly fall into these categories. Group I includes the inert elements and diatomic molecules given in Table 1.1. Group II

includes non-polar and slightly polar organic liquids given in Tables 1.2–1.4. Group III liquids include many polar and hydrogen bonding liquids such as alcohols. Water is in its own unique group. Group I and Group II share some thermodynamic properties, yet show a clear difference for other properties. Dimensionless entropies of vaporization are plotted in Figure 1.3 for some Group II liquids. The superposition of ΔS_{vap} vs. ρ_R plots illustrates a generalized Trouton's rule. Many Group II liquids at their normal boiling points have reduced densities of $\rho_R = 2.63 \pm 0.07$, which corresponds to a $\Delta S_{vap}/k \sim 10$ (Trouton's constant), but at $\rho_R = 2$, Trouton's constant would be about five.

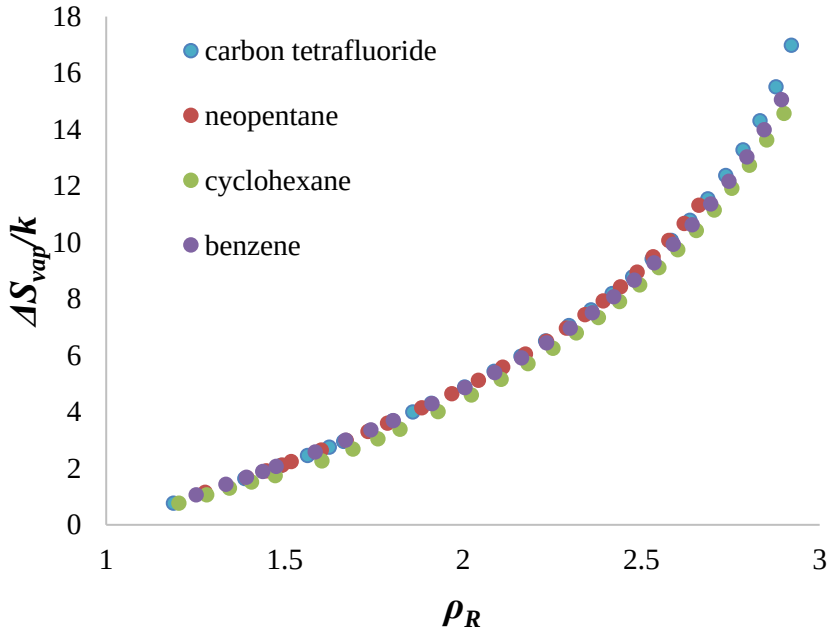

Figure 1.3: Entropies of vaporization for some Group II molecules.

Condensation of the saturated vapor approximated as an ideal gas at P^{sat}/kT to the liquid state can be thought of as requiring two steps: first, the compression of the

ideal gas from a density of $\rho_{ig} = P^{sat}/kT$ to an ideal gas at the same density as the liquid ρ_{liq} followed by "turning on the interactions" to convert the dense ideal gas to a liquid with the density ρ_{liq}. The second contribution to the entropy of condensation is the self-solvation entropy ΔS_p. The first contribution ΔS_{cond} is easily calculated as the isothermal compression of an ideal gas:

$$\frac{\Delta S_{cond}}{k} = \ln\left(\frac{\rho_{ig}}{\rho_{liq}}\right) = \ln\left(\frac{kT\rho_{ig}/P^{sat}}{kT\rho_{liq}/P^{sat}}\right) = \ln Z_{liq} - \ln Z_{ig} = \ln Z_{liq} < 0 \qquad (1.10)$$

Since ΔS_{vap} and Z_{liq} are experimental measurables, the self-solvation entropy ΔS_p can be calculated from the thermodynamic cycle:

$$\Delta S_{vap} + \Delta S_{cond} + \Delta S_p = 0 \qquad (1.11)$$

Self-solvation entropy has been described as the entropy loss of transferring a molecule at a fixed position in an ideal gas to a fixed position in a liquid of density ρ_{liq}.[4,5] Since the molecule is fixed in space before and after the transfer, there are no entropic contributions associated with changes in molecular translational degrees of freedom; ΔS_p isolates the entropy contribution of molecular interactions in the solvation process.

1.1.3 Chemical Potential

The chemical potential relative to an ideal gas at the same temperature and pressure may be computed from the equation of state by [6]:

$$\mu - \mu_{ig}(T,P) = Z - 1 - \ln Z + \int_0^{\rho_R} \frac{Z-1}{\rho} d\rho \qquad (1.12)$$

For a saturated liquid in equilibrium with an ideal gas, (1.12) is identically zero. Substituting the EOS (1.1) into (1.12) and rearranging yields:

$$\ln Z_{liq} = H_s(\rho_R) - 2\frac{\rho_R u}{kT} + \int_0^{\rho_R} \frac{H_s(\rho)}{\rho} d\rho \tag{1.13}$$

In the NLR, setting $Z_{liq} \simeq 0$, and solving for the potential energy contribution gives:

$$\ln Z_{liq} = -2 - H_s(\rho_R) + \int_0^{\rho_R} \frac{H_s(\rho)}{\rho} d\rho \tag{1.14}$$

Equation (1.14) predicts that in the NLR, Z_{liq} depends only on ρ_R. The validity of this conclusion is illustrated in Figure 1.4. Superposition of $\ln Z_{liq}$ vs. ρ_R data persists to the critical point where the vapor may not be approximated as an ideal gas [7].

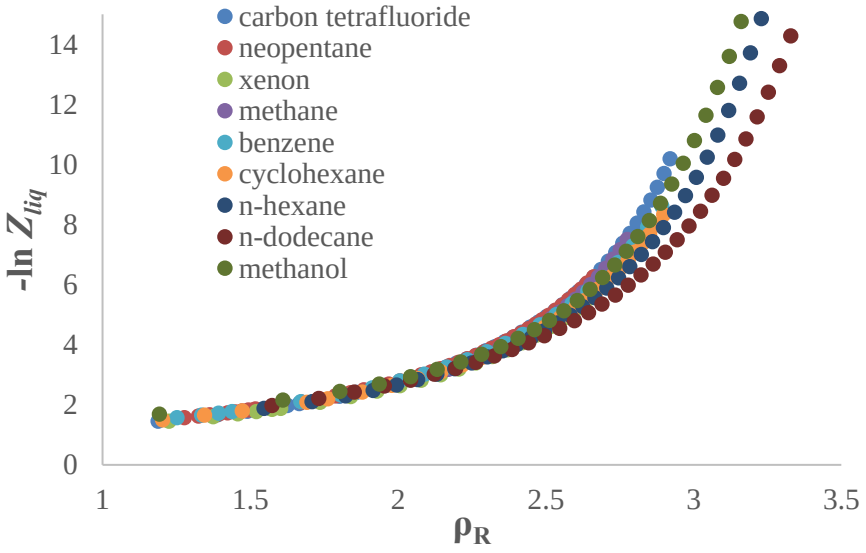

Figure 1.4: Behavior of the logarithm of liquid compressibility factor $-k \ln Z_{liq}$ for different types of liquids.

1.1.4 Thermal Expansion, Isothermal Compressibility, & Thermal Pressure

The thermal expansion coefficient and isothermal compressibility can be calculated from equation (1.1) in the NLR ($Z_{liq} \simeq 0; u/kT \simeq 1 + H_s(\rho_R)$):

$$\tilde{\alpha} \equiv T\alpha = -T \left.\frac{\partial \ln \rho_R}{\partial T}\right)_P = \frac{1 + H_s(\rho_R)}{\rho_R \frac{dH_s(\rho_R)}{d\rho_R} - 1 - H_s(\rho_R)} \tag{1.15}$$

$$\tilde{\kappa} \equiv (kT\rho)\kappa = \rho kT \left.\frac{\partial \ln \rho_R}{\partial P}\right)_T = \left[\left(\frac{\partial \rho_R Z}{\partial \rho_R}\right)_T\right]^{-1} = \frac{1}{\rho_R \frac{dH_s(\rho_R)}{d\rho_R} - 1 - H_s(\rho_R)} \tag{1.16}$$

Both $\tilde{\alpha}$ and $\tilde{\kappa}$ depend only on ρ_R in the NLR.

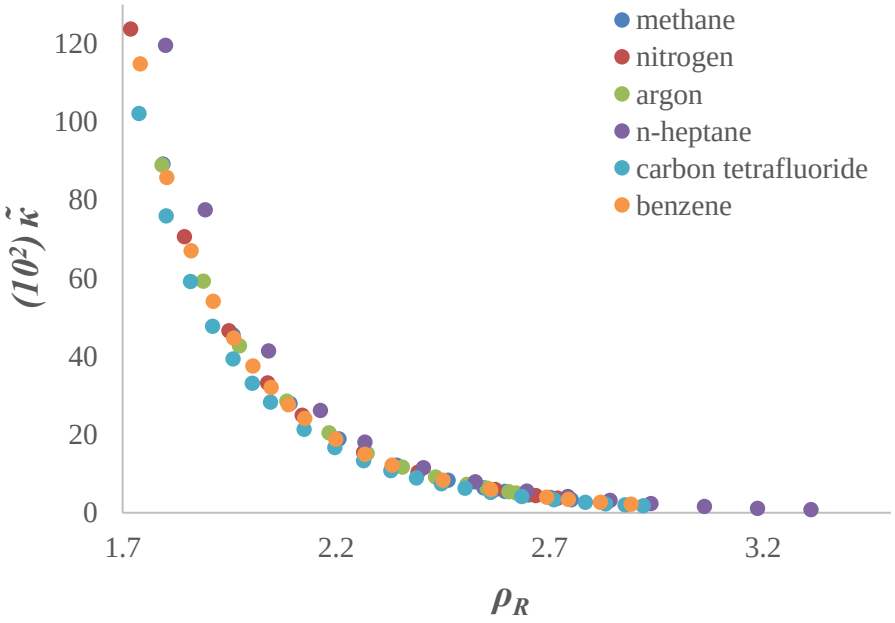

Figure 1.5: Dimensionless isothermal compressibility vs. reduced density

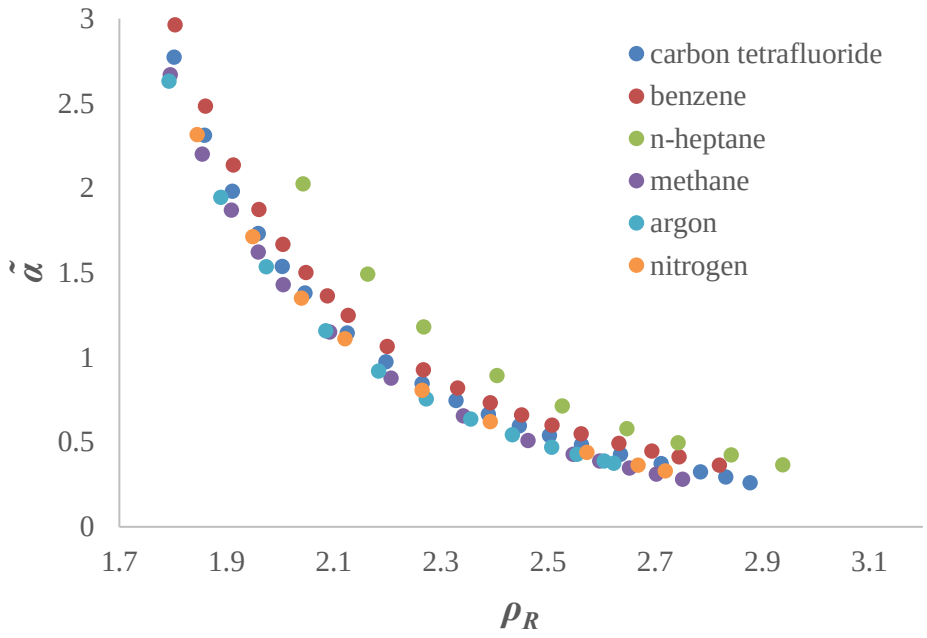

Figure 1.6: Dimensionless thermal expansion coefficient vs. reduced density

In Figure 1.5, $\tilde{\kappa}$ is plotted against ρ_R. For $\tilde{\kappa}$, both Group I and II molecules nearly follow the same universal curve, but Figure 1.6 shows that larger molecule liquids tend toward larger $\tilde{\alpha}$ at a given ρ_R.

The thermal pressure coefficient is given by:

$$\gamma_v = \frac{\partial P}{\partial T}\Big)_V = \frac{\alpha}{\kappa}$$
$$\tilde{\gamma}_v = \frac{T\alpha}{(kt\rho)\kappa} = \frac{\tilde{\alpha}}{\tilde{\kappa}} = 1 + H_s(\rho_R) \tag{1.17}$$

In the NLR where $Z_{liq} \simeq 0$, $\tilde{\delta}^2$ and $\tilde{\gamma}_v$ are equal to one another. This result only holds if configurational energy is directly proportional to density. $\tilde{\gamma}_v$ is plotted in Figure 1.7. Groups I and II form separate, distinct branches.

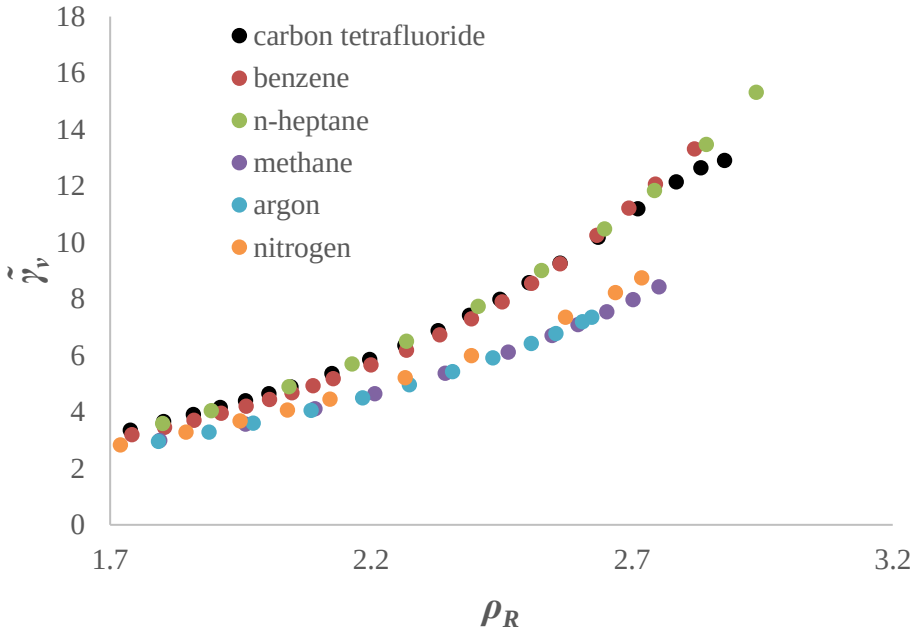

Figure 1.7: Dimensionless thermal pressure coefficient as a function of reduced density

1.1.5 Surface Tension

There is no explicit thermodynamic relation to guide in the selection of a scaling variable to render the surface tension (σ) dimensionless. Some applications of Cahn-Hilliard theory[8,9] indicate calculating surface tension through integrating the Helmholtz free energy density (which has units of pressure) over a characteristic interfacial distance. As with CED, Helmholtz free energy densities scale as ρkT, while interfacial distance scales as $\rho^{-1/3}$; therefore, a dimensionless surface tension $\tilde{\sigma}$ can be defined as:

$$\tilde{\sigma} = \frac{\sigma}{kT\rho^{2/3}} \tag{1.18}$$

$\tilde{\sigma}$ is plotted against ρ_R in Figure 1.8. While a wide variety of non-polar liquids show satisfactory superposition, Group I liquids $\tilde{\sigma}$ are 10 to 20% greater than Group II liquids.

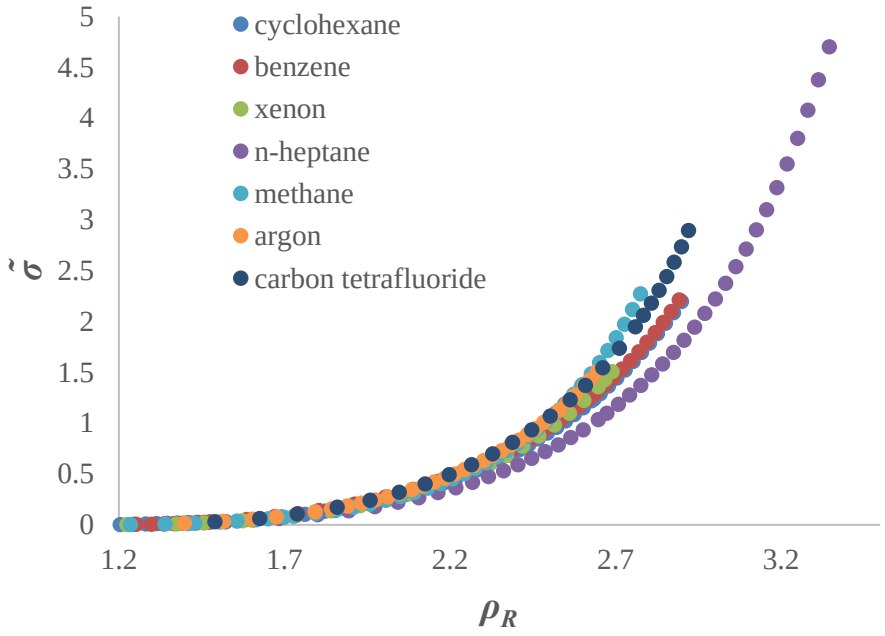

Figure 1.8: Dimensionless surface tension as a function of reduced density

1.2 Model Comparisons with Experimental Data

In Chapter 2, a VDW model is described based on Scaled Particle Theory (SPT) for hard spheres [10,11]. Since molecules discussed thus far are relatively small (compared to polymers), they will be treated as single spheres (for the purposes of Chapter 1 only). In the NLR, thermodynamic properties of saturated liquids only depend on a single variable, the occupied volume fraction $\eta = \eta_c \rho_R$, in which η is the occupied volume fraction, and η_c is the critical occupied volume fraction. For unchained SPT spheres with configurational energy proportional to density, the derived critical occupied volume fraction $\eta_c = 0.1287$.

Using $\eta_c = 0.1287$ to predict experimental entropies of vaporization consistently underestimates ΔS_{vap}. Alternately, η_c can be treated as an adjustable parameter chosen to

yield the correct value of a given property. Figure 1.3 shows that $\Delta S_{cond} = k \ln Z_{liq}$ dependence on ρ_R appears to be more universal than ΔS_{vap} even including Group III liquids such as methanol. Through equation (1.14) η_c is therefore adjusted to yield the correct value of ΔS_{cond} at the normal boiling point for a given liquid. This adjusted value of η_c is then used to predict all other thermodynamic properties in this chapter. Figure 1.9 compares the compressibility factor of liquid oxygen as a function of ρ_R calculated with the $\eta_c = 0.1287$ and the value of $\eta_c = 0.159$, adjusted to match Z_{liq} at oxygen's normal boiling point. $\eta_c = 0.1287$ overestimates Z_{liq} in the NLR. Values of η_c determined this way are shown for several liquids in Tables 1.1–1.4.

For the Group I liquids in Table 1, η_c is bounded tightly.

$$0.156 \leq \eta_c \leq 0.160$$

From computer simulations, the critical density $\rho_c \sigma^3$ of a Lennard-Jones (LJ) fluid has been estimated between 0.29 and 0.31 [12–14]. Taking σ as the effective diameter of the LJ particle, the fraction of space occupied by an LJ fluid at the critical occupied density $\eta_c(LJ)$ is:

$$0.152 \leq \eta_c(LJ) \leq 0.160$$

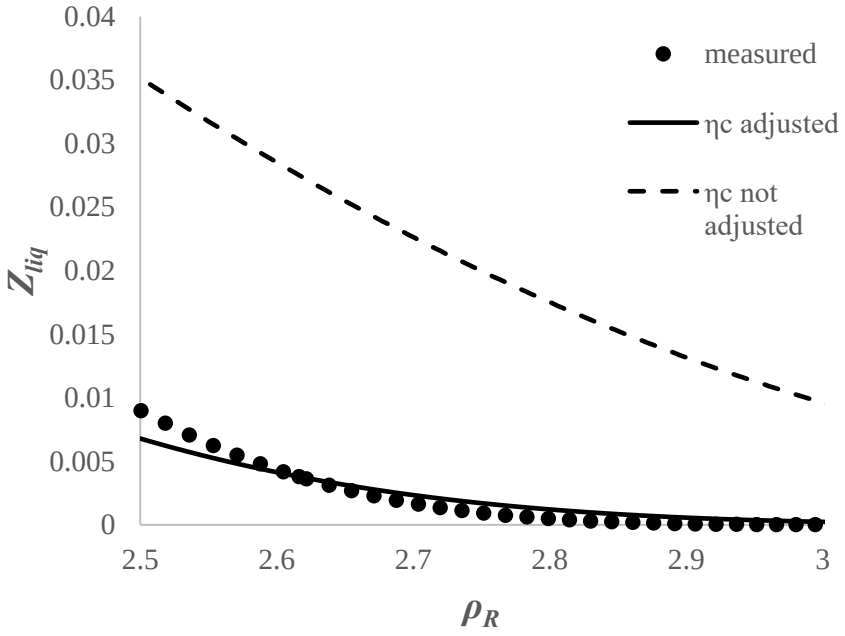

Figure 1.9: Compressibility factor calculated for the mean-filed SPT unchained sphere model for oxygen in the NLR.

With η_c rescaled to match ΔS_{cond} other thermodynamic properties are calculated. Properties in Table 1.1 show good agreement between calculated and experimental vaporization (ΔS_{vap}) and self-solvation (ΔS_p) entropies. Because $\tilde{\delta}^2$ depends on ΔS_{vap} as given in equations (1.7) and (1.8), the agreement between experimental $\tilde{\delta}^2$ and $\tilde{\delta}^2$ calculated with this SPT model for Group I liquids is good. For comparison an LJ fluid has at its normal boiling point[2]:

$$\Delta S_{vap}/k = 8.9 \text{ at } \rho_R = 2.63$$

which agrees well with the Group I liquids in Table 1.1.

		N_2	CO	Ar	O_2	CH_4	Xe
critical temperature	T_c(K)	126.192	132.86	150.69	154.58	190.56	289.73
critical volume	V_c(cm^3/mol)	89.4	92.2	74.6	73.4	98.6	119.0
normal boiling temperature	T_b(K)	77.4	81.6	87.3	90.2	111.7	165.1
volume at T_b	V_b(cm^3/mol)	34.8	35.3	28.6	28.0	38.0	44.6
	ρ_R	2.57	2.61	2.61	2.62	2.60	2.67
	$-\ln Z_{liq}$	5.21	5.25	5.52	5.58	5.49	5.72
η_c	adjusted	0.158	0.156	0.160	0.159	0.160	0.158
η_b	calcd	0.406	0.407	0.416	0.417	0.415	0.421
$\Delta S_{vap}/k$	exptl	8.7	8.9	8.9	9.1	8.8	9.1
	calcd	8.5	8.5	9.0	9.0	8.9	9.2
$-\Delta S_p/k$	exptl	3.5	3.6	3.3	3.5	3.3	3.4
	calcd	3.3	3.3	3.4	3.5	3.4	3.5
$\tilde{\delta}^2$	exptl	7.7	7.9	7.9	8.1	7.9	8.2
	calcd	7.5	7.5	8.0	8.0	7.9	8.2
$\tilde{\alpha}$	exptl	0.44	0.45	0.39	0.39	0.39	0.38
	calcd	0.66	0.65	0.62	0.61	0.62	0.60
$(10^2)\tilde{\kappa}$	exptl	6.0	6.1	5.4	5.2	5.5	5.2
	calcd	8.8	8.7	7.8	7.6	7.9	7.3
$\tilde{\gamma}_v$	exptl	7.35	7.47	7.20	7.52	7.09	7.28
	calcd	7.49	7.55	7.96	8.04	7.91	8.25
$\tilde{\sigma}$	exptl	1.2	1.3	1.4	1.4	1.4	1.4
$(10^2)\tilde{\kappa}\tilde{\sigma}$	exptl	7.4	7.7	7.4	7.2	7.5	7.4

Table 1.1: Experimental comparisons of SPT model with Group I small molecules at their normal boiling points.

This SPT VDW model for unchained spheres was less successful at calculating some second order properties of Group I liquids. The model consistently overestimates dimensionless isothermal compressibility and thermal expansion coefficient for Group I liquids by as much as 50%. The ratio of the two, $\tilde{\gamma}_v$, is accurately predicted. Table 1.1 shows that for Group I liquids, the experimental values of the dimensionless thermal pressure coefficient ($\tilde{\gamma}_v$) and CED $\left(\tilde{\delta}^2\right)$ agree with one another, consistent with NLR

properties for a model that assumes a linear dependency of configurational energy on density.

		Propene	C_3H_8	n-C_4H_{10}	$C(CH_3)_4$
critical temperature	T_c(K)	365.57	369.825	425.125	433.74
critical volume	V_c(cm3/mol)	188.4	200.0	254.92	305.81
normal boiling temperature	T_b (K)	225.5	231.0	272.66	282.65
volume at T_b	V_b(cm^3/mol)	69.1	75.9	96.67	120.01
	ρ_R	2.7	2.6	2.64	2.55
	$-\ln Z_{liq}$	5.6	5.5	5.44	5.26
η_c	adjusted	0.2	0.2	0.16	0.16
η_b	calcd	0.4	0.4	0.41	0.41
ΔS_{vap}	exptl	9.9	9.8	9.89	9.69
	calcd	9.06	8.96	8.84	8.57
$-\Delta S_p/k$	exptl	4.27	4.26	4.44	4.43
	calcd	3.47	3.44	3.40	3.31
$\tilde{\delta}^2$	exptl	8.90	8.82	8.93	8.74
	calcd	8.06	7.96	7.84	7.57
$\tilde{\alpha}$	exptl	0.46	0.46	0.49	0.50
	calcd	0.61	0.62	0.63	0.65
$(10^2)\tilde{\kappa}$	exptl	5.2	5.0	5.1	5.1
	calcd	7.6	7.8	8.0	8.6
$\tilde{\gamma}_v$	exptl	8.89	9.16	9.59	9.84
	calcd	8.06	7.96	7.84	7.57
$\tilde{\sigma}$	exptl	1.3	1.2	1.2	—
$(10^2)\tilde{\kappa}\tilde{\sigma}$	exptl	6.6	6.3	6.0	—

Table 1.2: Experimental comparisons of SPT model with aliphatic hydrocarbons at their normal boiling points

Group II liquid properties are shown in Tables 1.2–1.4. Like Group I liquids, the adjusted η_c vary little from one liquid to the other:

$$0.153 \leq \eta_c \leq 0.160$$

The calculated Group II $\Delta S_{vap}/k$ and $\Delta S_p/k$ are lower than their measured values by about 1 to 2. The discrepancy increases as molecular size increases. The experimental ΔS_p values indicate that Group II liquids, which occupy larger molecular volumes than Group I, pay a larger entropic penalty in self-solvation. With regards to entropy changes, and other energetic properties like the CED, the SPT model for unchained spherical molecules is adequate for small Group I molecules, but not for Group II molecules.

		n-C_6H_{14}	C_6H_6	$(CH_2)_6$	n-C_7H1_6	$CH_3C_6H_5$
critical temperature	T_c (K)	507.82	562.05	553.64	540.13	591.75
critical volume	V_c(cm^3/mol)	369.6	252.8	308.3	431.9	315.6
normal boiling temperature	T_b (K)	341.9	353.2	353.9	371.5	383.7
volume at T_b	V_b(cm^3/mol)	140.6	96.0	117.0	163.1	118.3
	ρ_R	2.63	2.63	2.64	2.65	2.67
	$-\ln Z_{liq}$	5.30	5.71	5.51	5.23	5.58
η_c	adjusted	0.155	0.160	0.158	0.154	0.156
η_b	calcd	0.409	0.421	0.415	0.407	0.417
$\Delta S_{vap}/k$	exptl	10.2	10.5	10.2	10.3	10.4
	calcd	8.6	9.2	8.9	8.5	9.1
$-\Delta S_p/k$	exptl	4.9	4.8	4.7	5.0	4.8
	calcd	3.3	3.5	3.4	3.3	3.5
$\tilde{\delta}^2$	exptl	9.2	9.5	9.2	9.3	9.5
	calcd	7.6	8.2	7.9	7.5	8.1
$\tilde{\alpha}$	exptl	0.56	0.49	0.50	0.58	0.51
	calcd	0.65	0.60	0.62	0.66	0.61
$(10^2)\tilde{\kappa}$	exptl	5.6	4.8	4.8	5.5	4.9
	calcd	8.5	7.3	7.8	8.7	7.6
$\tilde{\gamma}_v$	exptl	10.03	10.25	10.43	10.48	10.32
	calcd	7.62	8.24	7.95	7.52	8.05
$\tilde{\sigma}$	exptl	1.1	1.3	1.2	1.0	1.1
$(10^2)\tilde{\kappa}\tilde{\sigma}$	exptl	5.9	6.1	5.9	5.7	5.6

Table 1.3: Experimental comparisons of SPT model with aliphatic and aromatic hydrocarbons at their normal boiling points

		CCl_3F	CCl_2F_2	$CClF_3$	CF_4	C_2F_6	C_3F_8
critical temperature	Tc (K)	471.11	385.12	302	227.51	293.03	345.02
critical volume	V_c(cm^3/mol)	248.0	214.0	179.2	140.7	225.0	299.4
normal boiling temperature	T_b (K)	296.9	243.4	191.7	145.1	195.1	236.4
volume at T_b	V_b(cm^3/mol)	92.9	81.3	68.7	54.9	86.0	116.7
	ρ_R	2.67	2.63	2.61	2.56	2.62	2.57
	$-\ln Z_{liq}$	5.57	5.50	5.43	5.38	5.23	5.11
η_c	adjusted	0.156	0.158	0.158	0.161	0.155	0.157
η_b	calcd	0.417	0.415	0.413	0.411	0.406	0.403
$\Delta S_{vap}/k$	exptl	10.1	9.9	9.8	9.8	10.0	10.1
	calcd	9.0	8.9	8.8	8.7	8.5	8.3
$-\Delta S_p/k$	exptl	4.5	4.4	4.4	4.4	4.7	4.9
	calcd	3.5	3.4	3.4	3.4	3.3	3.2
$\tilde{\delta}^2$	exptl	9.1	9.0	8.8	8.8	9.0	9.1
	calcd	8.0	7.9	7.8	7.7	7.5	7.3
$\tilde{\alpha}$	exptl	0.48	0.48	0.49	0.49	0.54	0.58
	calcd	0.61	0.62	0.63	0.64	0.66	0.67
$(10^2)\tilde{\kappa}$	exptl	4.9	4.9	5.3	5.2	5.6	5.1
	calcd	7.7	7.8	8.0	8.2	8.7	9.1
$\tilde{\gamma}_v$	exptl	9.77	9.78	9.26	9.27	9.61	11.32
	calcd	8.03	7.93	7.83	7.75	7.52	7.35
$\tilde{\sigma}$	exptl	1.3	1.2	1.2	1.2	1.1	1.1
$(10^2)\tilde{\kappa}\tilde{\sigma}$	exptl	6.1	6.1	6.5	6.4	6.3	5.5

Table 1.4: Experimental comparisons of SPT model with halogenated hydrocarbons at their normal boiling points

The calculated η_B for Group II liquids average 0.412, which does not statistically differ from the average η_B for Group I liquids (0.415). As with the Group I liquids, this model overestimates $\tilde{\alpha}$ and $\tilde{\kappa}$ by about 50%, But unlike Group I, it does not accurately calculate $\tilde{\gamma}_v$. The discrepancy generally increases with molecular size. For Group II liquids, experimentally $\tilde{\gamma}_v > \tilde{\delta}^2$. $\tilde{\gamma}_v - \tilde{\delta}^2$ increases as molecular size increases.

Figures 1.5 and 1.8 show that both $\tilde{\kappa}$ and $\tilde{\sigma}$ satisfy a CSP; therefore, their product also satisfies a CSP:

$$\tilde{\kappa}\tilde{\sigma} = \rho^{1/3}\kappa\sigma \tag{1.19}$$

This experimental product is given in the tables. The $\kappa\sigma$ product, has units of length, and has recognized as a fundamental length scale for liquids[15]. $\kappa\sigma$ varies as $V^{1/3} \propto \rho^{-1/3}$ which is a measure of the average distance between molecules.

1.3 SUMMARY AND CONCLUSIONS

Thermodynamic properties can be rendered dimensionless with properly chosen scaling variables. For most properties, these variables are those which a generic VDW model suggests to reduce a given property to a function of reduced density in the NLR. This controlling nature of density in determining liquid properties yields the following corresponding states principle: liquids at the same reduced density ρ_R have comparable dimensionless thermodynamic properties. At low pressures, for a generic VDW model, temperature can be eliminated explicitly via the EOS by setting $Z_{liq} = 0$. For these models, ρ_R becomes the only variable governing the thermodynamic properties of liquids in the NLR.

Depending on $\Delta S_{vap}/k$, liquids can be classified into 3 general groups. Group I includes small molecules such as monoatomic elements, diatomic elements, and methane. Group II includes slightly larger non-polar and slightly polar organics such as those in Tables 1.2–1.4. Group III includes polar and hydrogen bonding liquids. Some thermodynamic properties of both Group I and II superpose to form "master curves," such as $\tilde{\kappa}$ and $-\ln Z_{liq}$, while other properties split into branches such as $\tilde{\alpha}$ and γ_v. Isothermal compressibility may be the most universal property among Groups I and II.

Among the liquids listed in Tables 1.1–1.4, the average experimental value of $\tilde{\kappa}$ at their normal boiling points is $(5.1 \pm 0.1)\times 10^{-2}$. A similar small variation is also observed in $-\ln Z_{liq} = \Delta S_{cond}/k$.

Using critical occupied volume fraction as the only adjustable parameter, the dimensionless thermodynamic properties are calculated at the normal boiling point with a VDW type model based on Scaled Particle Theory for hard spheres. Excellent agreement is obtained for some properties of Group I liquids. These properties for small molecules calculated with this model also agree well with computed Lennard-Jones properties.

Overall, this SPT model for small, rigid, unchained spheres is unsuitable for large flexible molecules such as n-heptane. At their normal boiling points, the experimental $\Delta S_p/k$ shown in the tables are larger in magnitude for Group II liquids than for Group I liquids, yet the $\Delta S_p/k$ calculated with this model do not show this trend. The SPT model developed and described in Chapter 2–4 addresses this issue by introducing a parameter (r) to account for molecular size differences.

Chapter 2: Scaled Particle Theory of Molecular and Polymer Solutions*

2.1 INTRODUCTION

The analytically simple, easily implemented Lattice Fluid (LF) model[17–19] remains popular in thermodynamic modeling of polymer fluids and polymer/solvent solutions[20–23]. Newer, more complex models yield accurate calculated properties[24,25] and can provide structural information[26,27], but at the cost of practicality. As an example, most implementations of Statistical Associating Fluid Theory (SAFT) require five pure component parameters[28] compared to LF's three, and SAFT chemical potentials are much more complicated than corresponding expressions for LF chemical potentials[18,29]. Some models that emphasize structure have difficult and inaccurate equations of state[30]. The enduring popularity of the LF model may be attributed to its robustness in calculating fluid properties of all sizes, its statistical thermodynamic foundation, and its relative ease of use; however, the LF model is built upon a lattice description of a fluid, which has obvious limitations in its ability to describe a fluid from a molecular viewpoint.

Scaled Particle Theory (SPT) is an off-lattice model shown to accurately predict thermodynamic properties of hard sphere (HS) mixtures[31]. As demonstrated in Chapter 1, adding a random mixing approximation to calculate potential energy (mean-field or van der Waals approximation) has shown useful in calculating some properties of small, elemental and rigid liquids[1]. A mean-field type argument is also invoked to derive the insertion probability for a tangent HS chain with SPT as an individual sphere template. The combination of insertion probability and potential energy allows the calculation of the chemical potential and other thermodynamic properties. Size and

* This material was partly published as: Sean P. O'Keefe, and Isaac C. Sanchez, "Scaled Particle Theory of solutions: Comparison with Lattice Fluid Model" *Fluid Phase Equilibria* 433, 67 (2017)[16]. Sean Patrick O'Keefe is the primary author.

energetic parameters for this SPT model are equal in number and similar in interpretation to the LF parameters. Like the LF model, the SPT model is easy to use and does not require much computing effort. Unlike the LF model, the SPT molecular description is an off-lattice model that strictly defines segment sizes.

2.2 SPT Chain Model Description

A molecule of type i is modeled as a chain of r_i tangent hard spheres of diameter σ_i (pearl necklace model). Both r_i and σ_i are characteristic properties of the molecule independent of temperature and pressure. The volume occupied by a single i molecule is $r_i\pi\sigma_i^3/6 \equiv r_i v_i^*$. The two independent molecular size parameters, $v_i^* = \pi\sigma_i^3/6$ and r_i are analogous to the LF segment volume v_i^* and chain length r_i^0 parameters given in [18,19]. For an m-component system of volume V containing N_1 molecules of type 1, N_2 molecules of type 2… N_m molecules of type m, $N = \sum_{i=1}^{m} N_i$, the HS volume is assumed additive, and occupied volume fraction η is defined by:

$$\eta = \frac{\sum_i^m N_i r_i v_i^*}{V} = \frac{V^*}{V} \tag{2.1}$$

Like $\tilde{\rho}$ in the LF model, η is a ratio of occupied to total volume and functions as a reduced density.

2.2.1 Chemical Potential

The chemical potential of species i (μ_i) can be expressed as[32]:

$$\mu_i = kT \ln(\phi_i \eta / r_i v_i^* q_i \mathbf{B}_i) \tag{2.2}$$

where k is the Boltzmann constant, T is the system temperature, q_i is the internal molecular partition function assumed to be at most a function of T (and hereafter, suppressed), and $\mathbf{B}_i$ is the dimensionless Widom insertion factor for the chain. ϕ_i is the fraction of the total HS volume occupied by species i:

$$\phi_i = \frac{N_i r_i v_i^*}{V}; \quad \eta_i = \phi_i \eta \tag{2.3}$$

For a HS fluid in a mean-field approximation in which fluctuations in the energy are ignored, $\mathbf{B}_i$ is given by[2]:

$$\ln \mathbf{B}_i = \ln \mathbf{P}_i - \beta \langle \psi_i \rangle \tag{2.4}$$

$\beta = 1/kT$, $\langle \psi_i \rangle$ is the average attractive energy of a HS chain of type i with all other molecules in the system, and $\mathbf{P}_i$ is the probability of a successful random insertion of a chain of r_i hard spheres into the HS system at once. $\mathbf{P}_i$ can be approximated as the product of inserting each sphere of the chain of r_i spheres independently into the mixture. With $\mathbf{P}_{1i}$ as the probability of inserting a single HS of diameter σ_i into the system, this approximation yields:

$$\mathbf{P}_i = \mathbf{P}_{HS,i}^{r_i} \tag{2.5}$$

Equation (2.5) completely ignores chain connectivity. If $\mathbf{P}_{HS,i}$ were known exactly, the approximate $\mathbf{P}_i$ calculated from an exact $\mathbf{P}_{HS,i}$ using (4) would overestimate the insertion probability since it does not require the more stringent condition that r_i contiguous sites be available for a successful insertion.

According to SPT[31]:

$$-\ln \mathbf{P}_{HS,i} = \ln(1+y) + (3\sigma_{-1}\sigma_i + 3\sigma_{-2}\sigma_i^2 + \sigma_{-3}\sigma_i^3)y + \left(\frac{9}{2}\sigma_{-1}^2\sigma_i^2 + 3\sigma_{-1}\sigma_{-2}\sigma_i^3\right)y^2 + 3\sigma_{-1}^3\sigma_i^3 y^3 \tag{2.6}$$

in which

$$\sigma_{-k} = \sum_i \frac{\phi_i}{\sigma_i^k} \tag{2.7}$$

and

$$y = \frac{\eta}{1-\eta}; \quad \eta = \frac{y}{1+y} \tag{2.8}$$

The mean-field potential energy is identical to that given for the LF model in[19]. Assuming that hard spheres interact attractively with one another through a R^{-6} potential of the form $\varepsilon_{ij}(\sigma_{ij}/R)^6$, the average interaction energy of a molecule of type i with a system of attractive spheres is given by:

$$\langle \psi_i \rangle = -2r_i v_i^* \eta \sum_j \phi_j P_{ij}^* \tag{2.9}$$

where

$$P_{ij}^* = 4\left(\frac{\sigma_{ij}^3}{\sigma_{ii}^*\sigma_{jj}^3}\right)\varepsilon_{ij} \quad \text{and} \quad P_{ii}^* = P_i^* = \frac{2\pi\varepsilon_{ii}/3}{\pi\sigma_{ii}^3/6} \equiv \frac{\varepsilon_i^*}{v_i^*} \tag{2.10}$$

P_{ij}^* is a temperature independent parameter with units of pressure that measures how strongly an i sphere attracts a j sphere.

Using equations (2.2–2.10) the chemical potential of species i is given by:

$$\beta\mu_i = \ln\underbrace{\left(\frac{\phi_i\eta}{r_i v_i^*}\right)}_{N_i/V=\rho_i} + r_i\begin{bmatrix}\ln(1+y) + (3\sigma_{-1}\sigma_i + 3\sigma_{-2}\sigma_i^2 + \sigma_{-3}\sigma_i^3)y \\ +\left(\frac{9}{2}\sigma_{-1}^2\sigma_i^2 + 3\sigma_{-1}\sigma_{-2}\sigma_i^3\right)y^2 \\ +3\sigma_{-1}^3\sigma_i^3 y^3 - 2\beta v_i^*\eta\sum_j \phi_j P_{ij}^*\end{bmatrix} \tag{2.11}$$

Equation (2.11) satisfies the Gibbs-Duhem requirement that $\sum_i N_i\mu_i = 0$ at a fixed temperature and pressure.

2.2.2 Equation of State

If the chemical potential is known to within a function of temperature, the equation of state may be found through isothermal integrations of the Gibbs-Duhem equation[6] by:

$$Z \equiv \frac{P}{\rho kT} = 1 - \ln\mathbf{B} + \frac{1}{\eta}\int_0^\eta \ln\mathbf{B}\, d\eta \tag{2.12}$$

$$\ln\mathbf{B} = \sum_i x_i \ln\mathbf{B}_i \tag{2.13}$$

in which x_i are mole/number fractions. Equation (2.12) yields the following EOS for the system of SPT chains:

$$\frac{Z}{r} = \frac{\tilde{P}}{\eta\tilde{T}} = \frac{(1+y)(\sigma_{-3} + 3\sigma_{-1}\sigma_{-2}y + 3\sigma_{-1}^3\, y^2)}{\sigma_{-3}} - \left(1 - \frac{1}{r}\right) - \frac{\eta}{\tilde{T}}$$
$$\tilde{P} \equiv P/P^* \quad P^* = \sum_i\sum_j \phi_i\phi_j P_{ij}^* \tag{2.14}$$
$$\tilde{T} \equiv T/T^* \qquad T^* = P^* v^*/k$$

r is the number average chain length of the SPT chain mixture:

$$r = \sum_i x_i r_i \tag{2.15}$$

and v^* is the average sphere volume in the mixture given by:

$$v^* = \frac{\sum_i N_i r_i v_i^*}{\sum_i N_i r_i} = \frac{V^*}{rN} \quad \text{or equivalently} \quad \frac{1}{v^*} = \sum_i \frac{\phi_i}{v_i^*} = \frac{6\sigma_{-3}}{\pi} \tag{2.16}$$

For pure fluids (2.14) reduces to:

$$\frac{\tilde{P}}{\eta \tilde{T}} = \frac{1}{r} + 4y + 6y^2 + 3y^3 - \frac{\eta}{\tilde{T}} \tag{2.17}$$

and the ideal gas law: $\frac{\tilde{P}}{\eta \tilde{T}} = \frac{1}{r}$ is recovered in the limit $\eta, y \to 0$.

The dimensionless and characteristic macroscopic properties have the same meanings and origins as the corresponding LF properties. A pure fluid is completely characterized by its molecular parameters v_i, r_i, P_i^* or alternately, its corresponding macroscopic parameters $T_i^*, P_i^*, \rho_i^* \equiv (V_i^*)^{-1}$ (V^* intensive). Mixtures only require interaction parameters P_{ij}^* for each constituent pair in addition to its pure component parameters. Appendix A contains SPT chain equation of state parameters for pure fluids and binary mixtures.

2.3 Other Derived Thermodynamic Properties

The chemical potential (2.11) and the equation of state (2.14) can be used to derive other thermodynamic properties of the system to within functions of temperature.

2.3.1 Free Energy

The Gibbs free energy G is found by summing chemical potentials weighted by number fraction x_i:

$$\begin{aligned}\frac{G}{NkT} &= \sum_i x_i \beta \mu_i \\ &= \sum_i x_i \ln \rho_i - \frac{2r\eta}{\tilde{T}} \\ &+ r\left\{ \ln(1+y) + \left(\frac{1}{\sigma_{-3}}\right)\left[\begin{matrix} (6\sigma_{-1}\sigma_{-2} + \sigma_{-3})y \\ + \left(\frac{9}{2}\sigma_{-1}^3 + 3\sigma_{-1}\sigma_{-2}\right)y^2 + 3\sigma_{-1}^3 y^3 \end{matrix} \right] \right\}\end{aligned} \tag{2.18}$$

Fixing η and y through the equation of state, equation of state and taking $(\partial G/\partial N_i)_{T,P,N_{j\neq i}}$ on (2.18) recovers (2.11). Substituting the equation of state (2.14) into (2.18) gives an equivalent pressure explicit free energy:

$$\frac{G}{NkT} = \sum_i x_i \ln \rho_i + r\left[\frac{\tilde{P}}{\eta\tilde{T}} + \ln(1+y) + \frac{1}{\sigma_{-3}}\left(3\sigma_{-1}\sigma_{-2}y + \frac{3}{2}\sigma_{-1}^3 y^2\right) - \frac{1}{r} - \frac{\eta}{\tilde{T}}\right] \tag{2.19}$$

The Helmholtz free energy A can be found by subtracting $\frac{P}{\rho kT} = \frac{r\tilde{P}}{\eta\tilde{T}}$ from (2.19).

$$\frac{A}{NkT} = \sum_i x_i \ln \rho_i + r\left[\ln(1+y) + \frac{1}{\sigma_{-3}}\left(3\sigma_{-1}\sigma_{-2}y + \frac{3}{2}\sigma_{-1}^3 y^2\right) - \frac{1}{r} - \frac{\eta}{\tilde{T}}\right] \tag{2.20}$$

Applying the thermodynamic relation $P = -\left(\frac{\partial A}{\partial V}\right)_T$ to (2.20) recovers the EOS (2.14).

2.3.2 Enthalpy, Configurational Energy, and Configurational Entropy

To avoid doubly counting pairs, the configurational energy of the system is half the sum of the average energies of interaction of each chain:

$$\frac{U}{NkT} = \frac{1}{2}\sum_i x_i \beta \langle \psi_i \rangle = -\beta \eta r v^* \sum_i \sum_j \phi_i \phi_j P_{ij}^* = -\frac{r\eta}{\tilde{T}} \tag{2.21}$$

Neglecting thermal contributions to the internal energy, the enthalpy H of the system to within a function of temperature is given as:

$$\begin{aligned} \frac{H}{NkT} &= \frac{U}{NkT} + \frac{P}{\rho kT} = r\left[\frac{\tilde{P}}{\eta \tilde{T}} - \frac{r\eta}{\tilde{T}}\right] \\ &= r\left[\frac{(1+y)(\sigma_{-3} + 3\sigma_{-1}\sigma_{-2}y + 3\sigma_{-1}^3 y^2)}{\sigma_{-3}} - \left(1 - \frac{1}{r}\right) - \frac{2\eta}{\tilde{T}}\right] \end{aligned} \tag{2.22}$$

In this mean-field SPT model, the configurational entropy is decoupled from the configurational energy. The two are linked through their separate contributions to thermodynamic properties. The configurational entropy S may be calculated by subtracting the Helmholtz free energy (2.20) (which deliberately neglects the purely thermal energetic contribution) from the configurational energy (2.21).

$$\begin{aligned} \frac{S}{Nk} &= \frac{U}{NkT} - \frac{A}{NkT} \\ &= -\sum_i x_i \ln \rho_i - r\left[\ln(1+y) + \frac{1}{\sigma_{-3}}\left(3\sigma_{-1}\sigma_{-2}y + \frac{3}{2}\sigma_{-1}^3 y^2\right) - \frac{1}{r}\right] \end{aligned} \tag{2.23}$$

Equation (2.23) depends only on composition and density. Contributions from configurational energy and temperature are only implicit via the equation of state.

2.3.3 Second Order Properties

Several second order properties may be derived from equations presented thus far. The isothermal compressibility is given by:

$$\kappa = \frac{1}{\rho}\left(\frac{\partial \rho}{\partial P}\right)_{T,N} = \left(P^* \tilde{T} \begin{Bmatrix} y(1+y)\left[1 + 6\frac{\sigma_{-1}\sigma_{-2}}{\sigma_{-3}} y + 9\frac{\sigma_{-1}^3}{\sigma_{-3}} y^2\right] \\ -\left(1 - \frac{1}{r}\right)\eta - \frac{2\eta^2}{\tilde{T}} \end{Bmatrix} \right)^{-1} \tag{2.24}$$

and the thermal expansion coefficient by:

$$\alpha = -\frac{1}{\rho}\left(\frac{\partial \rho}{\partial T}\right)_{P,N} = \frac{\left[\frac{\tilde{P}}{\tilde{T}} + \frac{\eta^2}{\tilde{T}}\right]}{T \begin{Bmatrix} y(1+y)\left[1 + 6\frac{\sigma_{-1}\sigma_{-2}}{\sigma_{-3}} y + 9\frac{\sigma_{-1}^3}{\sigma_{-3}} y^2\right] \\ -\left(1 - \frac{1}{r}\right)\eta - \frac{2\eta^2}{\tilde{T}} \end{Bmatrix}} \tag{2.25}$$

The thermal pressure coefficient is easily calculated from (2.24) and (2.25).

$$\gamma_v = \left(\frac{\partial P}{\partial T}\right)_{V,N} = \frac{\alpha}{\kappa} = \frac{P^*}{\mathrm{T}^*}\left[\frac{\tilde{P}}{\tilde{T}} + \frac{\eta^2}{\tilde{T}}\right] \tag{2.26}$$

Since energies are only known to within a function of temperature, absolute heat capacities cannot be calculated. The difference in intensive heat capacities on a per chain basis is given by:

$$C_p - C_v = \frac{T\alpha\gamma_v}{\rho} = \frac{\frac{kr}{\eta}\left[\frac{\tilde{P}}{\tilde{T}} + \frac{\eta^2}{\tilde{T}}\right]^2}{\begin{Bmatrix} y(1+y)\left[1 + 6\frac{\sigma_{-1}\sigma_{-2}}{\sigma_{-3}} y + 9\frac{\sigma_{-1}^3}{\sigma_{-3}} y^2\right] \\ -\left(1 - \frac{1}{r}\right)\eta - \frac{2\eta^2}{\tilde{T}} \end{Bmatrix}} \tag{2.27}$$

Equation (2.27) shows that as the chain length increases, the heat capacity difference per chain increases. Dividing (2.27) by the number average molecular weight M_n gives the mass intensive heat capacity difference $\hat{C}_p - \hat{C}_V$. As with the LF model, for polymers, chain length is proportional to molecular weight. As $r \to \infty$, the heat capacity difference per chain also $\to \infty$, but the mass intensive $\hat{C}_p - \hat{C}_v$ remains finite.

2.3.4 Liquid/Vapor Critical Point

At a given composition, η is directly proportional to the number density ρ; therefore, the liquid/vapor critical conditions may be written as:

$$\left(\frac{\partial \tilde{P}}{\partial \eta}\right)_T = \left(\frac{\partial^2 \tilde{P}}{\partial \eta^2}\right)_T = 0 \tag{2.28}$$

For a pure fluid, equations (2.17) (2.27), and (2.28) establish a system of three equations to solve for dimensionless pressure $\tilde{P}_c$, temperature $\tilde{T}_c$, and occupied volume fraction η_c:

$$\tilde{P}_c = -\eta_c^2 + \eta_c \tilde{T}_c \left[\frac{1}{r} + 4y_c + 6y_c^2 + 3y_c^3\right] \tag{2.29}$$

$$\tilde{T}_c = \frac{(1-\eta_c)^2}{4 + 22y_c + 36y_c^2 + 18y_c^3} \tag{2.30}$$

$$30y_c^2 + 92y_c^3 + 99y_c^4 + 36y_c^5 = \frac{1}{r} \tag{2.31}$$

For convenience, the critical compressibility factor Z_c may be rewritten as:

$$Z_c = r\frac{\tilde{P}_c}{\eta \tilde{T}_c} = r\left[\frac{1}{3r} + \frac{19}{3}y_c^3 + 12y_c^4 + 6y_c^5\right] \tag{2.32}$$

The critical properties η_c, and $\tilde{T}_c$ as a function of r are shown in Figure 2.1.

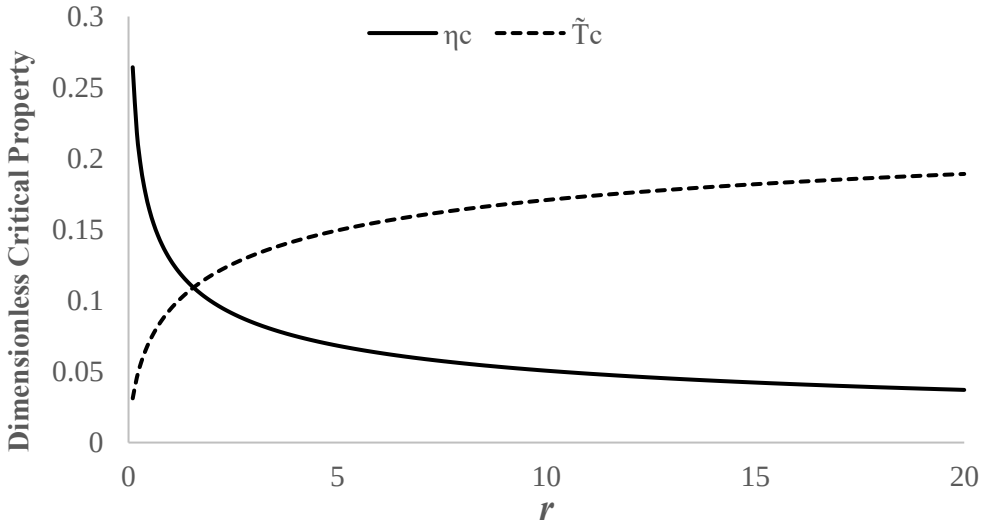

Figure 2.1: η_c and $\tilde{T}_c$ as a function of r for short chain length ($r \leq 20$)

For the limiting cases of $r = 1$, and $r \to \infty$, equation (2.31) may be solved analytically. $\eta_c, \tilde{T}_c, \tilde{P}_c,$ and Z_c for these cases are given in Table 2.1. The result of a density and pressure of zero and $Z_c = 1/3$ for $r \to \infty$ are identical to those of the LF model for an infinitely long chain[17]. 1/3 is the lowest value of $Z_c$the model predicts; however, $Z_c < 0.3$ for most small molecule liquids. As with the LF model, the SPT chain model is inadequate at critical PVT evaluation.

	$r = 1$	$r \to \infty$
η_c	$\frac{\sqrt{73} - 7}{12} = 0.1287$	0
$\tilde{T}_c$	$\frac{11{,}534\sqrt{73} - 98{,}898}{6{,}912} = 0.09383$	1/4
$\tilde{P}_c$	$\frac{8{,}762 - 1{,}022\sqrt{73}}{6{,}912} = 0.004344$	0
Z_c	$\frac{1{,}975 + 157\sqrt{73}}{9{,}216} = 0.3599$	1/3

Table 2.1: Dimensionless critical properties in the single sphere ($r = 1$) and infinite chain ($r \to \infty$) limits

2.3.5 Phase Stability in Binary Mixtures and the Spinodal

A homogeneous binary mixture is stable or metastable with respect to concentration fluctuations if the second concentration derivative of the Gibbs free energy is positive, or equivalently if

$$\frac{\partial \mu_i}{\partial x_i}\Big)_{T,P} > 0 \tag{2.33}$$

for both species 1 and 2 in the binary mixture. Applying relationships described in reference [33] to the SPT chain model, gives the stability condition as:

$$\begin{aligned} & v^*\left(\frac{1}{r_1 v_1^* \phi_1}+\frac{1}{r_2 v_2^* \phi_2}\right)-2\eta\beta v^* \Delta P_{12}^* - \frac{\kappa\beta v^* P_\phi^2}{\eta} \\ & +\frac{1}{\sigma_{-3}}\left(\frac{1}{\sigma_1}-\frac{1}{\sigma_2}\right)^2\left[6y\left(\frac{1}{\sigma_1}+\frac{1}{\sigma_2}\right)+9y^2\sigma_{-1}\right] \end{aligned} \quad > \quad 0 \tag{2.34}$$

in which

$$\Delta P_{12}^* \equiv P_1^* + P_2^* - 2P_{12}^* \tag{2.35}$$

and $P_\phi = \partial P/\partial \phi\ )_{T,v}$ is the isothermal, isochoric pressure coefficient and is given by:

$$P_\phi = kT\left\{\begin{array}{l} -2\eta^2\beta[\phi_1 P_1^* + (\phi_2-\phi_1)P_{12}^* - \phi_2 P_2^*] \\ +\eta\left(\dfrac{1}{r_1 v_1^*}-\dfrac{1}{r_2 v_2^*}\right)+(y-\eta)\left(\dfrac{1}{v_1^*}-\dfrac{1}{v_2^*}\right) \\ +\dfrac{6}{\pi}\left(\dfrac{1}{\sigma_1}-\dfrac{1}{\sigma_2}\right)\left[3y^2\sigma_{-2}+3y^2\sigma_{-1}\left(\dfrac{1}{\sigma_1}+\dfrac{1}{\sigma_2}\right)+9y^3\sigma_{-1}^2\right] \end{array}\right\} \tag{2.36}$$

If the indices 1 & 2 are interchanged in (2.36), P_ϕ only changes sign, and the left side of inequality (2.34) is unaffected. All other quantities in (2.34) have been defined earlier in the chapter.

In inequality (2.34),

$$v^*\left(\frac{1}{r_1 v_1^* \phi_1}+\frac{1}{r_2 v_2^* \phi_2}\right)$$

is a favorable (supports homogeneous phase stability) combinatorial entropy contribution. $-2\eta\beta v^* \Delta P_{12}^*$ is an energetic contribution. It is generally negative (unfavorable), but in some cases, may be positive (favorable) if $\Delta P_{12}^* < 0$. $-\kappa\beta v^* P_\phi^2 \kappa P_\phi^2/\eta$ is an unfavorable entropic contribution from equation of state effects (non-zero compressibility), and

$$\frac{1}{\sigma_{-3}}\left(\frac{1}{\sigma_1}-\frac{1}{\sigma_2}\right)^2\left[6y\left(\frac{1}{\sigma_1}+\frac{1}{\sigma_2}\right)+9y^2\sigma_{-1}\right]$$

is a favorable entropic term arising from the net reduction in excluded volume for a HS pair upon mixing spheres of different sizes.

If inequality (2.34) is not met, the homogenous binary phase is unstable and the mixture will separate into two fluid phases. Setting the inequality equal to zero defines the spinodal, the boundary between phase stability (or metastability) and instability.

2.3.6 Pressure Explicit Chemical Potential (binary mixtures)

Often in binary phase equilibrium calculations, an alternate yet equivalent pressure explicit form of the chemical potential (2.11) is more convenient. Multiplying both sides of the equation of state (2.14) by $\sigma_{-3}\sigma_1^3 = v_1^*/v^*$ and rearranging yields:

$$\frac{P v_1^*}{\eta k T}-\sigma_1^3(1+y)[\sigma_{-3}+3\sigma_{-1}\sigma_{-2}y+3\sigma_{-1}^3 y^2]+\left(1-\frac{1}{r}\right)\frac{v_1^*}{v^*}+v_1\eta\beta P^*=0 \quad (2.37)$$

Since (2.37) equals zero, it can be added to (2.11) without changing its value. This addition yields (neglecting the temperature independent $-\ln r_i v_i$)

$$\begin{aligned}\beta\mu_1 = \ln\phi_1 + \left(1 - \frac{r_1 v_1^*}{r_2 v_2^*}\right)\phi_2 + r_1\eta\chi_1\phi_2^2 + \ln\eta - 1 \\ + r_1\left[\begin{aligned}&\ln(1+y) + (3\sigma_{-1}\sigma_1 + 3\sigma_{-2}\sigma_1^2 - 3\sigma_{-1}\sigma_{-2}\sigma_1^3)y \\ &+ \left(\frac{9}{2}\sigma_{-1}^2\sigma_1^2 - 3\sigma_{-1}^3\sigma_1^3\right)y^2 + \frac{\tilde{P}_1}{\eta\tilde{T}_1} - \frac{\eta}{\tilde{T}_1}\end{aligned}\right]\end{aligned} \tag{2.38}$$

$\tilde{P}_1 \equiv P/P_1^*; \tilde{T}_1 \equiv T/T_1^*$. χ_1 is given by:

$$\chi_1 = \beta v_1^* \Delta P_{12}^* \tag{2.39}$$

The following identity was used in deriving (2.38):

$$-\frac{r_1}{r}\sigma_{-3}\sigma_1^3 = -1 + \left(1 - \frac{r_1 v_1^*}{r_2 v_2^*}\right)\phi_2 \tag{2.40}$$

The pressure explicit chemical potential for species 2 can be found by interchanging the subscripts 1 and 2.

Equation (2.19) is recovered when the $-\ln r_i v_i^*$ is restored, and $\sum_i x_i\beta\mu_i$ is applied to this pressure explicit form of the chemical potential. Equation (2.38) is particularly useful when the change in μ_1 on mixing is required to satisfy the functional form suggested by classical theory:

$$\beta(\mu_1 - \mu_1^0) = \ln\phi_1 + \left(1 - \frac{r_1 v_1^*}{r_2 v_2^*}\right)\phi_2 + \phi_2^2\chi \tag{2.41}$$

where μ_1^0 is the pure component chemical potential. In this way (2.41) can be used to define an effective χ,

$$\chi_{eff} = r_1\eta\chi_1 + \frac{1}{\phi_2}\left\{\ln\left(\frac{\eta}{\eta_1^0}\right) + r_1\left[\begin{array}{l}\ln\left(\frac{1+y}{1+y_1^0}\right) - 3y_1^0 - 3(y_1^0)^2 \\ +(3\sigma_{-1}\sigma_1 + 3\sigma_{-2}\sigma_1^2 - 3\sigma_{-1}\sigma_{-2}\sigma_1^3)y \\ +\left(\frac{9}{2}\sigma_{-1}^2\sigma_1^2 - 3\sigma_{-1}^3\sigma_1^3\right)y^2 \\ \quad +\frac{\tilde{P}_1}{\tilde{T}_1}\left(\frac{1}{\eta} - \frac{1}{\eta^0}\right) - \frac{(\eta - \eta_1^0)}{\tilde{T}_1}\end{array}\right]\right\} \quad (2.42)$$

in which η_1^0 and y_1^0 denote η and y of pure component 1 at the specified temperature and pressure. The analogous expression for the LF model is[19]:

$$\chi_{eff} = r_1\tilde{\rho}\chi_1 + \frac{1}{\phi_2^2}\left\{\ln\left(\frac{\tilde{\rho}}{\tilde{\rho}_1^0}\right) + r_1\left[\begin{array}{l}\frac{(1-\tilde{\rho})}{\tilde{\rho}}\ln(1-\tilde{\rho}) \\ -\frac{(1-\tilde{\rho}_1^0)}{\tilde{\rho}_1^0}\ln(1-\tilde{\rho}_1^0) \\ +\frac{\tilde{P}_1}{\tilde{T}_1}\left(\frac{1}{\tilde{\rho}} - \frac{1}{\tilde{\rho}_1^0}\right) - \frac{(\tilde{\rho} - \tilde{\rho}_1^0)}{\tilde{T}_1}\end{array}\right]\right\} \quad (2.43)$$

in which $\tilde{\rho}$ is a reduced density analogous to η and all other LF variables and parameters have the same interpretations as those for the SPT model.

Experimentally, for a solvent(1)/polymer(2) solution, χ_{eff} may increase or decrease as polymer composition increases[34]. Both the SPT and LF models predict an increase in reduced density with increasing polymer composition. For the LF model, all composition dependent terms within the square brackets of (2.43) decrease with increasing polymer composition (ϕ_2) and (2.43) almost universally predicts a decrease in χ_{eff} with increasing ϕ_2. In contrast, many of the terms in the square brackets of (2.42) increase as η increases, and the SPT χ_{eff} may either increase or decrease with ϕ_2.

2.4 CHAPTER SUMMARY

Using Scaled Particle Theory (SPT) in a mean-field configurational energy approximation, an easily implemented, off-lattice, thermodynamically consistent model of fluid mixtures is developed. Chemical potentials are derived from the random insertion of a HS chain into a HS fluid and invoking random mixing to calculate energetics. Like the Lattice Fluid (LF) model, the SPT model completely characterizes pure fluids with three parameters that can be calculated from pure component properties. Binary mixtures require only one additional interaction parameter. Several thermodynamic properties, including binary phase stability criteria are derived. This model was shown to calculate properties of small, rigid, nearly spherical molecules in Chapter 1 when chain length was set as $(r = 1)$. In Chapter 3 this model is compared with LF model for calculating properties of fluid systems.

Chapter 3: SPT Model Comparisons with Experiment*

3.1 INTRODUCTION

The SPT chain model is a simple, off-lattice thermodynamic model that approximates molecules with a well-defined size and shape. Despite its apparent theoretical advantages, the model's success should be determined by its ability to predict thermodynamic properties against other theoretical models. In Chapter 3 the SPT chain model is compared against experimental data and the Lattice Fluid model[17–19]. Both models are entirely theoretical in origin, require the same number of parameters, and are analytically simple. Most of the systems selected in this chapter had been successfully described by the LF model[17,18,35].

When considering binary mixtures in this chapter for both models, the interaction parameter P_{12}^* will be reported through a parameter ζ_{12} which scales P_{12}^* relative to the geometric mean of the pure species characteristic pressures.

$$\zeta_{12} = P_{12}^*/\sqrt{P_1^* P_2^*} \tag{3.1}$$

In the original formulation of the LF model[18], the characteristic energy $\varepsilon^* = kT^*$ was given by a quadratic mixing rule weighted by ϕ instead of the characteristic pressure P^* as in equation (2.14). The geometric mean scaling was also done on a characteristic interaction energy $\varepsilon_{12}^* = \zeta_{12}\sqrt{\varepsilon_1^* \varepsilon_2^*}$ instead of by (3.1). All LF predictions in this chapter were recalculated using the characteristic pressure weighted mixing rule. Pure component SPT parameters and ζ_{12} fit for certain mixtures for both models can be found in

* As with Chapter 2, this material was partly published as: Sean P. O'Keefe, and Isaac C. Sanchez, "Scaled Particle Theory of solutions: Comparison with Lattice Fluid model" *Fluid Phase Equilibria* 433, 67 (2017)[16]. Sean Patrick O'Keefe is the primary author.

Appendix A. Other LF parameters are either those reported in [17] and [19] or given as used in this chapter.

3.2 One Component Liquid/Vapor Equilibrium

For a pure liquid (liq) in equilibrium with its vapor (vap), chemical potential s of each phase at the given temperature and pressure must be equal:

$$\mu_{liq}(T,P) = \mu_{vap}(T,P) \tag{3.2}$$

At a fixed temperature, (2.17) for each phase and (3.2) establish a system of three equations to solve for the unknowns $P, \eta_{liq}, \eta_{vap}$. As described in Chapter 1, setting $Z = r\tilde{P}/\eta\tilde{T} \simeq 0$ excellently approximates η_{liq} at NLR temperatures, but in order to obtain saturated pressures and η_{vap}, the two equations of state and chemical potential equality must be solved without approximation. Model predictions of the temperature dependence of saturated pressures for nitrogen and the more flexible n-decane are shown in Figures 3.1 and 3.2 respectively. Saturated density predictions are shown in Figures 3.3 and 3.4. Experimental data used for Figures 3.1–3.4 were obtained from the NIST webbook of thermophysical properties of fluid systems http://webbook.nist.gov/chemistry/fluid/[3]. The two models are comparable at predicting both saturated pressures and densities.

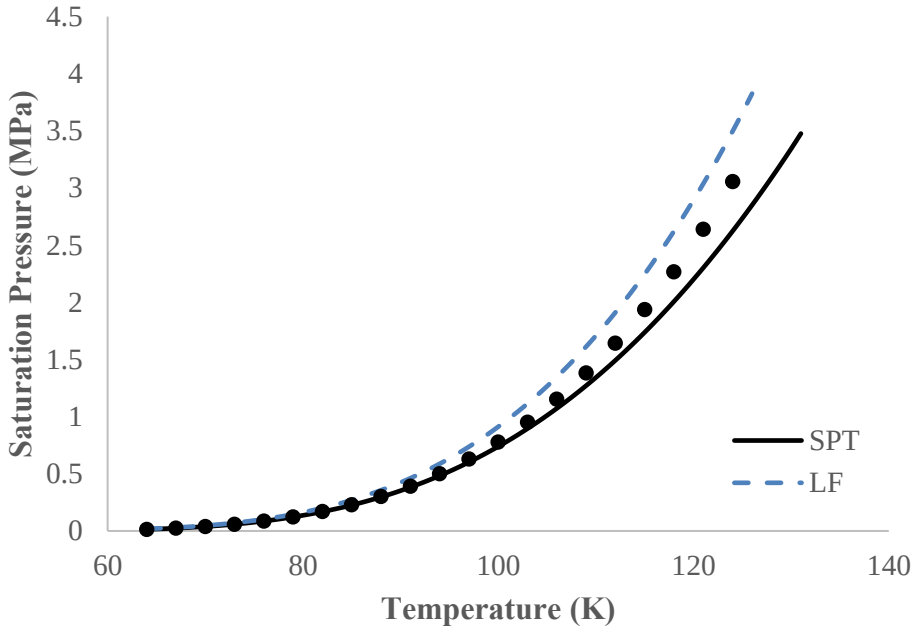

Figure 3.1: Model comparison for calculating vapor pressure of nitrogen

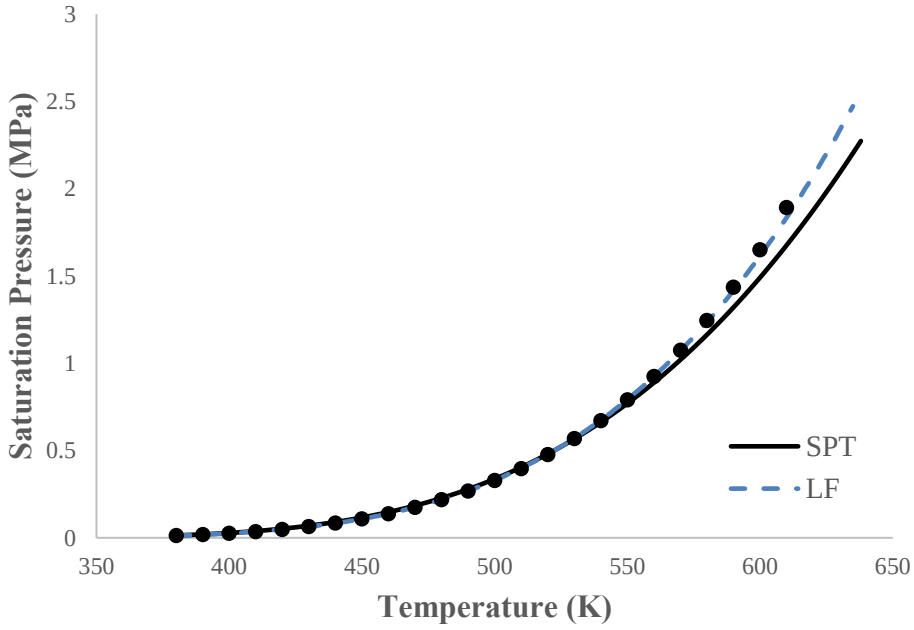

Figure 3.2: Model comparison for calculating vapor pressure of n-decane

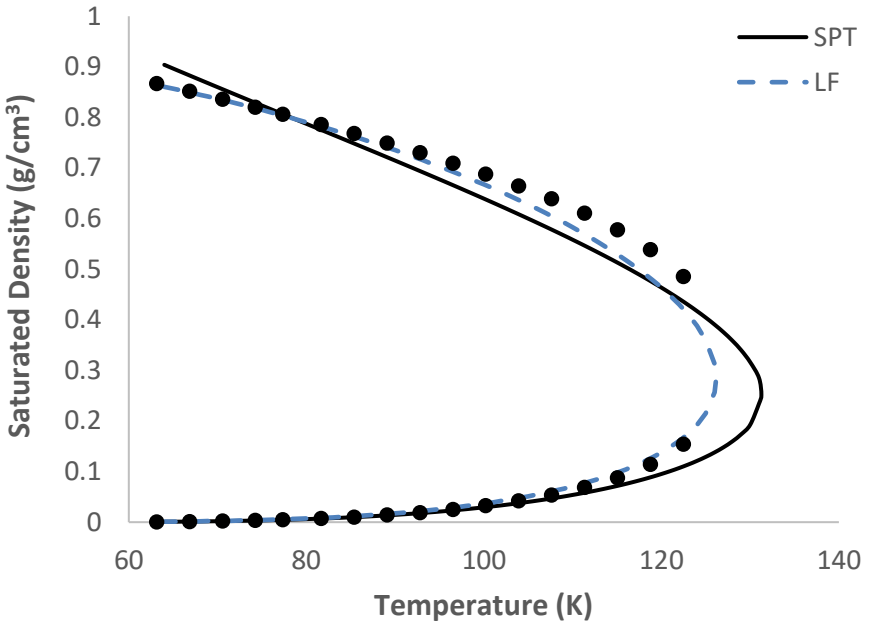

Figure 3.3: Saturated liquid and vapor density calculations for nitrogen

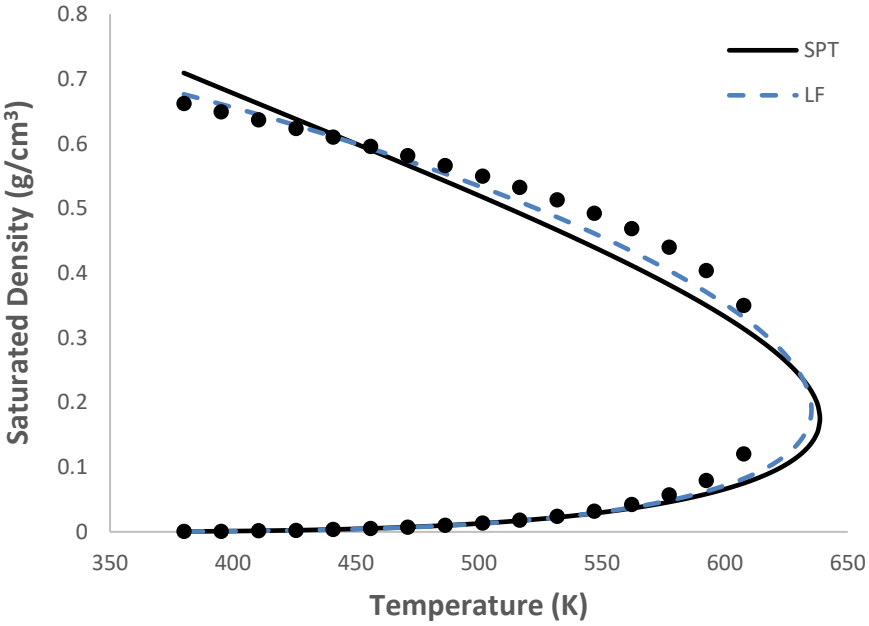

Figure 3.4: Saturated liquid and vapor density calculations for n-decane

3.3 GAS SOLUBILITY IN MOLTEN POLYMERS

By equating the chemical potential of a pure gas (μ_1^0) to that of the same gas dissolved in a polymer (μ_1), a Henry's law constant (k_H) for that gas(1)/polymer(2) system is obtained. For the pure gas equation (2.38) is written as:

$$\beta\mu_1^0 = \ln\eta_1^0 - 1 + \frac{r_1\tilde{P}_1}{\eta_1^0\tilde{T}_1} + r_1\left[\ln(1+y_1^0) + 3y_1^0 + \frac{3}{2}(y_1^0)^2 - \frac{\eta_1^0}{\tilde{T}_1}\right] \tag{3.3}$$

In the dilute limit both $\eta, y \to 0$ and the ideal gas law is valid such that $r_1\tilde{P}_1/\eta_1\tilde{T}_1 = 1$ and (3.3) simplifies to:

$$\beta\mu_1^0 = \ln\eta_1^0 \tag{3.4}$$

η_i^0, and y_i^0 denote η and y of the pure species i. Dilute gases are sparingly soluble in polymers[35]. The limit $\phi_1 \to 0$, may be applied to the composition of dissolved gas in the polymer. In this limit, $\phi_2 \to 1,\ \eta \to \eta_2^0, y \to y_2^0$, and $\sigma_{-k} \to \sigma_2^{-k}$. The SPT chemical potential for the gas in this limit is given by:

$$\beta\mu_1 = \ln\phi_1 + \ln\eta_2^0 + r_1\begin{bmatrix}\ln(1+y_2^0) + \left(3\frac{\sigma_1}{\sigma_2} + 3\frac{\sigma_1^2}{\sigma_2^2} - 3\frac{\sigma_1^3}{\sigma_2^3}\right)y_2^0 \\ + \left(\frac{9}{2}\frac{\sigma_1^2}{\sigma_2^2} - 3\frac{\sigma_1^3}{\sigma_2^3}\right)(y_2^0)^2 + \frac{\tilde{P}_1}{\eta_2^0\tilde{T}_1} - \frac{\eta_2^0}{\tilde{T}_1} + \eta_2^0\chi_1\end{bmatrix} \tag{3.5}$$

Denoting the concentration of gas in the polymer c_1^{liq}, and the partial pressure of gas in equilibrium with the liquid P_1, Henry's Law is written as:

$$P_1 = k_h c_1^{liq} \tag{3.6}$$

The SPT model definitions give c_1^{liq} in units of mass per unit volume as:

$$c_1^{liq} = \frac{\eta_2^0 M_1}{r_1 v_1}\phi_1 \tag{3.7}$$

in which M_1 is the molar mass of the gas. Equating chemical potentials (3.4) and (3.5) and rearranging terms gives the reciprocal of the Henry's law constant k_H^{-1} as:

$$k_H^{-1} = \frac{M_1}{RT}(1-\eta_2^0)^{r_1}\exp\left\{r_1\begin{bmatrix}-\left(3\frac{\sigma_1}{\sigma_2}+3\frac{\sigma_1^2}{\sigma_2^2}-3\frac{\sigma_1^3}{\sigma_2^3}\right)y_2^0 \\ -\left(\frac{9}{2}\frac{\sigma_1^2}{\sigma_2^2}-3\frac{\sigma_1^3}{\sigma_2^3}\right)(y_2^0)^2-\frac{\tilde{P}_1}{\eta_2^0\tilde{T}_1}+\frac{\eta_2^0}{\tilde{T}_1}-\eta_2^0\chi_1\end{bmatrix}\right\} \tag{3.8}$$

Solubility of gases in polymers is frequently measured through inverse gas chromatography (IGC) experiments. In these experiments the net retention volume V_N is measured as the difference in volume of gas needed to elute a probe gas and volume of gas needed to elute a non-interacting marker gas. V_N is thus the total volume of gas absorbed by the polymer. Dividing V_N by the mass of the polymer gives the specific retention volume V_g which is related to (k_H^{-1}) through[36]:

$$V_g = k_H^{-1}\left(\frac{RT}{M_1\rho_2}\right) \tag{3.9}$$

in which ρ_2 is the mass density of the polymer. Often V_g is corrected to a standard temperature $T_0 = 273.15$ K in which case, the corrected specific retention volume V_g^0 is given by[37]:

$$V_g^0 = k_H^{-1}\left(\frac{RT_0}{M_1\rho_2^0}\right) \tag{3.10}$$

The LF equation for k_H analogous to equation (3.8) is given as[35]:

$$k_H^{-1} = \frac{M_1}{RT}(1-\tilde{\rho}_2)^{r_1}\exp\left\{r_1\left[-1-\frac{\ln(1-\tilde{\rho}_2)}{\tilde{\rho}_2}-\frac{\tilde{P}_1}{\tilde{\rho}_2\tilde{T}_1}+\frac{\tilde{\rho}_2}{\tilde{T}_1}-\tilde{\rho}_2\chi_1\right]\right\} \tag{3.11}$$

From a functional viewpoint, the primary difference in equations (3.8) and (3.11) is that the SPT model prediction explicitly depends on the segment diameter ratio σ_1/σ_2 whereas the LF model does not.

Specific retention volumes were calculated with both the LF and SPT models for gases at atmospheric pressure dissolved in three polymeric liquids. A geometric mean approximation was invoked for the cross term $P_{12}^* = \sqrt{P_1^* P_2^*}$ $(\zeta_{12} = 1)$; therefore, the mixture properties are completely determined by pure component equation of state parameters. Figures 3.5–3.7 compare the predicted specific retention volumes that scale gas solubility. Experimental solubility data was taken from references [38] and [39].

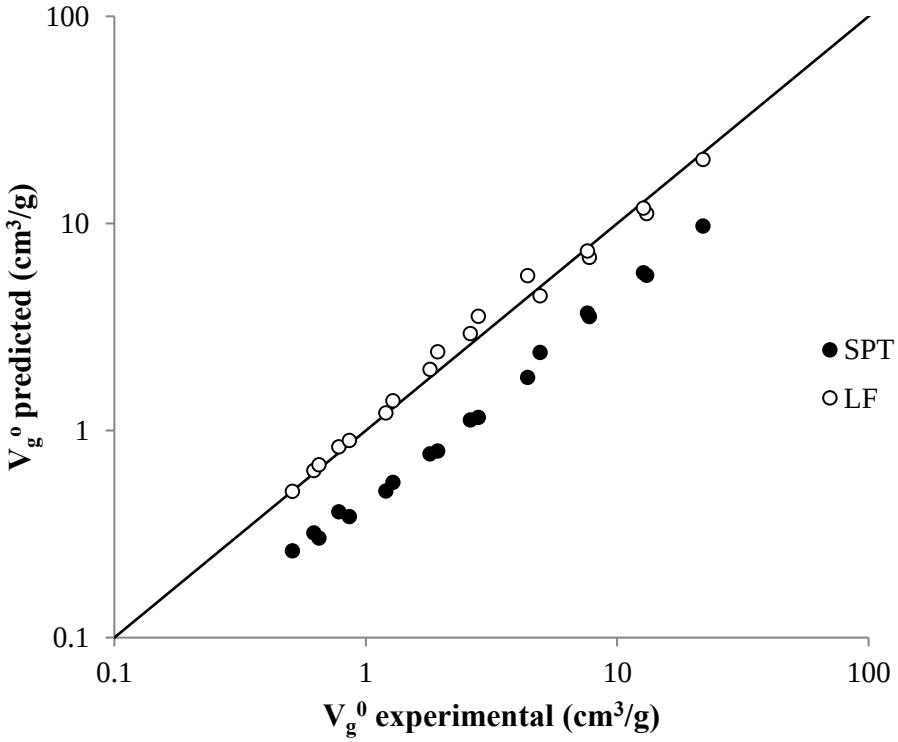

Figure: 3.5 Comparison of calculated and experimental specific retention volumes for short alkanes and aromatic hydrocarbons at 423, 448, and 473 K in polystyrene.

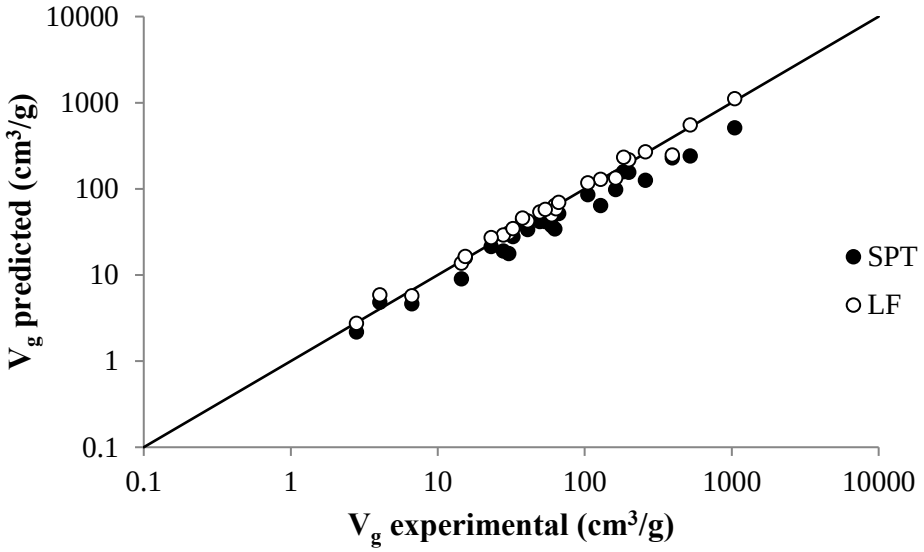

Figure 3.6: Comparison of experimental and calculated specific retention volumes of alkanes, cyclic hydrocarbons, aromatic hydrocarbons, and chlorinated hydrocarbons in poly(1-butene) at 373 K.

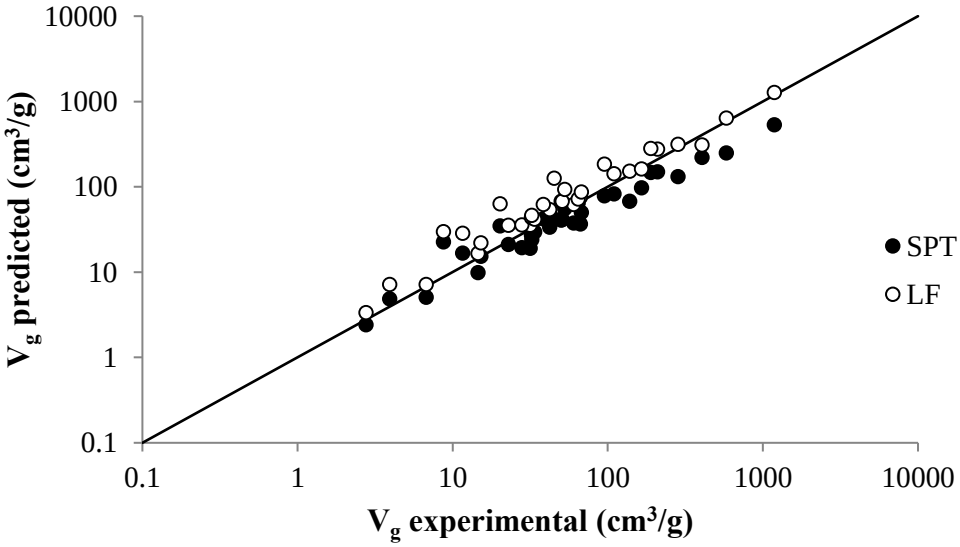

Figure 3.7: Comparison of calculated and experimental specific retention volumes in atactic-polypropylene at 373 K for 26 hydrocarbons and 8 oxygen containing organics. LF parameters for a-PP were fit as $T^* = 619$ K, $P^* = 340$ MPa, $\rho^* = 0.917$ g/cm^3

Predicted SPT solubilities were generally lower than corresponding LF predictions. With the exception of undecane, the absolute percent error in the predictions of alkane solubility increased with increasing chain length for SPT, while the percent error for the LF model remained roughly constant. LF was superior in predicting solubilities of larger, more chainlike molecules such as alkanes and aromatic hydrocarbons. SPT was somewhat better at predicting solubilities of very small chlorine containing molecules and most of the oxygen containing organics.

3.4 ISOTHERMAL METHANE/BUTANE LIQUID/VAPOR EQUILIBRIUM

As with the pure species liquid/vapor equilibrium discussed in Section 3.2, phase equilibrium conditions for binary mixtures are determined through equating chemical potentials

$$\begin{aligned} \mu_1'(T,P,\phi_1') &= \mu_1''(T,P,\phi_1'') \\ \mu_2'(T,P,\phi_2') &= \mu_2''(T,P,\phi_2'') \end{aligned} \tag{3.12}$$

in which the primes denote separate phases. At equilibrium, each phase must satisfy the equation of state (2.14). The relationship:

$$\begin{aligned} \phi_1' + \phi_2' &= 1 \\ \phi_1'' + \phi_2'' &= 1 \end{aligned} \tag{3.13}$$

must also hold. At fixed temperature and pressure, equations (3.12), (3.13), (2.11), and (2.14) completely describe the binary two phase system in equilibrium and determine the compositions of each phase.

Figure 3.8 shows a liquid/vapor diagram in the pressure-composition plane for a methane/n-butane mixture at 104.4°C. The values of ζ_{12} for both the SPT and LF models were determined by a single point fit matching the experimental boiling point at a

composition 10.1 mol% methane at 54.4°C, 50 °C below the temperature of Figure 3.8. Experimental data for the phase diagram calculation were obtained from reference [40].

Both the LF and SPT model predict the retrograde condensation phenomenon, in which a liquid can be produced by decreasing pressure. Reversing the example given in reference [18], at 104.4°C and a pressure of over 100 atm, a mixture of 54 mol% methane is a dense fluid. If the pressure is decreased to about 95.3 atm, the liquid/vapor coexistence curve is reached, and a liquid of a higher density appears. Liquid continues to appear with decreasing pressure until about 72 atm when liquid begins to disappear as pressure is decreased. At about 54.3 atm, the lower branch of the coexistence curve is reached, and the liquid disappears completely.

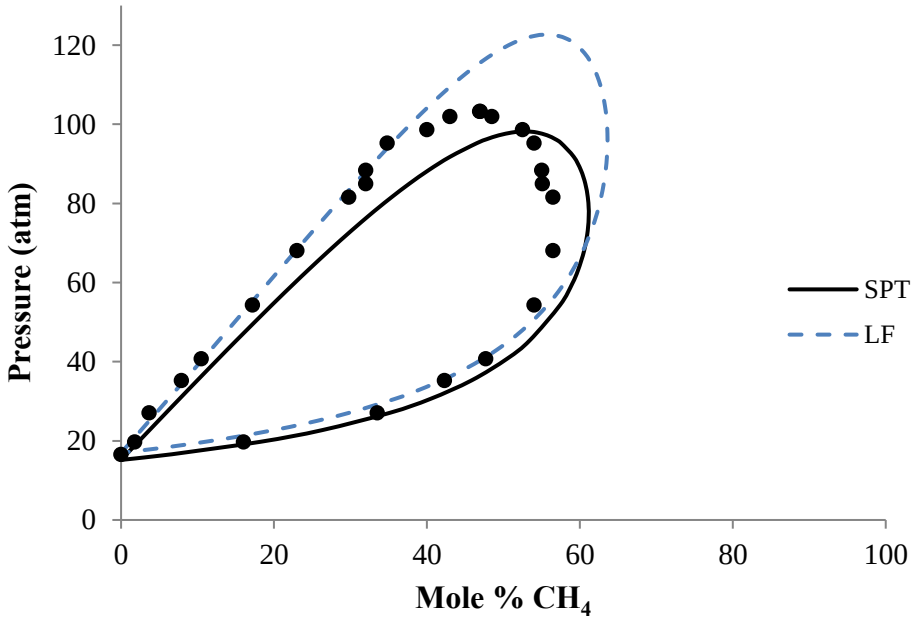

Figure 3.8: Liquid/Vapor phase diagram in the pressure composition plane for methane/n-butane at 104.4°C.

LF calculations are more accurate than SPT in the high butane composition limit. Though butane is a reasonably small molecule, it is larger and more flexible than methane. SPT becomes increasingly more accurate as the methane concentration increases. The experimental data suggests a mixture critical pressure of 102 atm at 104.4°C. LF predicts a critical pressure of 122.7 atm while SPT better predicts a critical pressure of 98.2 atm.

3.5 HEATS AND VOLUMES OF MIXING

Figure 3.9 compares experimental heats of mixing given in reference [41] with ΔH_m calculated using equation (2.22) and the analogous LF enthalpy equation for three binary hydrocarbon mixtures, benzene/cyclohexane, benzene/n-heptane, and cyclohexane/n-heptane at atmospheric pressure and 20°C. The values of ζ_{12} given in Table A3 were calculated by matching a single ΔH_m for each mixture at an intermediate composition to its experimental measurement. All other properties were then calculated with these ζ_{12}. Because $Z_{liq} \ll \left|U_{liq}/kT\right|$, the potential energy terms dominate ΔH_m calculations, and $\Delta H_m \simeq \Delta U_m$ for these liquids. Since both the LF and SPT models use the same mean-field approximation for potential energy, the calculations in Figure 3.9 agree to the extent that they appear to superpose.

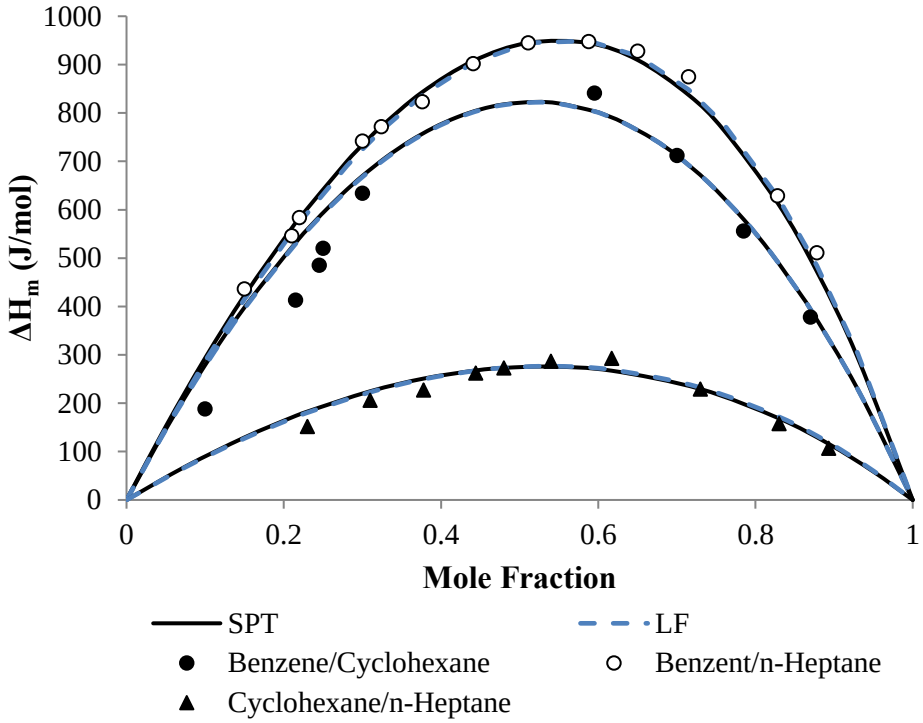

Figure 3.9: Heats of mixing for three hydrocarbon mixtures at atmospheric pressure and 20°C

Volume changes on mixing for these binary mixtures at 25°C and atmospheric pressure were also calculated using both models and compared with experimental data for these mixtures with the same values of ζ_{12} as those used to construct Figure 3.9. Figure 3.10 plots calculated volume changes on mixing against measured values taken from reference [42]. The SPT chain model is clearly inferior as the volume changes for the benzene/cyclohexane solution are overestimated by as much as 50%. The two models agree well for cyclohexane/n-heptane volumes changes of mixing. In Figure 3.10 V_0 is the ideal volume of the mixture assuming volume additivity. For both models the benzene/cyclohexane mixture had the greatest volume changes on mixing, and the cyclohexane/n-heptane mixture had the least volume change on mixing.

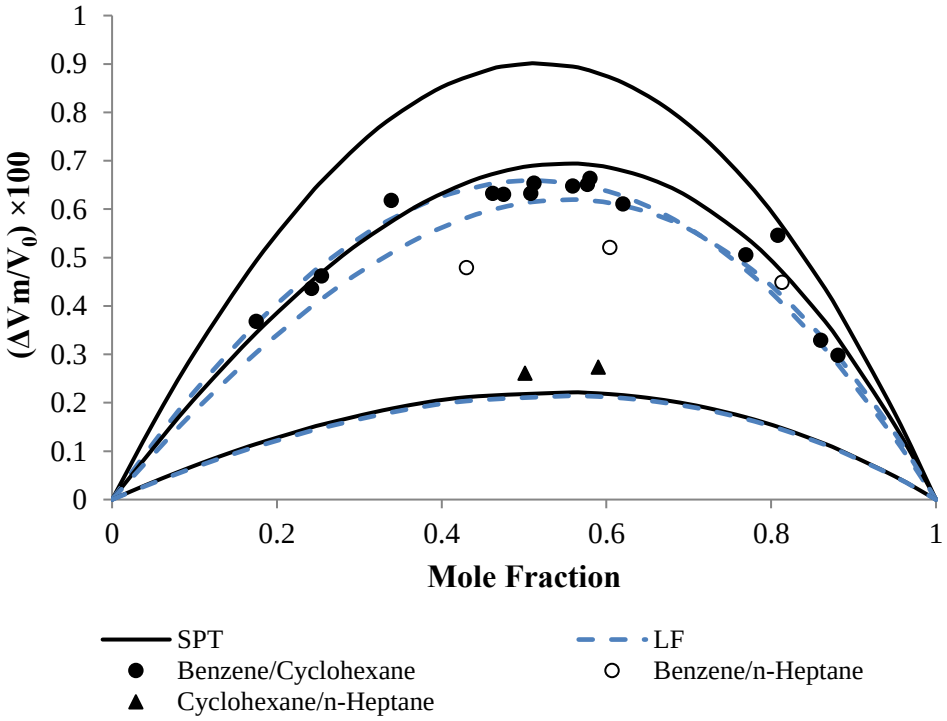

Figure 3.10: Volume change of mixing for three hydrocarbon mixtures at 25°C and atmospheric pressure

All thermodynamic properties of ternary and higher order systems for the LF and SPT models are completely determined by pure component and respective binary mixture parameters. Table 3.1 compares ΔH_m for benzene/cyclohexane/n-heptane ternary mixtures calculated with the two models and experimental results. The SPT model appears comparable to LF at calculating enthalpies of mixing of ternary mixtures.

Mole Fractions		ΔH_m (J/mol)		
Benzene	Cyclohexane	SPT	LF	Exptl. [43]
0.27	0.418	807	805	737
0.335	0.505	836	836	818
0.752	0.188	689	694	697
0.81	0.070	625	634	649
0.791	0.120	642	649	673
0.856	0.083	483	490	489
0.501	0.195	972	974	946
0.595	0.250	911	915	904
0.298	0.280	845	841	819
0.316	0.237	861	857	828
0.415	0.342	935	935	957
0.197	0.684	604	604	616
0.206	0.169	661	653	645

Table 3.1: SPT and LF heats of mixing for benzene/cyclohexane/n-heptane ternary mixtures

3.6 SYSTEMS WITH UPPER CRITICAL SOLUTION TEMPERATURES

At low temperatures, the ΔP_{12}^* term in inequality (2.34) becomes large in magnitude. If ΔP_{12}^* is positive, inequality (2.34) may not hold for a single, binary homogeneous phase at low temperatures, and the system will phase separate into two liquid phases. For a given temperature and pressure, composition of each phase is given by the conditions in Section 3.4. When plotted on the temperature-composition plane, liquid/liquid equilibria of this type reach a maximum Upper Critical Solution Temperature (UCST).

Binary mixtures of perfluoroalkanes and hydrocarbons often exhibit this liquid/liquid behavior at low temperatures. Figure 3.11 compares experimental solubility data from reference [25] with the coexistence curves calculated with the SPT and LF models for an n-perfluorooctane/n-octane mixture at atmospheric pressure. ζ_{12}were determined by requiring the octane rich phase at 350.52 K to have an n-perfluorooctane

mole fraction $x = 0.3013$. The SPT model is slightly closer to the experimental data than the LF model, but the models agree better with each other than either one does with the data. As with the ΔH_m calculations in Section 3.5, the UCST type of phase instability and equilibrium conditions strongly depend on the unfavorable changes in potential energy on mixing, and both models use a mean-field VDW type potential energy. Theoretical UCST type liquid/liquid coexistence curves are narrower than the experimental solubility measurements, consistent with the coexistence curves in [18].

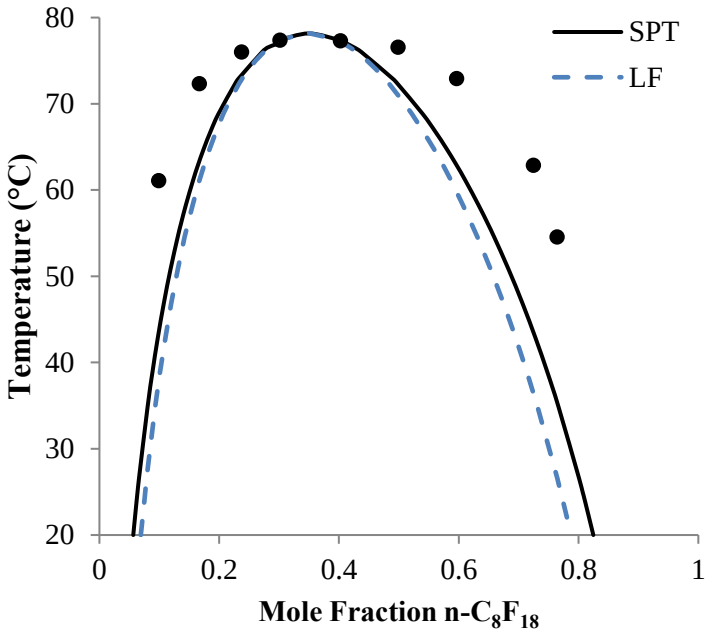

Figure 3.11: Liquid-liquid equilibrium for n-perfluorooctane/n-octane at atmospheric pressure. LF n-perfluorooctane parameters are $T^* = 430.9$ K, $P^* = 220.9$ MPa, $\rho^* = 2.250$ g/cm^3.

Setting inequality (2.34) to zero defines the spinodal. The spinodal is a condition applied to a single, homogeneous phase, and it is more easily solved than the system of equation s required for binary phase equilibrium calculations. By calculating the limit of

homogeneous phase instability, the spinodal provides the general nature of the phase diagram. Extrema in the spinodal occur at the same temperatures and compositions as critical solution temperatures in liquid/liquid coexistence curves. The UCST type of liquid/liquid phase stability strongly depends on ΔP_{12}^{*}. Changes in P_{12}^{*} or ζ_{12} of $\pm 0.1\%$ dramatically shift the calculated UCST. To illustrate the effect of ζ_{12} on the calculated UCTS, Table 3.2 shows UCSTs calculated for five aniline mixtures assuming $\zeta_{12} = 1$. Values of ζ_{12} that yield the correct UCSTs, shown in Table 3.2, are near unity, yet few of the UCSTs calculated with a geometric mean assumption is acceptable.

Aniline/	UCST (°C)			ζ_{12} required for correct UCST	
	Expt [44]	SPT	LF	SPT	LF
n-Butane	84.1	61.89	10.05	0.99396	0.98641
n-Pentane	71.7	30.42	35.22	0.98837	0.99147
n-Hexane	69.1	14.42	63.71	0.98498	0.99860
n-Heptane	70.1	1.06	52.79	0.98181	0.99574
Cyclohexane	29.5	-69.82	-110.75	0.97421	0.97013

Table 3.2: Effect of ζ_{12} on calculated UCSTs for aniline/hydrocarbon mixtures at atmospheric pressure

Because of this sensitivity, values of ζ_{12} for three binary polar/nonpolar acetone mixtures were fit by matching the calculated liquid/liquid UCSTs to those given in reference [44]. To demonstrate the self-consistency of the model, these same values of ζ_{12} fit at the UCST were used to calculate the liquid/vapor coexistence curves for each acetone mixture. These mixtures all experience minimum boiling azeotropes[45] at more than 80°C. above the respective UCST. Figure 3.12 shows the liquid/vapor phase diagram for the acetone/carbon disulfide mixture at atmospheric pressure. Methods of fitting ζ_{12} were identical for SPT and LF models. Experimental data for Figure 3.12 was taken from reference [40]. Table 3.3 summarizes predicted azeotrope temperatures and

compositions and compares them to experimental data. For these systems SPT and LF models agree well with each other and measured quantities.

acetone/	UCST (°C)[44]	Azeotrope Temperature (°C)			Azeotrope composition wt% acetone		
		SPT	LF	Expt [45]	SPT	LF	Expt[45]
carbon disulfide	−42	41.1	40.6	39.25	31.8	31.7	33
n-Hexane	−39	52.5	51.9	49.8	65.8	62.6	59
Cyclohexane	−29	54.2	54.4	53.0	75.6	75.3	67

Table 3.3: Comparison of experimental and theoretical azeotropes of binary acetone mixtures

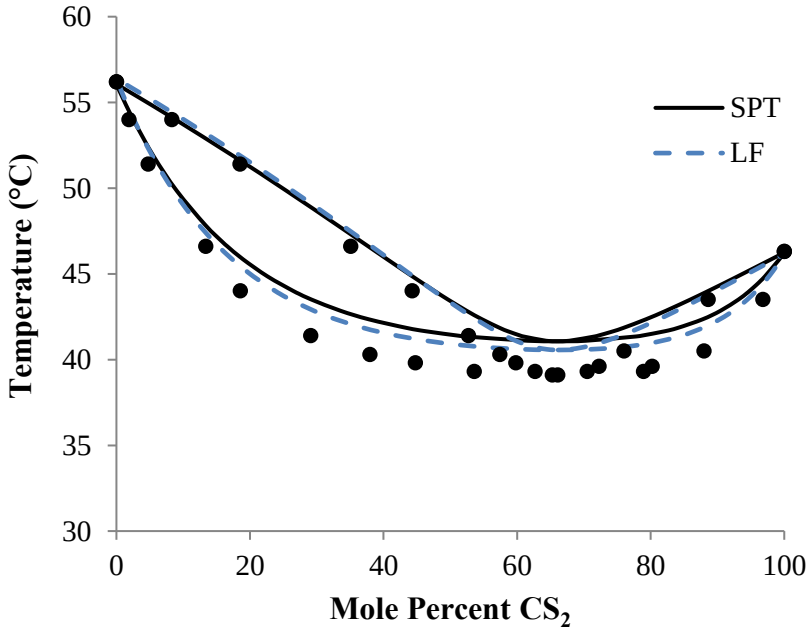

Figure 3.12: Comparison of Acetone/CS_2 liquid/vapor coexistence curves at atmospheric pressure

3.7 LIQUID/VAPOR EQUILIBRIUM FOR A POLAR/POLAR MIXTURE

Though both the SPT chain and LF models base their configurational energies on an R^{-6} potential they were reasonably capable of predicting liquid/vapor equilibrium compositions for mixtures of 2,6-dimethylpyridine, a weak base, and phenol, a weak acid. ζ_{12} values were determined by fitting the maximum boiling azeotrope temperature of 185.5°C at 760 mm Hg [45]. The phase diagrams at 760 mm Hg and at 200 mm Hg in Figure 3.13 were both calculated using the values of ζ_{12} fit at 760 mm Hg. Experimental points in Figure 3.13 are taken from reference [46]. Both the SPT and LF models yielded similar results. ΔP_{12}^{*} for this mixture is negative, indicating two cross (2,6-dimethylpyridine-phenol) interactions are energetically more favorable than the sum of the like (phenol-phenol and 2,6-dimethylpyridine/2,6-dimethylpyridine) interactions.

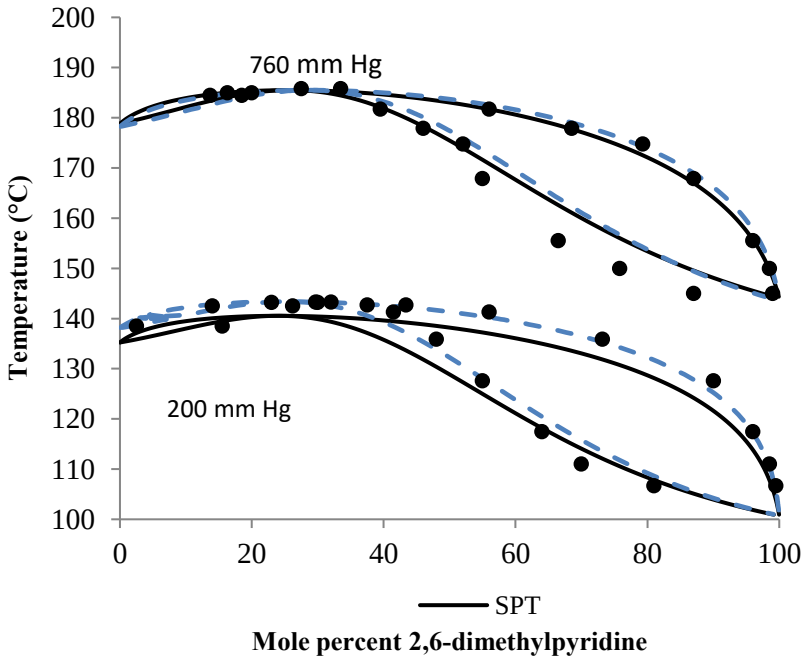

Figure 3.13: Liquid/Vapor phase diagram of 2,6-dimethyl-pyridine and phenol

3.8 POLYMER/SOLVENT SYSTEMS

At high temperatures, the $-\kappa\beta v^* P_\phi^2 \kappa P_\phi^2/\eta$ contribution to (2.34) may drive binary phase separation if equation of state parameters are sufficiently different (as in polymer/solvent solutions). Coexistence curves of this type reach local minima lower critical solution temperatures (LCSTs). As with the UCSTs discussed in Section 3.6, the spinodal gives the general character of the liquid/liquid phase diagram, and LCSTs may be obtained directly from spinodal calculations. To test the ability of the SPT model to describe LCST behavior and polymer/solvent solutions, spinodal curves were calculated for solutions of n-hexane and polyisobutlyene (PIB) that exhibit LCSTs. The molecular weight of the PIB used in calculations was 1.5×10^6 which exhibits an LCST in n-hexane solution at 128°C[47].

The upper-left pane in Figure 3.14 is the spinodal curve for the PIB/hexane system calculated with the SPT model by approximating the interaction pressure with the geometric mean, ($\zeta_{12} = 1$). With this interaction pressure, the SPT model predicts immiscibility at all temperatures and reasonable compositions. The spinodal (and corresponding phase diagram) is an asymmetric hourglass type which occurs when the LCST and UCST curves intersect. The PIB/hexane spinodal for the LF model at $\zeta_{12} = 1$ is shown in the lower-left of Figure 3.14. It does not predict the phase instability seen with the SPT model, and calculates an LCST of 59.3°C.

Increasing the value of ζ_{12} makes 1,2 interactions more energetically favorable, and causes the SPT hourglass phase diagram to split into an LCST and UCST type diagram. For the SPT model, separation occurs near a ζ_{12} of 1.0054 (upper right of Figure 3.14). The UCST is the local maximum of the concave down branch and has a value of -86.9°C. The LCST is the local minimum of the concave up branch and has a

value of -69.1°C. At $\zeta_{12} = 1.02$, the SPT UCST drops to about -197°C while the LCST increases to +15.0°C (not shown in Figure 3.14).

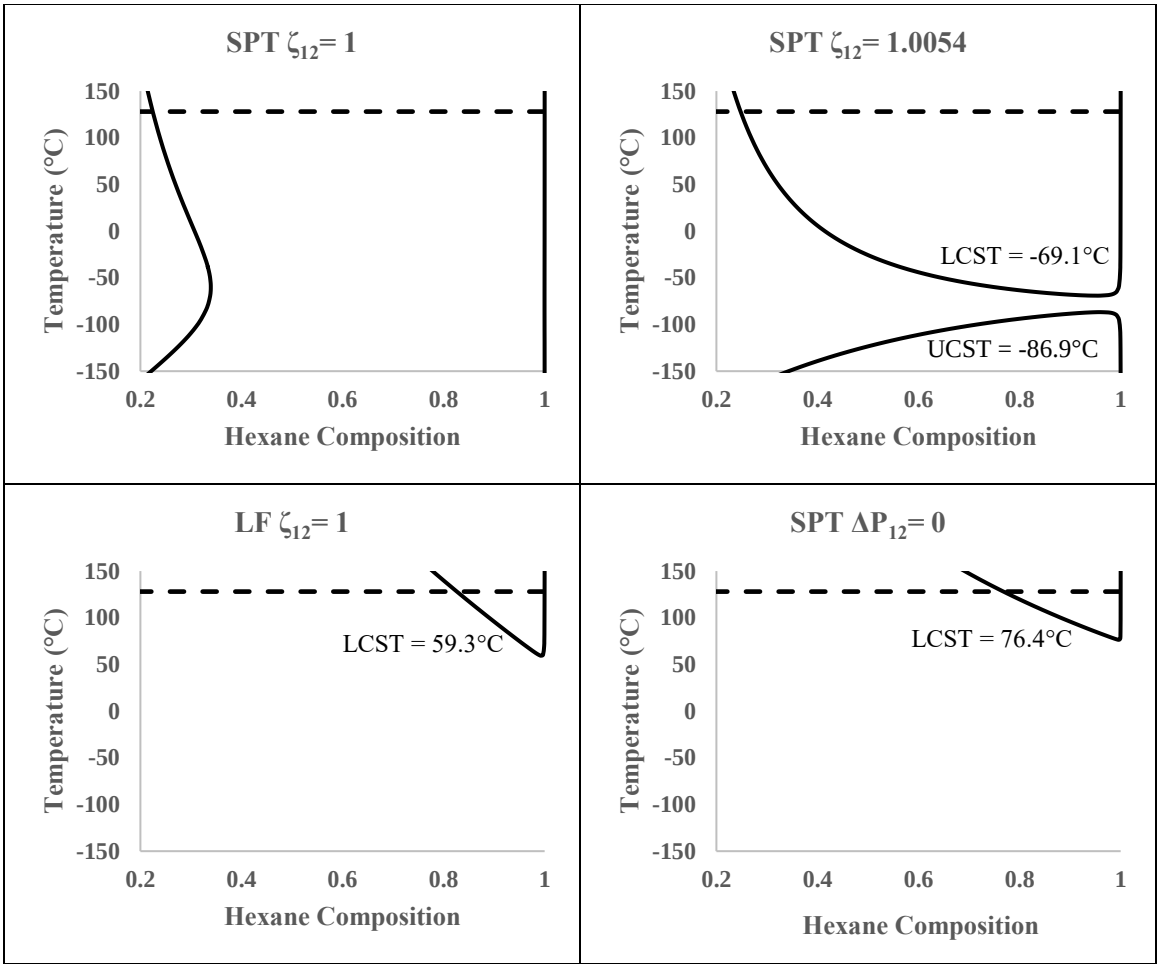

Figure 3.14: Calculated spinodal curves for the PIB/n-hexane system at atmospheric pressure. CSTs are indicated when applicable. Solid curves are spinodals calculated with the indicated model and ζ_{12} or ΔP_{12}^*. Dashed horizontal lines indicate the experimental value of 128°C.

The LCST continues to increase as the polymer/solvent interactions are made more favorable. When $\Delta P_{12}^* = 0$, two 1,2 interactions are as favorable as the sum of a 1,1 and a 2,2 interaction. When $\Delta P_{12}^* \leq 0$, the only negative contribution to inequality

(2.34) that may drive liquid/liquid phase separation is $-\kappa\beta\eta P_\phi^2$. The SPT LCST for the PIB/hexane system reaches a maximum of about 89.26°C at $\zeta_{12} \sim 1.219$. The SPT model was unable to attain the experimental LCST of 128°C[47]. The LF model does reach the correct LCST at $\zeta_{12} = 1.035$.

The LCSTs reported in [18], using a characteristic energy ε^* based mixing rule, instead of the P^* based rule, better agreed with measured critical solution temperatures. To make a fair comparison with [18], inequality (2.34) was rederived for the SPT chain model with this $\varepsilon^* = v^* P^*$ based mixing rule and applied to the PIB/n-hexane system. With this ε^* mixing rule, the LF model predicted an LCST of 99°C at $\zeta_{12} = \varepsilon_{12}^*/\sqrt{\varepsilon_1^* \varepsilon_2^*} = 1$, an improvement over the LF LCST with a P^*based mixing rule. When this ε_{12}^* mixing rule was attempted for SPT, the calculated LCST for $\zeta_{12} = 1$ was -228.5°C, an improvement only in the sense that it no longer predicted complete immiscibility.

These spinodal calculations were repeated with the SPT model for different polymers and solvents with the P^* based mixing rule. All polymer/solvent spinodals predicted the type of immiscibility shown in the upper-left pane of Figure 3.14 for $\zeta_{12} = 1$, and underpredicted LCSTs at values of ζ_{12} large enough to separate the LCST and UCST curves. The behavior was even observed for model spinodal calculations for solutions with linear polyethylene, whose equation of state parameters in Appendix A are closest to those of small molecules. These results strongly contrast LF calculations of the same systems that predict homogeneous phase stability below a well-defined LCST for polymer/solvent systems.

3.9 CHAPTER SUMMARY AND CONCLUSIONS

The SPT chain model was intended to model the fluid systems whose properties are successfully predicted by the LF model. Both models require the same number of parameters, the potential energy derivation is identical for both models, and the spinodal inequalities of both models predict the same types of phase instabilities. SPT was repeatedly compared with LF throughout this chapter, yielding mixed results. Both models were comparable when applied to mixtures of small, similarly sized molecules, but the LF model was superior when applied to polymer solutions. In Chapter 4 the ability of Scaled Particle Theory to model binary mixtures of differently sized hard spheres, and the approximation used to extend the individual sphere insertion probability to long chains are discussed.

Chapter 4: SPT Shortcomings and other Models for Hard Sphere Solutions and Hard Sphere Chain Solutions*

4.1 INTRODUCTION

For most of the solutions of molecules with low r, SPT is neither evidently superior nor inferior to the LF model. Inequality (2.34) predicts the same types of phase instability as the LF spinodal given in [19], and if the SPT HS volumes of each component are similar, the SPT and LF spinodals have a similar functional appearance. Both models characterize pure fluids with three independent parameters (r, v^*, P^*). Binary mixtures require only one additional parameter, P_{12}^* (or equivalently ζ_{12}), and parameters for both models have similar molecular interpretations.

SPT was best at predicting some properties of small, Group I fluids. Many of these types of molecules, such as methane, can reasonably be considered a single attractive hard sphere for the purpose of the SPT model. The success of this model with respect to unchained spheres may be attributed to its statistical thermodynamic foundation. In the absence of attractive interactions $\left(P_{ij}^* = 0\right)$, equation (2.14) for mixtures of hard spheres $(r_1, r_2 \ldots r_i = 1)$ reduces to the Percus-Yevick compressibility equation of state generalized for mixtures[31,48]:

$$\frac{P}{\rho kT} = (1+y)\left(1 + 3\frac{\sigma_{-1}\sigma_{-2}}{\sigma_{-3}}y + 3\frac{\sigma_{-1}}{\sigma_{-3}}y^2\right) \tag{4.1}$$

* As with Chapters 2 and 3, this material was partly published as: Sean P. O'Keefe, and Isaac C. Sanchez, "Scaled Particle Theory of solutions: Comparison with Lattice Fluid model" *Fluid Phase Equilibria* 433, 67 (2017)[16]. Sean Patrick O'Keefe is the primary author.

When all spheres have equivalent diameters, equation (4.1) reduces to the more familiar Percus-Yevick compressibility equation of state for a pure HS fluid:

$$\frac{P}{\rho kT} = \frac{1+\eta+\eta^2}{(1-\eta)^3} \tag{4.2}$$

Equation (4.2) was used as $1 + H_S(\rho)$ in Chapter 1. When a mean-field potential energy contribution was added to (4.2), this simplified SPT model proved excellent at calculating first-order thermodynamic properties for Group I liquids in Table 1.1[1].

The LF model was clearly superior at predicting properties of polymer/solvent solutions. In addition to the difference in chain length parameters $\left(r_{\text{polymer}} \gg r_{\text{solvent}}\right)$, Appendix A tabulates significant qualitative differences in value between SPTT solvent and polymer molecular parameters. In the LF model, characteristic temperatures (T^*) are of $O(10^2)$ K for both small and polymeric molecules[17,19]. In the SPT model, small molecules have T^*s of $O(10^3)$ K, and polymer molecules have larger T^*s, typically a factor of three to five times those of chemically similar small molecules. For the SPT model small nonpolar aromatics in Table A1 have T^*s from 5×10^3 to 6×10^3 K, while in Table A2 polystyrene and poly(o-methyl styrene) both have $T^* > 2\times10^4$. Corresponding LF T^*s range from 5×10^2 to 6×10^2 K for small aromatics[17], while the LF T^*s for polystyrene and poly(o-methyl styrene) are 773 K and 796 K respectively[49].

SPT characteristic pressures P^*s for both polymers and small molecules are are $O(10^3)$ MPa. Since $T^* \propto P^* v^*$, the difference in characteristic temperatures manifests as a significant difference in segment volume. The polymer sphere volumes are about 8–10 times that of small molecule v^*. One should expect that in a homologous series of

molecules, such as the n-alkanes, the fundamental monomer size of the model should remain invariant with chain length, but for n-pentadecane (the longest n-alkane in Table A1) σ is 3.91 Å ($v^* = 36$ cm^3/mol) while linear polyethylene has a σ of 6.35 Å ($v^* = 154$ cm^3/mol). The linear polyethylene sphere volume v^* is therefore 4.28 times that of the n-pentadecane v^*.

Section 4.2 examines the effects of sphere size differences, composition, and η on the SPT model's ability to predict insertion probabilities in binary mixtures of unchained hard spheres. In section 4.3, models that improve upon the SPT model by explicitly accounting for chain connectivity are compared to SPT for the insertion probability of chains of spheres and predicted polymer/solvent critical solution temperatures.

For a system of hard spheres or hard sphere chains without weak attractive interactions, the compressibility factor is a function of density only $\left(Z = Z(\eta)\right)$. All models discussed calculate insertion probabilities through integration of the isothermal Gibbs-Duhem equation followed by differentiation. The probability of inserting species 1 in a binary mixture of hard sphere chains from a given equation of state is:

$$-\ln \mathbf{P}_1 = (Z-1)\frac{r_1 v_1^*}{r v^*} + \int_0^\eta \frac{(Z-1)}{\eta} d\eta + \frac{\phi_2 v_1^*}{v^*} \int_0^\eta \frac{\partial}{\partial \phi_1}\left(\frac{Z-1}{\eta}\right)_{T,P,\eta} d\eta \qquad (4.3)$$

$-\ln \mathbf{P}_2$ may be found by interchanging the 1 and 2 subscripts in (4.3).

4.2 BINARY MIXTURES OF UNCHAINED HARD SPHERES

Previous work indicated that SPT tends to underpredict insertion probabilities of unchained hard spheres ($r_1, r_2 = 1$)[50]. SPT insertion probability for unchained hard spheres are here compared with both simulated insertion probability (or equivalent growth probabilities) data, and insertion probabilities derived of other models.

4.2.1 Extended Carnahan-Starling Model

The extended Carnahan-Starling model (eCS) for HS mixtures was developed from exact requirements in the limit of a point particle/HS mixture system, and the form of the radial distribution function at contact obtained with a Percus-Yevick approximation[51] applied to the Carnahan-Starling model for a one component HS system[52]. The eCS EOS is given by:

$$Z = 1 + \left[1 + 3\frac{\sigma_{-1}\sigma_{-2}}{\sigma_{-3}}\right]y + \left[3\frac{\sigma_{-1}\sigma_{-2}}{\sigma_{-3}} + 3\frac{\sigma_{-1}^3}{\sigma_{-3}}\right]y^2 + \left[\frac{\sigma_{-1}\sigma_{-2}}{\sigma_{-3}} + \frac{\sigma_{-1}^3}{\sigma_{-3}}\right]y^3 \qquad (4.4)$$

Equation (4.4) is more accurate[51,53] than the Boublík-Mansoori-Carnahan-Starling-Leland[54,55] equation of state. The insertion probability for species 1 in a binary HS mixture found by using (4.4) in equation (4.3) is:

$$\begin{aligned} -\ln \mathbf{P}_1 = {} & (1 + \sigma_1\sigma_{-1} + \sigma_1^2\sigma_{-2} + 4\sigma_1^3\sigma_{-1}^3 - \sigma_1^3\sigma_{-1}\sigma_{-2} - 6\sigma_1^2\sigma_{-1}^2)\ln(1+y) \\ & + (2\sigma_1\sigma_{-1} + 2\sigma_1^2\sigma_{-2} + 6\sigma_1^2\sigma_{-1}^2 + \sigma_1^3\sigma_{-1}\sigma_{-2} + \sigma_1^3\sigma_{-3} - 4\sigma_1^3\sigma_{-1}^3)y \\ & + \frac{1}{2}(\sigma_1\sigma_{-1} + \sigma_1^2\sigma_{-2} + 3\sigma_1^2\sigma_{-1}^2 + 5\sigma_1^3\sigma_{-1}\sigma_{-2} + 4\sigma_1^3\sigma_{-1}^3)y^2 \\ & + (\sigma_1^3\sigma_{-1}\sigma_{-2} + \sigma_1^3\sigma_{-1}^3)y^3 \end{aligned} \qquad (4.5)$$

4.2.2 Fourth Virial Expansion

Expanding in powers of η a fourth virial expansion gives for Z:

$$Z = 1 + b_2\eta + b_3\eta^2 + b_4\eta^3 \ldots \tag{4.6}$$

A virial expansion was selected for comparison because unlike SPT, virial expansions consistently overpredict insertion probabilities. The exact second and third virial coefficients for HS mixtures are given as[56]:

$$b_2 = 1 + 3\frac{\sigma_{-1}\sigma_{-2}}{\sigma_{-3}} \tag{4.7}$$

$$b_3 = 1 + 6\frac{\sigma_{-1}\sigma_{-2}}{\sigma_{-3}} + 3\frac{\sigma_{-1}^3}{\sigma_{-3}} \tag{4.8}$$

Using an exact composition dependence of partial virial coefficients and numerical fitting to polynomial functions of the diameter ratio, the fourth virial coefficient in a binary HS mixture may be approximated as[53,57,58]:

$$b_4 = (\sigma_1^3\sigma_{-3})^3\left[x_2^4 b_4^{(0)} + 4x_1x_2^3 b_4^{(1)} + 6x_1^2x_2^2 b_4^{(2)} + 4x_1^3x_2 b_4^{(3)} + x_1^4 b_4^{(4)}\right] \tag{4.9}$$

b_4^k are the partial virial coefficients given by:

$$\begin{aligned}
b_4^{(0)} &= 18.365\left(\frac{\sigma_2}{\sigma_1}\right)^9 \\
b_4^{(1)} &= \frac{1}{4}\left(\frac{\sigma_2}{\sigma_1}\right)^6\left[30 + 33.042\left(\frac{\sigma_2}{\sigma_1}\right) + 9.417\left(\frac{\sigma_2}{\sigma_1}\right)^2 + \left(\frac{\sigma_2}{\sigma_1}\right)^3\right] \\
b_4^{(2)} &= \frac{1}{2}\left(\frac{\sigma_2}{\sigma_1}\right)^3\left[4 + 14.365\left(\frac{\sigma_2}{\sigma_1}\right) + 14.365\left(\frac{\sigma_2}{\sigma_1}\right)^2 + 4\left(\frac{\sigma_2}{\sigma_1}\right)^3\right] \\
b_4^{(3)} &= \frac{1}{4}\left[1 + 9.417\left(\frac{\sigma_2}{\sigma_1}\right) + 33.042\left(\frac{\sigma_2}{\sigma_1}\right)^2 + 30\left(\frac{\sigma_2}{\sigma_1}\right)^3\right] \\
b_4^{(4)} &= 18.365
\end{aligned} \tag{4.10}$$

The fourth virial insertion probability for a sphere of diameter σ_1 in a binary HS mixture is given by:

$$\begin{aligned} -\ln \mathbf{P}_1 = {} & [3\sigma_1\sigma_{-1} + 3\sigma_1^2\sigma_{-2} + \sigma_1^3\sigma_{-3} + 1]\eta \\ & + \left[3\sigma_1\sigma_{-1} + 3\sigma_1^2\sigma_{-2} + \sigma_1^3\sigma_{-3} + \frac{9}{2}\sigma_1^2\sigma_{-1}^2 + 3\sigma_1^3\sigma_{-1}\sigma_{-2} + \frac{1}{2}\right]\eta^2 \\ & + \left[\frac{4}{3}x_1^3 b_4^{(4)} + 4x_1^2 x_2 b_4^{(3)} + 4x_1 x_2^2 b_4^{(2)} + \frac{4}{3}x_2^3 b_4^{(1)}\right]\sigma_1^9\sigma_{-3}^3\eta^3 \end{aligned} \tag{4.11}$$

The insertion probability of component (2) is found by interchanging the subscripts 1 and 2 in both (4.11) and each of the $b_4^{(k)}$.

Expanding the SPT insertion probability in η about $\eta = 0$ gives:

$$\begin{aligned} -\ln \mathbf{P}_1 = {} & [3\sigma_1\sigma_{-1} + 3\sigma_1^2\sigma_{-2} + \sigma_1^3\sigma_{-3} + 1]\eta \\ & + \left[3\sigma_1\sigma_{-1} + 3\sigma_1^2\sigma_{-2} + \sigma_1^3\sigma_{-3} + \frac{9}{2}\sigma_1^2\sigma_{-1}^2 + 3\sigma_1^3\sigma_{-1}\sigma_{-2} + \frac{1}{2}\right]\eta^2 \\ & + \left[3\sigma_1\sigma_{-1} + 3\sigma_1^2\sigma_{-2} + \sigma_1^3\sigma_{-3} + 9\sigma_1^2\sigma_{-1}^2 + 6\sigma_1^3\sigma_{-1}\sigma_{-2} + 3\sigma_1^3\sigma_{-1}^3 + \frac{1}{3}\right]\eta^3 \end{aligned} \tag{4.12}$$

SPT correctly predicts the second and third virial coefficients, but its fourth virial coefficient is $1 + 9\frac{\sigma_{-1}\sigma_{-2}}{\sigma_{-3}} + 9\frac{\sigma_{-1}^3}{\sigma_{-3}}$ which tends to be greater than b_4 calculated with equations (4.9) and (4.10).

4.2.3 Model Comparisons with Simulation Data

Figures 4.1–4.5 compare insertion probabilities measured in simulations with those calculated with SPT (2.6), eCS (4.5), and the fourth virial expansion (4.11). Figures 4.1–4.4 use data taken from reference [59], and Figure 4.5 uses data taken from reference [60]. Both references employed particle growth methods instead of direct insertion of the HS with diameter σ.

Trends in insertion probabilities may qualitatively be explained through the availability of cavities large enough to accommodate a sphere either of diameter σ_1 (Figures 4.1, 4.3, and 4.5) or σ_2 (Figures 4.2 and 4.4). At a fixed mole fraction of either large or small spheres, η is modified by changing the available empty space, and insertion probability decreases as η increases in Figures 4.3–4.5. In Figures 4.1 and 4.2, insertion probabilities decrease as the composition of the smaller sphere increases. Small spheres are better at distributing occupied volume than larger spheres, while large spheres concentrate the occupied volume. There are more clusters of large cavities and HS insertion probability is higher in the large sphere composition limit at $\eta = 0.35$, than in the small sphere composition limit at $\eta = 0.35$. This HS volume dispersion is also the reason why Figure 4.4 shows a greater insertion probability for HS of type 2 when $\sigma_2/\sigma_1 = 0.3$ than when $\sigma_2/\sigma_1 = 0.6$, even though $\sigma_2/\sigma_1 = 0.6$ has a relatively smaller species 2. This is also why in Figure 4.2, the $\sigma_2/\sigma_1 = 0.3$ has a greater insertion probability than the $\sigma_2/\sigma_1 = 0.6$ curve near the limit concentrated in larger spheres, but the $\sigma_2/\sigma_1 = 0.6$ insertion probability is greater when the mixture is concentrated in small spheres. Since all curves in Figure 4.5 are at the infinite dilution limit, average cavity size relative to solvent size only depends on η, and insertion probability simply decreases as solute size increases.

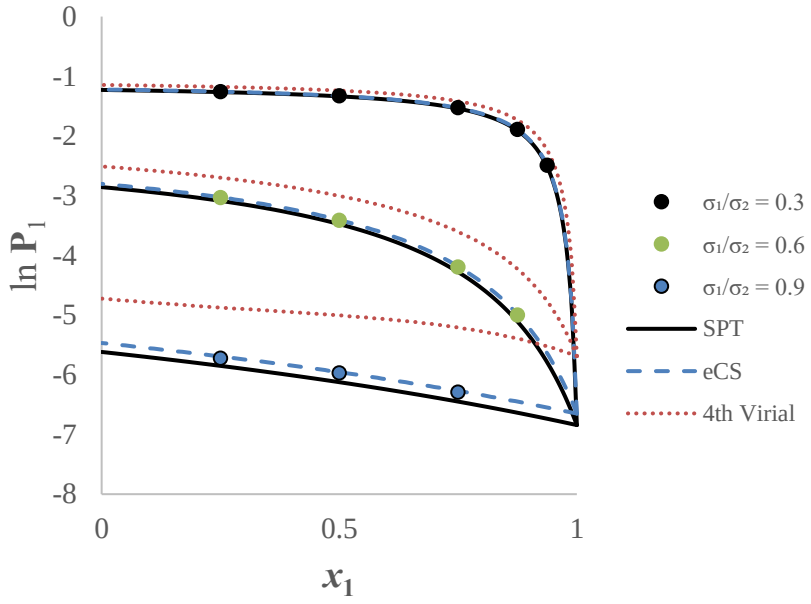

Figure 4.1: Insertion probability of smaller sphere(1) in a binary HS mixture versus mole fraction of small sphere(x_1) at $\eta = 0.35$

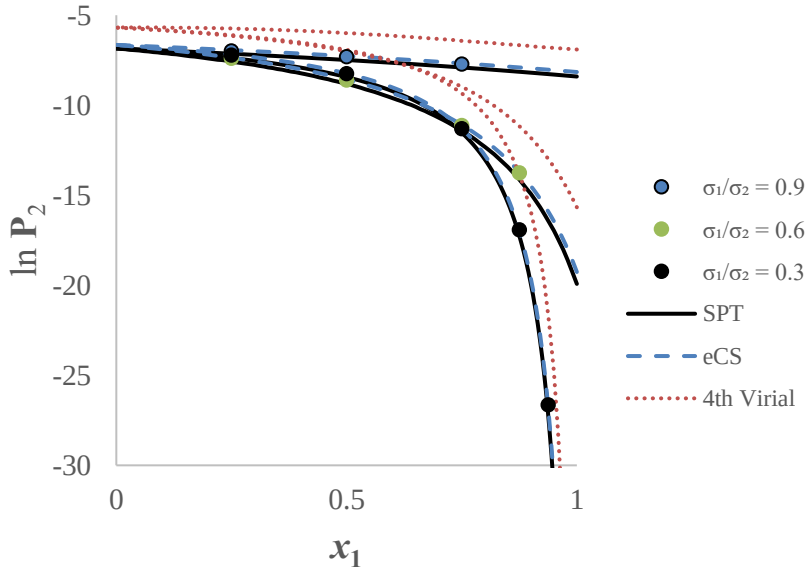

Figure 4.2: Insertion probability of larger sphere(2) in a binary HS mixture versus mole fraction of small sphere(x_1) at $\eta = 0.35$

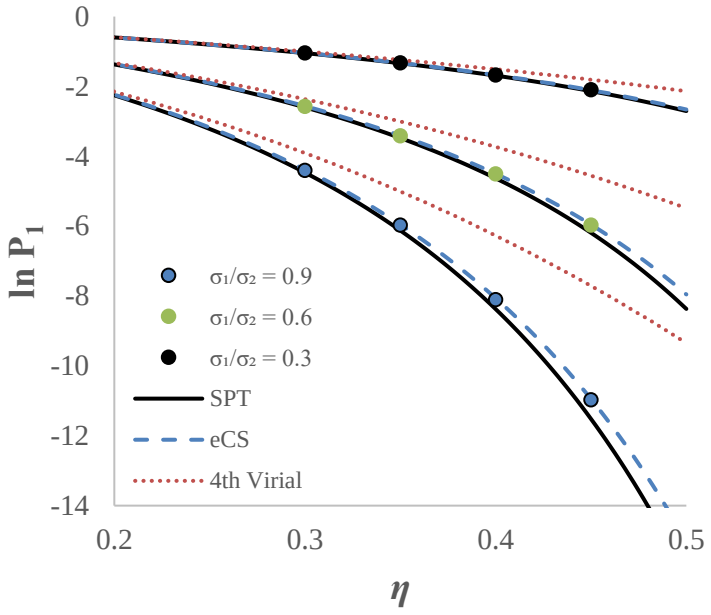

Figure 4.3: Effect of η on insertion probability of smaller sphere(1) in a binary HS at $x_1 = x_2 = 0.5$

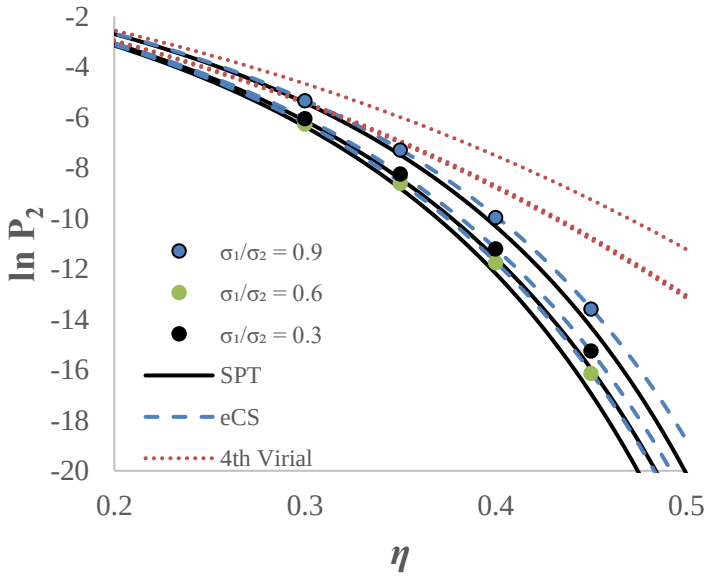

Figure 4.4: Effect of η on insertion probability of larger sphere(2) in a binary HS at $x_1 = x_2 = 0.5$

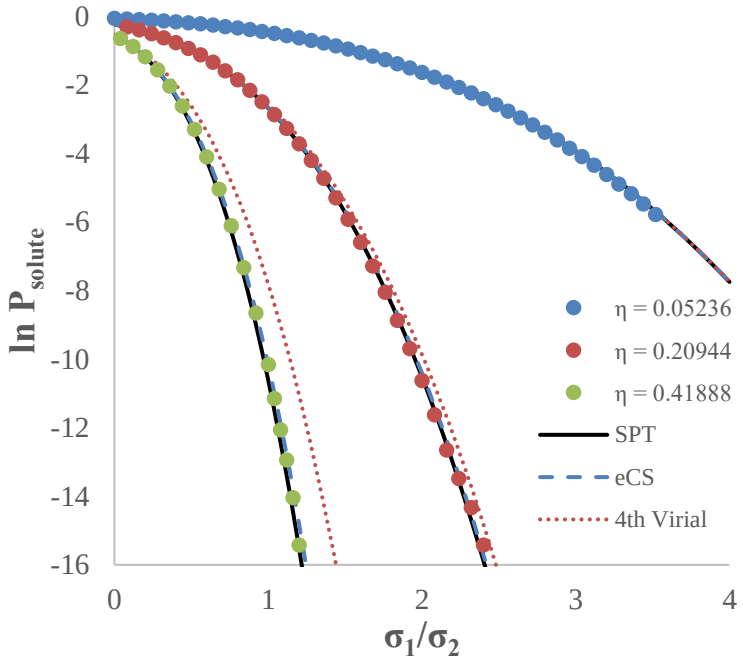

Figure 4.5: Solute insertion probability at infinite dilution as a function of the ratio of solute(1) diameter to solvent(2) diameter

In all five plots, the fourth virial expansion overestimates insertion probability as expected. SPT predicts lower insertion probabilities than the other models, and in all but the two lower η curves in Figure 4.5 underpredicts simulated probabilities. The eCS model is consistently best. At its worst the eCS model curves appear to superpose with the SPT curves, but in Figure 4.4 eCS remains accurate over the entire η range for each σ_2/σ_1 while SPT is unsatisfactory at predicting insertion probabilities of large spheres at $\eta > 0.4$.

4.3 Models for Hard Sphere Chains

For individual unchained spheres, Section 4.2 showed that SPT tends to predict lower insertion probabilities than reported simulation data. Ignoring chain connectivity,

as in equation (2.5), introduces this error upon insertion of every SPT sphere in the chain of r spheres. The eCS model better calculated insertion probability data, and if applied to equations (2.5–13) may yield a better model for HS chains than the SPT model. Simple analytical models that explicitly account for neighboring spheres at contact might also improve on the SPT chain insertion probability.

4.3.1 Extended Carnahan-Starling Chains

Substituting equation (4.5) into equation (2.5) gives the insertion probability for an eCS chain of r_i tangent hard spheres (THS), with diameter σ_i, without short-ranged attractive interactions:

$$-\ln \mathbf{P}_i = -r_i \ln \mathbf{P}_{HS,i} = r_i \begin{bmatrix} \begin{pmatrix} 1+\sigma_1\sigma_{-1}+\sigma_1^2\sigma_{-2} \\ +4\sigma_1^3\sigma_{-1}^3-\sigma_1^3\sigma_{-1}\sigma_{-2}-6\sigma_1^2\sigma_{-1}^2 \end{pmatrix}\ln(1+y) \\ +\begin{pmatrix} 2\sigma_1\sigma_{-1}+2\sigma_1^2\sigma_{-2}+6\sigma_1^2\sigma_{-1}^2 \\ +\sigma_1^3\sigma_{-1}\sigma_{-2}+\sigma_1^3\sigma_{-3}-4\sigma_1^3\sigma_{-1}^3 \end{pmatrix} y \\ +\begin{pmatrix} \frac{1}{2}\sigma_1\sigma_{-1}+\frac{1}{2}\sigma_1^2\sigma_{-2}+\frac{3}{2}\sigma_1^2\sigma_{-1}^2 \\ +\frac{5}{2}\sigma_1^3\sigma_{-1}\sigma_{-2}+2\sigma_1^3\sigma_{-1}^3 \end{pmatrix} y^2 \\ +(\sigma_1^3\sigma_{-1}\sigma_{-2}+\sigma_1^3\sigma_{-1}^3)y^3 \end{bmatrix} \quad (4.13)$$

With equations (2.12) and (2.13), the eCS chain EOS is given as:

$$Z = 1 + r\left[\left(1+3\frac{\sigma_{-1}\sigma_{-2}}{\sigma_{-3}}\right)y + \left(3\frac{\sigma_{-1}\sigma_{-2}}{\sigma_{-3}}+3\frac{\sigma_{-1}^3}{\sigma_{-3}}\right)y^2 + \left(\frac{\sigma_{-1}\sigma_{-2}}{\sigma_{-3}}+\frac{\sigma_{-1}^3}{\sigma_{-3}}\right)y^3\right] \quad (4.14)$$

4.3.2 Chiew Type Models for Tangent Hard Sphere Chains

To investigate the effects of segment connectivity, the SPT chain model was compared to three Chiew Percus-Yevick (PY) type chain models[61,62]. These models

retain the bulk HS PY type contribution to the equation of state of the SPT model, but their equations of state contain additional contributions from the bonding of segments derived from Baxter's solution of the Ornstein-Zernike equation with a PY approximation for hard spheres with infinitely adhesive surfaces[63].

Percus-Yevick Compressibility (PY-C) Model

This model uses a Percus-Yevick radial distribution function to account for chaining and Equation (4.1) as the HS contribution. The PY-C EOS is given by:

$$Z = 1 + y + r\left[\frac{3}{2}\frac{\sigma_{-1}\sigma_{-2}}{\sigma_{-3}}y + \left(\frac{3}{2}\frac{\sigma_{-1}\sigma_{-2}}{\sigma_{-3}} + 3\frac{\sigma_{-1}^3}{\sigma_{-3}}\right)y^2 + 3\frac{\sigma_{-1}^3}{\sigma_{-3}}y^3\right] + \frac{3}{2}y(1+y)\sigma_{-1}\sum_i x_i\sigma_i \tag{4.15}$$

The insertion probability found through Equation (4.3) is:

$$-\ln \mathbf{P}_i = \ln(1+y) + 3r_i\sigma_i^3\sigma_{-1}^3y^3 + \left[\frac{9}{2}r_i\sigma_i^2\sigma_{-1}^2 + \frac{3}{2}r_i\sigma_i^3\sigma_{-1}\sigma_{-2} + \frac{3}{2}\sigma_{-1}\frac{r_iv_i^*}{rv^*}\sum_j x_j\sigma_j\right]y^2 + \left[\frac{r_iv_i^*}{rv^*} + \frac{3}{2}r_i\sigma_i\sigma_{-1} + \frac{3}{2}r_i\sigma_i^2\sigma_{-2} + \frac{3}{2}\left(\frac{\pi}{6}\right)\frac{r_i\sigma_i^2}{rv^*}\sum_j x_j\sigma_j + \frac{3}{2}\sigma_i\sigma_{-1}\right]y \tag{4.16}$$

Percus-Yevick Carnahan-Starling (PY-CS) Model

This model uses the Percus-Yevick radial distribution function for connectivity, but uses the more accurate Boublík-Mansoori-Carnahan-Starling-Leland (BMCSL) equation of state[54,55] for the HS contribution. The resulting EOS is

$$Z = 1 + y + r\left[\frac{3}{2}\frac{\sigma_{-1}\sigma_{-2}}{\sigma_{-3}}y + \left(\frac{3}{2}\frac{\sigma_{-1}\sigma_{-2}}{\sigma_{-3}} + 3\frac{\sigma_{-1}^3}{\sigma_{-3}}\right)y^2 + 2\frac{\sigma_{-1}^3}{\sigma_{-3}}y^3\right] + \frac{3}{2}y(1+y)\sigma_{-1}\sum_i x_i\sigma_i \tag{4.17}$$

The only difference between (4.17) and (4.15) is the coefficient of the y^3 term.

The insertion probability found through Equation (4.3) is:

$$\begin{aligned} -\ln \mathrm{P}_i = {} & [1 - 3r_i\sigma_i^2\sigma_{-1}^2 + 2r_i\sigma_i^3\sigma_{-1}^3]\ln(1+y) \\ & + \left[\begin{array}{l} \frac{r_i v_i^*}{r v^*} + 3r_i\sigma_i^2\sigma_{-1}^2 - 2r_i\sigma_i^3\sigma_{-1}^3 + \frac{3}{2}r_i\sigma_i^2\sigma_{-2} + \frac{3}{2}r_i\sigma_i\sigma_{-1} \\ + \frac{3}{2}\left(\frac{\pi}{6}\right)\left(\frac{r_i\sigma_i^2}{r v^*}\right)\sum_j x_j\sigma_j + \frac{3}{2}\sigma_{-1}\sigma_i \end{array}\right] y \\ & + \left[\begin{array}{l} 3r_i\sigma_i^2\sigma_{-1}^2 + r_i\sigma_i^3\sigma_{-1}^3 + \frac{3}{2}r_i\sigma_i^3\sigma_{-1}\sigma_{-2} \\ + \frac{3}{2}\frac{r_i v_i}{r v^*}\sigma_{-1}\sum_j x_j\sigma_j \end{array}\right] y^2 + 2r_i\sigma_i^3\sigma_{-1}^3 y^3 \end{aligned} \tag{4.18}$$

Perturbed Hard Chain Theory (PHCT)

Perturbed Hard Chain Theory uses the BMCSL equation of state and radial distribution function for the connected HS chain[64]. The resulting EOS is:

$$Z = 1 + y + r\left[\frac{3}{2}\frac{\sigma_{-1}\sigma_{-2}}{\sigma_{-3}}y + \left(\frac{3}{2}\frac{\sigma_{-1}\sigma_{-2}}{\sigma_{-3}} + \frac{5}{2}\frac{\sigma_{-1}^3}{\sigma_{-3}}\right)y^2 + \frac{3}{2}\frac{\sigma_{-1}^3}{\sigma_{-3}}y^3\right] + \frac{3}{2}y(1+y)\sigma_{-1}\sum_i x_i\sigma_i + \frac{1}{2}y^2(1+y)\sigma_{-1}^2\sum_i x_i\sigma_i^2 \tag{4.19}$$

The insertion probability found through Equation (4.3) is:

$$
\begin{aligned}
-\ln \mathbf{P}_i = {} & [1 - 3r_i\sigma_i^2\sigma_{-1}^2 + 2r_i\sigma_i^3\sigma_{-1}^3]\ln(1+y) \\
& + \left[\begin{array}{l} \frac{r_i v_i^*}{r v^*} + \frac{3}{2} r_i\sigma_i^2\sigma_{-2} + \frac{3}{2} r_i\sigma_i\sigma_{-1} + 3r_i\sigma_i^2\sigma_{-1}^2 \\ -2r_i\sigma_i^3\sigma_{-1}^3 + \frac{3}{2}\left(\frac{\pi}{6}\right)\left(\frac{r_i\sigma_i^2}{r v^*}\right)\sum_j x_j\sigma_j + \frac{3}{2}\sigma_{-1}\sigma_i \end{array}\right] y \\
& + \left[\begin{array}{l} \frac{3}{2} r_i\sigma_i^3\sigma_{-1}\sigma_{-2} + r_i\sigma_i^3\sigma_{-1}^3 + \frac{9}{4} r_i\sigma_i^2\sigma_{-1}^2 + \frac{1}{4}\sigma_{-1}^2\sigma_i^2 \\ + \frac{1}{2}\sigma_{-1}\left(\frac{\pi}{6}\right)\left(\frac{r_i\sigma_i^2}{r v^*}\right)\sum_j x_j\sigma_j^2 + \frac{3}{2}\sigma_{-1}\left(\frac{r_i v_i}{r v^*}\right)\sum_j x_j\sigma_j \end{array}\right] y^2 \\
& + \left[\frac{3}{2} r_i\sigma_i^3\sigma_{-1}^3 + \frac{1}{2}\left(\frac{r_i v_i^*}{r v^*}\right)\sigma_{-1}^2\sum_j x_j\sigma_j^2\right] y^3
\end{aligned}
\tag{4.20}
$$

4.3.3 Comparison of Models for Long Chain Insertion Probability

Hard chain insertion probabilities for the SPT and Chiew models were compared using equivalent chain and segment volume ratios among models. For the solvent(1), polymer(2) system, segment diameter ratio σ_2/σ_1 was set to 2.3, and chain lengths were set $r_1 = 5$, $r_2 = 1{,}000$. All values correspond with polymer/solvent parameters fit for the SPT model. The infinite dilution limit, $\phi_1 \to 1$, was also applied to correspond with the limit where SPT was least accurate[50].

Insertion Probabilities under these conditions are plotted in Figure 4.6 versus the occupied volume fraction. SPT calculates much lower insertion probabilities than the other models at all η, and eCS agrees better with SPT than any of the Chiew models. Since the eCS chain model ignores chain connectivity in the same manner as the SPT chain model, Figure 4.6 shows that the chain connectivity approximation more greatly contributed to insertion probability effect in the polymer/solvent system than any error in individual sphere insertion probability.

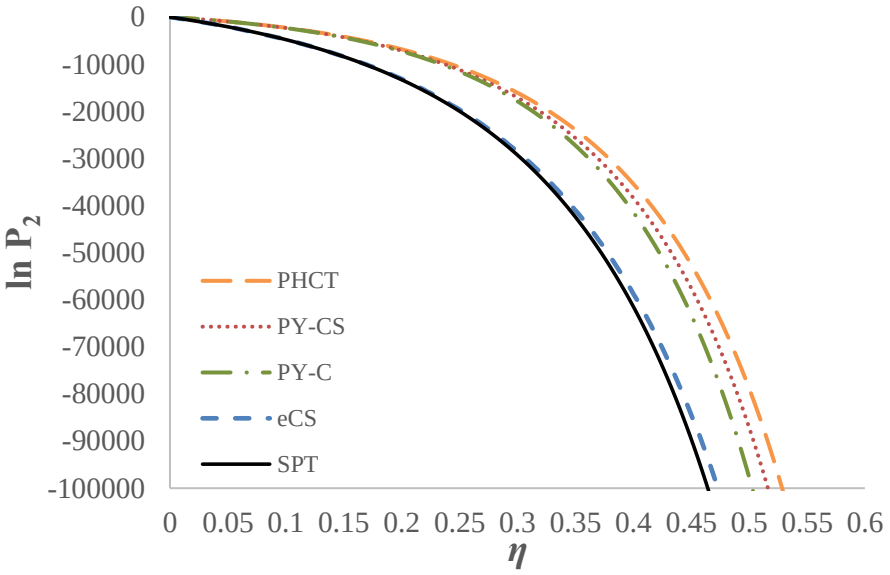

Figure 4.6: Long chain ($r = 1{,}000$) insertion probability into short chain ($r = 5$) fluid vs. occupied volume fraction

4.3.4 Polymer/Solvent Model Parameters

Considering the Chiew models predicted much greater insertion probabilities than the SPT chain model at typical LCST densities and compositions, a VDW mean-field energy contribution of Equation (2.9) was added to the Chiew models. PIB and n-hexane parameters were fit using the methods described in Appendix A for the SPT model. The Chiew model parameters in Table 4.1 have the same interpretations as the corresponding SPT parameters. For both the polymer and solvent, the characteristic temperature T^* is much lower for the Chiew models than for the SPT model, and the hexane chain length is longer, but the parameters still indicate that $v^*_{\text{polymer}} > v^*_{\text{solvent}}$, and Chiew modeled polymer/solvent mixtures likely will encounter the issues seen in Chapter 3.

Model	n-Hexane T^* (K)	P^* (MPa)	ρ^* (g/cm^3)	r	PIB T^* (K)	P^* (MPa)	ρ^* (g/cm^3)
PY-C	2204	2514	2.25	5.249	13952	810	1.47
PY-CS	2254	2322	2.17	4.931	13302	774	1.43
PHCT	2266	2136	2.08	4.706	12022	756	1.41

Table 4.1: n-Hexane and poly(isobutylene) equation of state parameters for the Chiew type models for hard sphere chains

4.3.5 Chiew Model Spinodals and Polymer/Solvent LCSTs

The equation for the single homogeneous binary phase stability (or metastability), the spinodal was determined for these models with methods described in reference [33].

PY-C Spinodal

The PY-C spinodal is given by:

$$\begin{aligned} & v^*\left(\frac{1}{r_1 v_1^* \phi_1}+\frac{1}{r_2 v_2^* \phi_2}\right)-2\eta\beta v^* \Delta P_{12}^*-\frac{\kappa\beta v^* P_\phi^2}{\eta} \\ & +3\left(\frac{1}{\sigma_{-3}}\right)\left(\frac{1}{\sigma_1}-\frac{1}{\sigma_2}\right)\left[\left(\frac{1}{\sigma_1^2}-\frac{1}{\sigma_2^2}\right)+\left(\frac{1}{r_1\sigma_1^2}-\frac{1}{r_2\sigma_2^2}\right)\right] y \quad = \quad 0 \\ & +9\left(\frac{1}{\sigma_{-3}}\right)\sigma_{-1}\left(\frac{1}{\sigma_1}-\frac{1}{\sigma_2}\right)^2 y^2 \end{aligned} \tag{4.21}$$

in which

$$P_\phi = kT\left\{\begin{array}{l} -\eta^2\beta(2\phi_1 P_1^* + (\phi_2-\phi_1)P_{12}^* - 2\phi_2 P_2^*) \\ +\left(\frac{1}{r_1 v_1^*}-\frac{1}{r_2 v_2^*}\right) y + \frac{3}{2}\left(\frac{6}{\pi}\right)\left(\frac{1}{\sigma_1}-\frac{1}{\sigma_2}\right)\left(\frac{\phi_1}{r_1\sigma_1^2}+\frac{\phi_2}{r_2\sigma_2^2}\right) y^2 \\ +\frac{3}{2}\left(\frac{6}{\pi}\right)\sigma_{-1}\left(\frac{1}{r_1\sigma_1^2}-\frac{1}{r_2\sigma_2^2}\right) y^2 + 9\left(\frac{6}{\pi}\right)\sigma_{-1}^2\left(\frac{1}{\sigma_1}-\frac{1}{\sigma_2}\right) y^3 \\ +\frac{3}{2}\left(\frac{6}{\pi}\right)\sigma_{-1}\left(\frac{1}{\sigma_1^2}-\frac{1}{\sigma_2^2}\right) y^2 + \frac{3}{2}\left(\frac{6}{\pi}\right)\sigma_{-2}\left(\frac{1}{\sigma_1}-\frac{1}{\sigma_2}\right) y^2 \end{array}\right\} \tag{4.22}$$

and

$$\kappa = \left\{ \frac{kT}{\eta} \left[\begin{array}{l} \frac{y^2}{rv^*} + 3\sigma_{-1}\left(\frac{\phi_1\sigma_1}{r_1v_1^*} + \frac{\phi_2\sigma_2}{r_2v_2^*}\right)y^3 \\ +\frac{6}{\pi}(3\sigma_{-1}\sigma_{-2})y^3 + \frac{6}{\pi}(9\sigma_{-1}^3)y^4 \end{array} \right] - 2\eta^2 P^* \right\}^{-1} \quad (4.23)$$

PY-CS Spinodal

The PY-CS spinodal is given by

$$\begin{array}{l} v^*\left(\frac{1}{r_1v_1^*\phi_1} + \frac{1}{r_2v_2^*\phi_2}\right) - 2\eta\beta v^*\Delta P_{12}^* - \frac{\kappa\beta v^* P_\phi^2}{\eta} \\ +3\left(\frac{1}{\sigma_{-3}}\right)\left(\frac{1}{\sigma_1} - \frac{1}{\sigma_2}\right)\left[\left(\frac{1}{\sigma_1^2} - \frac{1}{\sigma_2^2}\right) + 2\sigma_{-1}\left(\frac{1}{\sigma_1} - \frac{1}{\sigma_2}\right) + \left(\frac{1}{r_1\sigma_1^2} - \frac{1}{r_2\sigma_2^2}\right)\right]y \\ +6\left(\frac{1}{\sigma_{-3}}\right)\sigma_{-1}\left(\frac{1}{\sigma_1} - \frac{1}{\sigma_2}\right)^2 y^2 - 6\left(\frac{1}{\sigma_{-3}}\right)\sigma_{-1}\left(\frac{1}{\sigma_1} - \frac{1}{\sigma_2}\right)^2 \ln(1+y) \end{array} = 0 \quad (4.24)$$

in which

$$P_\phi = kT\left\{ \begin{array}{l} -\eta^2\beta(2\phi_1P_1^* + (\phi_2 - \phi_1)P_{12}^* - 2\phi_2P_2^*) + \left(\frac{1}{r_1v_1^*} - \frac{1}{r_2v_2^*}\right)y \\ +\left(\frac{6}{\pi}\right)\left[\begin{array}{l} -3\left(\frac{1}{\sigma_1} - \frac{1}{\sigma_2}\right)\sigma_{-1}^2 y + \frac{3}{2}\left(\frac{1}{\sigma_1} - \frac{1}{\sigma_2}\right)\sigma_{-2}y^2 \\ +\frac{3}{2}\sigma_{-1}\left(\frac{1}{\sigma_1^2} - \frac{1}{\sigma_2^2}\right)y^2 + 3\left(\frac{1}{\sigma_1} - \frac{1}{\sigma_2}\right)\sigma_{-1}^2 y^2 \\ +6\left(\frac{1}{\sigma_1} - \frac{1}{\sigma_2}\right)\sigma_{-1}^2 y^3 + 3\left(\frac{1}{\sigma_1} - \frac{1}{\sigma_2}\right)\sigma_{-1}^2\eta \\ +\frac{3}{2}\left(\frac{1}{\sigma_1} - \frac{1}{\sigma_2}\right)\left(\frac{\phi_1}{r_1\sigma_1^2} + \frac{\phi_2}{r_2\sigma_2^2}\right)y^2 + \frac{3}{2}\sigma_{-1}\left(\frac{1}{r_1\sigma_1^2} - \frac{1}{r_2\sigma_2^2}\right)y^2 \end{array} \right] \end{array} \right\} \quad (4.25)$$

and

$$\kappa = \left\{ \frac{kT}{\eta} \left[\begin{array}{l} \frac{y^2}{rv^*} - \left(\frac{\pi}{6}\right)\sigma_{-1}^3 y^2 + 3\left(\frac{6}{\pi}\right)\sigma_{-1}\sigma_{-2}y^3 + 2\left(\frac{6}{\pi}\right)\sigma_{-1}^3 y^3 \\ +6\left(\frac{6}{\pi}\right)\sigma_{-1}^3 y^4 + \left(\frac{6}{\pi}\right)\sigma_{-1}^3\eta^2 + 3\sigma_{-1}\left(\frac{\phi_1\sigma_1}{r_1v_1} + \frac{\phi_2\sigma_2}{r_2v_2}\right)y^3 \end{array} \right] - 2\eta^2 P^* \right\}^{-1} \quad (4.26)$$

PHCT Spinodal

The PY-C spinodal is given by:

$$
\begin{aligned}
& v^*\left(\frac{1}{r_1 v_1^* \phi_1}+\frac{1}{r_2 v_2^* \phi_2}\right)-2\eta\beta v^* \Delta P_{12}^*-\frac{\kappa\beta v^* P_\phi^2}{\eta} \\
& +3\left(\frac{1}{\sigma_{-3}}\right)\left(\frac{1}{\sigma_1}-\frac{1}{\sigma_2}\right)\left[\left(\frac{1}{\sigma_1^2}-\frac{1}{\sigma_2^2}\right)+2\sigma_{-1}\left(\frac{1}{\sigma_1}-\frac{1}{\sigma_2}\right)+\left(\frac{1}{r_1\sigma_1^2}-\frac{1}{r_2\sigma_2^2}\right)\right] y \\
& +\left[\begin{array}{l}\frac{9}{2}\left(\frac{1}{\sigma_{-3}}\right)\sigma_{-1}\left(\frac{1}{\sigma_1}-\frac{1}{\sigma_2}\right)^2+\frac{1}{2}\left(\frac{1}{r}\right)\left(\frac{1}{\sigma_1}-\frac{1}{\sigma_2}\right)^2\left(x_1\sigma_1^2+x_2\sigma_2^2\right) \\ +\left(\frac{1}{\sigma_{-3}}\right)\sigma_{-1}\left(\frac{1}{\sigma_1}-\frac{1}{\sigma_2}\right)\left(\frac{1}{r_1\sigma_1}-\frac{1}{r_2\sigma_2}\right)\end{array}\right] y^2 \\
& -6\left(\frac{1}{\sigma_{-3}}\right)\sigma_{-1}\left(\frac{1}{\sigma_1}-\frac{1}{\sigma_2}\right)^2 \ln(1+y)
\end{aligned}
= 0 \quad (4.27)
$$

in which

$$
P_\phi = kT\left\{\begin{array}{l}
-\eta^2\beta(2\phi_1 P_1^*+(\phi_2-\phi_1)P_{12}^*-2\phi_2 P_2^*)+\left(\frac{1}{r_1 v_1^*}-\frac{1}{r_2 v_2^*}\right) y \\
-3\left(\frac{6}{\pi}\right)\left(\frac{1}{\sigma_1}-\frac{1}{\sigma_2}\right)\sigma_{-1}^2 y+\frac{3}{2}\left(\frac{6}{\pi}\right)\sigma_{-1}\left(\frac{1}{r_1\sigma_1^2}-\frac{1}{r_2\sigma_2^2}\right) y^2 \\
+\frac{3}{2}\left(\frac{1}{r v^*}\right)\left(\frac{1}{\sigma_1}-\frac{1}{\sigma_2}\right)(x_1\sigma_1+x_2\sigma_2) y^2 \\
+\left(\frac{1}{r v^*}\right)\sigma_{-1}\left(\frac{1}{\sigma_1}-\frac{1}{\sigma_2}\right)(x_1\sigma_1^2+x_2\sigma_2^2) y^3 \\
+\frac{1}{2}\left(\frac{6}{\pi}\right)\sigma_{-1}^2\left(\frac{1}{r_1\sigma_1}-\frac{1}{r_2\sigma_2}\right) y^3+\frac{3}{2}\left(\frac{6}{\pi}\right)\left(\frac{1}{\sigma_1}-\frac{1}{\sigma_2}\right)\sigma_{-2} y^2 \\
+\frac{3}{2}\left(\frac{6}{\pi}\right)\sigma_{-1}\left(\frac{1}{\sigma_1^2}-\frac{1}{\sigma_2^2}\right) y^2+3\left(\frac{6}{\pi}\right)\left(\frac{1}{\sigma_1}-\frac{1}{\sigma_2}\right)\sigma_{-1}^2 y^2 \\
+\frac{9}{2}\left(\frac{6}{\pi}\right)\left(\frac{1}{\sigma_1}-\frac{1}{\sigma_2}\right)\sigma_{-1}^2 y^3+3\left(\frac{6}{\pi}\right)\left(\frac{1}{\sigma_1}-\frac{1}{\sigma_2}\right)\sigma_{-1}^2\eta
\end{array}\right\} \quad (4.28)
$$

and

$$
\kappa = \left\{\frac{kT}{\eta}\left[\begin{array}{l}\frac{y^2}{r v^*}-\left(\frac{6}{\pi}\right)\sigma_{-1}^3 y^2+3\sigma_{-1}\left(\frac{\phi_1\sigma_1}{r_1 v_1}+\frac{\phi_2\sigma_2}{r_2 v_2}\right) y^3 \\ +3\left(\frac{6}{\pi}\right)\sigma_{-1}\sigma_{-2} y^3+2\left(\frac{6}{\pi}\right)\sigma_{-1}^3 y^3+\frac{9}{2}\left(\frac{6}{\pi}\right)\sigma_{-1}^3 y^4 \\ +\left(\frac{6}{\pi}\right)\sigma_{-1}^3\eta^2+\frac{3}{2}\left(\frac{1}{r v^*}\right)\sigma_{-1}^2(x_1\sigma_1^2+x_2\sigma_2^2) y^4\end{array}\right]-2\eta^2 P^*\right\}^{-1} \quad (4.29)
$$

Spinodal Calculations

Figure 4.7 shows the calculated spinodals for the PIB/n-hexane mixture for the three Chiew type models with $\zeta_{12} = 1$. The SPT spinodal for $\zeta_{12} = 1$ was also included for comparison. As in Section 3.8, the molecular weight of the PIB used in calculations was 1.5×10^6. The Chiew models performed better than the SPT chain model, in that they all predicted a temperature range of single homogeneous phase stability for $\zeta_{12} = 1$, but the Chiew predicted LCSTs for $\zeta_{12} = 1$ occurred far below the experimental 128°C[47]. Making polymer/solvent interactions more favorable by increasing ζ_{12} did improve the calculated LCSTs, but the Chiew models reached a maximum LCST far below the experimental value and below that of the SPT model upon adjustment of ζ_{12}. The maximum LCST and associated ζ_{12} for each model is listed in Table 4.2. Each $\Delta P_{12}^{*} < 0$ at the ζ_{12} values in Table 4.2.

model	max LCST (°C)	ζ_{12}
SPT	89.26	1.219
PY-C	83.37	1.209
PY-CS	83.05	1.205
PHCT	58.73	1.188

Table 4.2: Maximum LCST predicted with adjusted ζ_{12} for each model for the PIB/n-hexane solution

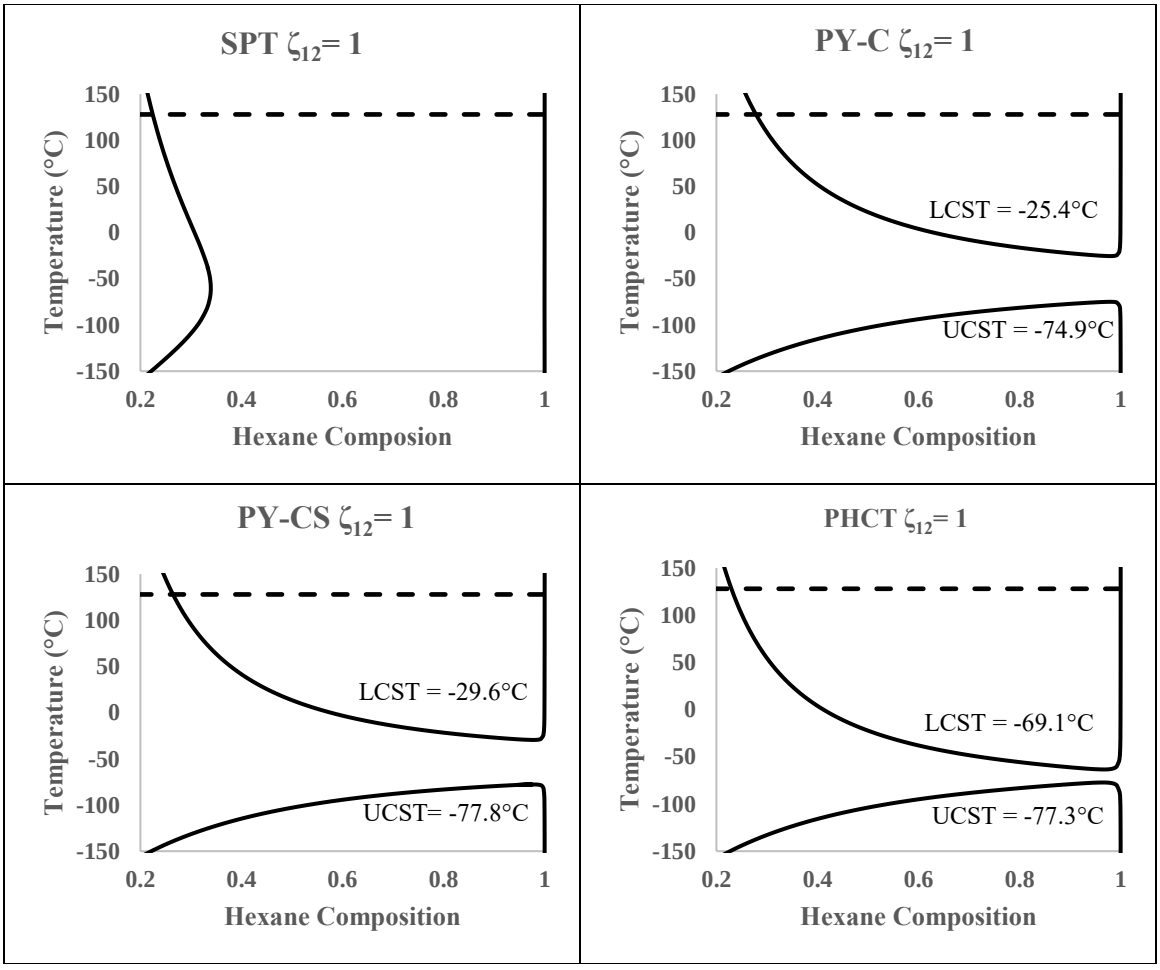

Figure 4.7: Calculated spinodal curves for the PIB/n-hexane system at atmospheric pressure. CSTs are indicated when applicable. Solid curves are spinodals calculated with the indicated model and $\zeta_{12} = 1$. Dashed horizontal lines indicate the experimental value of 128°C.

4.3.6 Other Considered Model

A Chapman type statistical associating fluid theory (SAFT) perturbation model for mixtures of homonuclear chains using a BMCSL HS reference fluid was developed[61,65], and a mean field potential energy was added. The resulting equation of state is given by:

$$Z = 1 + r\left[\left(1 + 3\frac{\sigma_{-1}\sigma_{-2}}{\sigma_{-3}}\right)y + 3\left(\frac{\sigma_{-1}\sigma_{-2}}{\sigma_{-3}} + \frac{\sigma_{-1}^3}{\sigma_{-3}}\right)y^2 + 2\frac{\sigma_{-1}^3}{\sigma_{-3}}y^3\right] - \sum_i \left\{x_i(r_i - 1)\left[\frac{y + \frac{3}{2}\sigma_{-1}\sigma_i y + 3\sigma_{-1}\sigma_i y^2 + \sigma_{-1}^2\sigma_i^2 y^2 + \frac{3}{2}\sigma_{-1}^2\sigma_i^2 y^3}{1 + \frac{3}{2}\sigma_{-1}y\sigma_i + \frac{1}{2}\sigma_{-1}^2 y^2\sigma_i^2}\right]\right\} \quad (4.30)$$

By nature of the model, chemical potentials and the spinodal for binary mixtures may be analytically derived, but equation (4.30) and other thermodynamic properties are more complicated than their Chiew model counterparts and offer little improvements in accuracy. Ultimately this SAFT model did not meet the ease of implementation goal stated in Chapter 2.

4.4 CONCLUSIONS

The SPT model was compared against other models to predict insertion probabilities of hard spheres and hard sphere chains. The eCS model better predicted the insertion probabilities of individual spheres, but Figure 4.6 showed that improving the accuracy of individual sphere insertion probability had little effect on the chain chemical potential compared to explicitly accounting for chain connectivity. When applied to the PIB/hexane solution, Chiew type models provided marginal improvements in accuracy at the cost of practicality. In Chapter 7, improvements to the mean-field van der Waals configurational energy contribution is addressed through a new thermodynamic model which more realistically limits the number of spheres a given sphere can attract and the range over which the attractive energy may extend.

Chapter 5: Linearity of Saturated Liquid Density and Configurational Energy at Low Pressure*

5.1 INTRODUCTION

Fluid Zeno lines are the loci of points in the temperature-density plane where the compressibility factor $P/\rho kT \equiv Z = 1$. This linearity is not limited to the supercritical fluids, but persists well into the subcritical regime. Batschinski first reported on this unique locus, also known as the "Boyle line"[67], which was discovered in 1906[68]. It serves as an index for the competition between attractive and repulsive forces: when $Z > 1$ repulsive forces dominate (hard fluid), and when $Z < 1$ attractive forces dominate (soft fluid)[69]. On the $Z = 1$ line these opposing forces balance and the fluid exhibits pseudo ideal gas behavior. This line intersects the temperature axis (zero density intercept) at the Boyle temperature T_B^* where the second virial coefficient vanishes. T_B^* typically is 2 to 2.5 times the critical temperature T_c. When the $Z = 1$ line reaches T_c, the density is about 2 times greater than the critical density ρ_c with a pressure roughly 8 times the critical pressure, consistent with Z_c in the range 0.25–0.31. For many fluids, the Zeno line extends well into the subcritical liquid regime, covering a span of several hundred Kelvin.

Iso-Z curves for $Z < 1$ lines diverge negatively from the Zeno line and terminate on the coexistence (COEX) curve[70]. As temperature approaches absolute zero, the extrapolated Zeno line enters the metastable liquid regime and intersects the density axis at the Boyle density ρ_B^*. Physically ρ_B^* represents the maximum hypothetical density of the disordered liquid at absolute zero. With the exception of the van der Waals equation

* This material was published as: Isaac C. Sanchez, Sean O'Keefe, and Jeffrey F. Xu, "New Zeno-Like Liquid States" *J. Phys. Chem. B* 120 (15), 3705 (2016)[66]. Sean Patrick O'Keefe contributed to the data collection plotting and regression of sections detailing the linearity of liquid density in temperature along $Z \simeq 0$.

of state (VDW EOS), no other known purely theoretical EOS captures the Zeno linearity at all temperatures, from supercritical to subcritical regimes[71].

Just as the $Z = 1$ locus defines the Zeno line, there is another locus in the temperature-density plane that defines another striking linearity in liquids. This linear locus is defined by liquid states for which $Z \to 0$, where the low temperature region of this iso-Z curve coincides with the liquid branch of the liquid-vapor coexistence curve. As discussed in Chapter 1, on the liquid-vapor coexistence curve, the saturated vapor compressibility factor $Z_{vap} \to 1$ with decreasing temperature, and the saturated liquid, compressibility factor $Z_{liq} \to 0$ as temperature decreases. Due to the decreasing vapor pressure ($P_{\text{sat}} \to 0$) the saturated vapor behaves like an ideal gas, while for saturated liquids, $Z_{liq} = P_{\text{sat}}/kT\rho_{liq} \to 0/kT\rho_{liq} = 0$. For example, many liquids at their normal boiling point have a compressibility factor $Z_{liq} = \exp[-5.5 \pm 0.2] \sim 0.024$ and. This liquid compressibility factor further decreases as the triple point is approached. Thus, in the normal liquid range (NLR as defined in Chapter 1), $Z_{liq} \simeq 0$ for saturated liquids.

Saturated liquid densities in the NLR are linear in temperature and form a strong corresponding states principle (CSP). The so-called "Law of Rectilinear Diameters" may be interpreted as an early observation of this relationship for liquids[72]. Often written as:

$$\frac{1}{2}\left(\rho_{liq} + \rho_{vap}\right) = \rho_c + a(T_c - T) \tag{5.1}$$

in which a is a positive constant, the rectilinear diameter statement equates the average of the saturated vapor density and saturated liquid density to a linear function of the difference between temperature and T_c. In its earliest applications, (5.1) estimated the critical density[73]; however, its accuracy decreases as the critical point is

approached[74]. (5.1) is most accurate along the portion of the coexistence curve when $Z \simeq 0$, and $\rho_l \gg \rho_v$. In this limit (5.1) can be written as:

$$\rho_{liq} = 2(\rho_c + a)T_c - 2aT \tag{5.2}$$

which corresponds with the observed linearity of liquid density in temperature as $Z \simeq 0$.

When the $Z \simeq 0$ line is extrapolated to absolute zero, its value is near the Boyle density ρ_B^*, the $T = 0$ intercept of the Zeno line. This $Z \simeq 0$ linearity is a common characteristic of liquids with negligible or very low vapor pressures. Liquids that express this linearity include monoatomic and diatomic elements, other low boiling organics, hydrogen bonding ammonia and methanol, molten metals and salts[75,76], metal alloys[77–81], and polymer melts[82]. Helium and water are the only known exceptions, both of which exhibit slight, but noticeable curvature along the $Z \simeq 0$ curve as the triple point is approached.

Plots of the configurational energy of the saturated liquid also vary linearly with density or temperature in the NLR. Extension of this line to zero temperature defines the ground state configurational energy of the hypothetical disordered liquid. This linear dependence on density implies that the usual VDW approximation for the configurational energy is valid in the NLR for a wide variety of liquids that include some hydrogen bonding liquids such as ammonia.

5.2 ZENO-LIKE STATES AS $Z \simeq 0$

5.2.1 Insights from the van der Waals equation

The VDW EOS can be expressed in reduced variables as:

$$\frac{P}{\rho kT} \equiv Z = \frac{3}{3-\rho_R} - \frac{9\rho_R}{8T_R} \tag{5.3}$$

in which $\rho_R \equiv \rho/\rho_c$, and $T_R \equiv T/T_c$. Equating Z to unity yields the Zeno line ($Z = 1$):

$$\frac{T_B}{27/8} + \frac{\rho_B}{3} \equiv \frac{T_B}{T_B^*} + \frac{\rho_B}{\rho_B^*} = 1 \tag{5.4}$$

where the Boyle temperature $T_B^*/T_c = 27/8$, and the Boyle density $\rho_B^*/\rho_c = 3$. When these Boyle parameters are used to reduce temperature and pressure the VDW EOS adopts a simple form:

$$Z = \frac{1}{1-(\rho/\rho_B^*)} - \frac{(\rho/\rho_B^*)}{(T/T_B^*)} \tag{5.5}$$

In the NLR where $Z \simeq 0$, setting equation (5.3) to zero results in a parabolic equation and a corresponding states principle (CSP):

$$T_R = \frac{9}{8}\rho_R\left(1 - \frac{\rho_R}{3}\right) \tag{5.6}$$

Equation (5.6) suggests saturated liquids for which $Z \simeq 0$ should obey a CSP when temperature and density are reduced by their respective critical values. This idea is tested in Figure 5.1 for 11 liquids. As can be seen, the CSP holds to some degree, but not as well as equation (5.6) suggests. Though the CSP predicted by the EOS is not observed, each plot is strikingly linear, a quality not predicted by the VDW equation. Figure 5.1 also shows that ρ_R for some liquids exceeds 3, the maximum reduced density allowed by the classical VDW model, further suggesting the inadequacy of the VDW EOS in

modeling saturated liquids. Data used for Figures 5.1, and 5.2 were obtained from the NIST webbook of thermophysical properties of fluid systems http://webbook.nist.gov/chemistry/fluid/ [3].

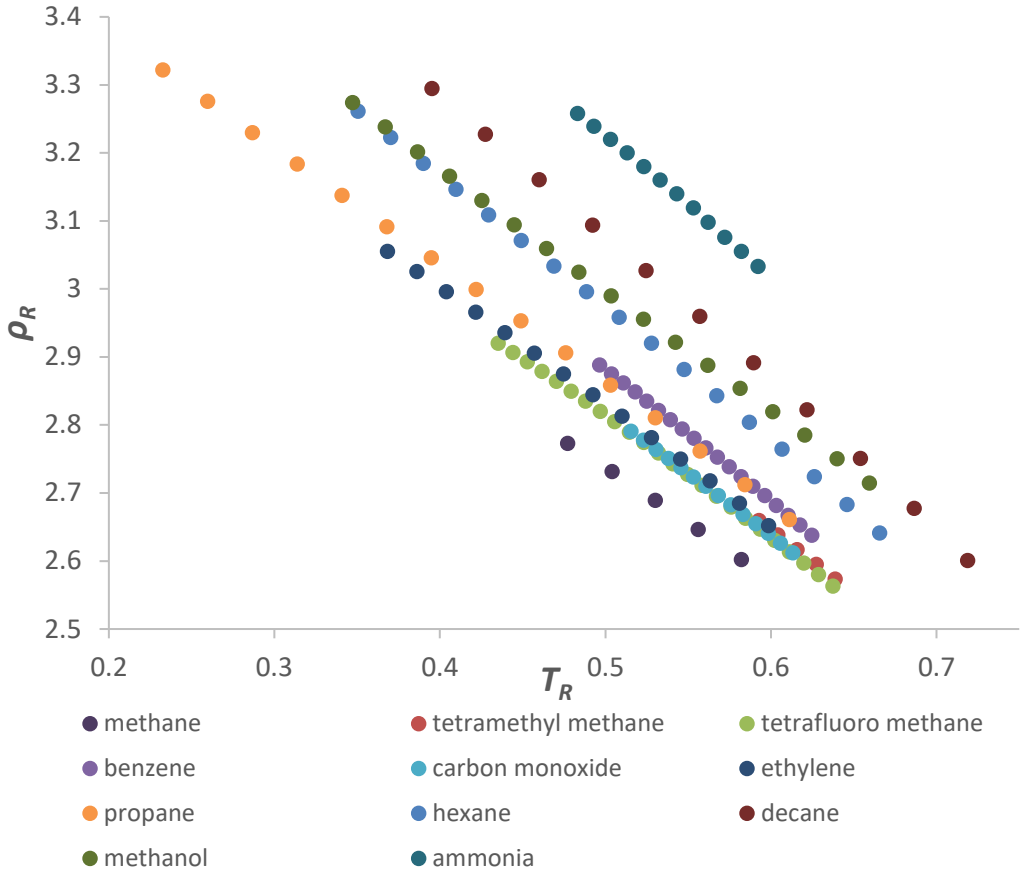

Figure 5.1: Reduced temperature-reduced density plot of saturated liquids in the NLR

If equation (5.3) is set to zero, a different CSP is predicted:

$$T/T_B^* = (\rho/\rho_B^*)[1 - (\rho/\rho_B^*)] \tag{5.7}$$

Rescaling the temperature and pressure with the Boyle parameters yields a much better CSP (not shown), but the apparent linearity of the data is not captured. Table 5.1 contains density (ρ^*) and temperature (T^*) intercepts of the $Z \simeq 0$ saturated density/temperature lines in Figure 5.1 reduced by ρ_c and T_c respectively. Table 5.1 also contains reduced Zeno line intercepts with ρ_B^* and T_B^* values taken from reference [69] while all other data were obtained from the NIST webbook[3]. Reducing the density and temperature by the $Z \simeq 0$ intercepts and replotting yields Figure 5.2. Typical deviations from the line defined by the reducing ρ and T by the saturated liquid intercepts are of the order of 0.5% in the NLR and within experimental uncertainties.

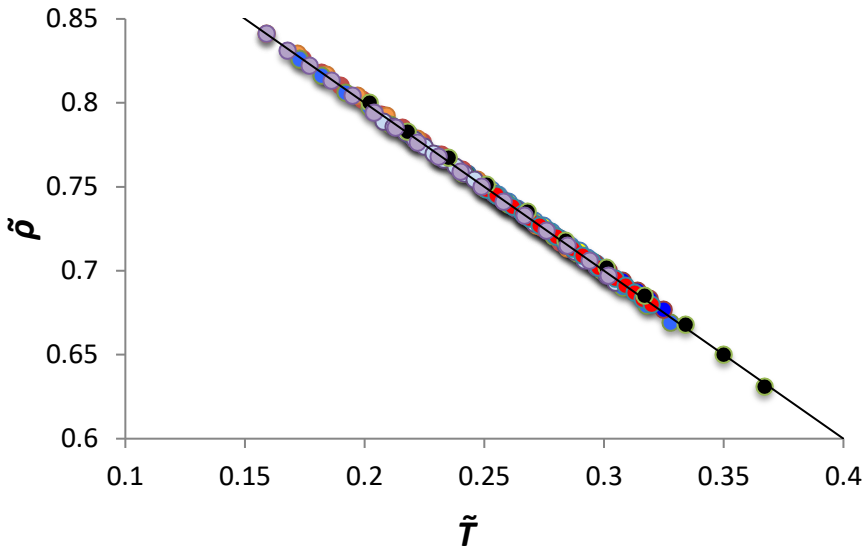

Figure 5.2: Dimensionless density vs. temperature plots of the data shown in Figure 5.1

liquids	$\frac{T_B^*}{T_c}$	$\frac{\rho_B^*}{\rho_c}$	$\frac{\rho^*}{\rho_c}$	$\frac{T^*}{T_c}$	$\frac{U^*}{RT^*}$	$\frac{T^*}{U^*}\frac{dU}{dT}$	Trouton's constant
Group I							
argon*	2.71	3.52	3.60	2.08	3.4	1.26	8.9
krypton*	2.72	3.45	3.66	2.09	3.4	1.25	9.0
xenon*	2.74	3.47	3.66	2.10	3.4	1.27	9.2
methane*	2.67	3.50	3.55	2.18	3.2	1.23	8.9
oxygen*	2.64	3.51	3.58	2.19	3.3	1.25	9.1
nitrogen*	2.57	3.63	3.64	2.10	3.6	1.29	8.7
CO	2.56	3.62	3.73	2.04	3.9	1.30	8.8
average	2.66	3.53	3.63	2.11	3.5	1.26	8.9
Group II							
ethylene	2.54	3.65	3.70	2.19	3.8	1.38	9.6
ethane*	2.49	3.71	3.65	2.17	3.8	1.31	9.6
propane	2.46	3.74	3.73	2.14	4.3	1.36	9.8
butane*	2.39	3.78	3.80	2.11	5.2	1.37	9.9
pentane*	2.28	3.90	3.85	2.10	5.1	1.41	10.0
hexane	2.32	3.89	3.95	2.03	5.6	1.36	10.1
decane	2.21	4.04	4.12	1.96	7.4	1.41	10.6
C6H12	2.36	3.76	3.89	2.00	5.2	1.36	10.2
C6H6	2.34	3.81	3.86	1.98	5.2	1.42	10.5
C6H5CH3	2.41	3.79	3.91	2.05	5.5	1.44	10.4
C(CH3)4	2.38	3.68	3.77	2.00	5.1	1.37	9.7
H2S	2.58	3.66	3.79	2.06	4.1	1.32	10.5
CF4	2.31	3.74	3.70	2.09	4.6	1.35	9.8
CHF3	2.39	3.94	4.02	2.02	5.3	1.33	10.6
CH2F2	2.48	4.04	4.18	2.00	5.2	1.30	10.8
CH3F	2.64	3.81	4.05	1.96	4.9	1.30	10.3
C2F5H	2.26	3.91	3.96	1.99	5.9	1.36	10.5
C2F6	2.27	3.89	3.97	1.95	5.6	1.33	10.6
average	2.40	3.82	3.88	2.04	5.1	1.36	10.2
Group III							
ammonia	2.54	4.16	4.27	2.07	4.8	1.28	11.7
methanol	—	—	3.90	2.09	—	—	12.6

Table 5.1: Summary of parameters associated with Zeno-like states.

The density intercept is designated as ρ^*. This is the hypothetical maximum density attainable by the disordered liquid. The temperature intercept is designated as T^*. This temperature represents the theoretical critical temperature of a fluid in which the liquid side of the liquid-vapor coexistence curve remains linear along the entirety of the coexistence curve. Each liquid satisfies the following simple linear equation:

$$\frac{\rho}{\rho^*} + \frac{T}{T^*} = 1 \tag{5.8}$$

where ρ^* and T^* are respectively the density and temperature of a saturated liquid in the NLR. This equation also holds along low-pressure isobars where $Z \simeq 0$.

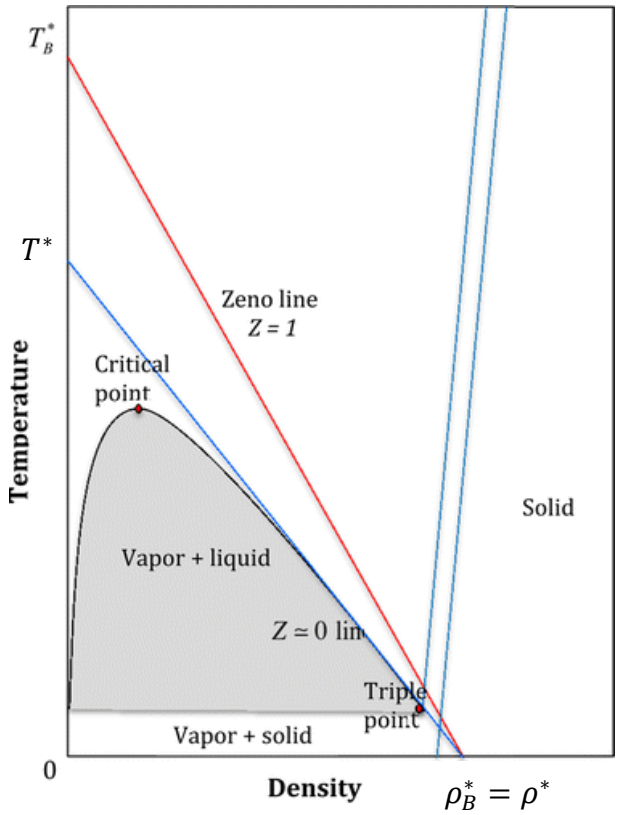

Figure 5.3: Schematic illustration of the coexistence curve, the Zeno ($Z = 1$), and the NLR saturated density ($Z \simeq 0$) lines

Figure 5.3 schematically illustrates the temperature-density phase diagram. The two iso-Z lines ($Z = 1; Z \simeq 0$) along with their temperature and density intercepts are also displayed. When both lines are extrapolated to zero temperature, they intercept the density axis at approximately the same density, $\rho^* \simeq \rho_B^*$ which is the hypothetical maximum density attainable by the disordered liquid at absolute zero. As seen in Table 5.1, this density is usually 3.5 to 4.0 times the critical density for small organics, but tends to be larger for more chainlike molecules such as dodecane and for molten metals (Table 5.3). The $Z = 1$ locus intercepts the temperature at the well-known Boyle temperature T_B^*, which is usually about 2 to 2.5 times T_c. The extension of the $Z \simeq 0$ line to zero density intercepts the temperature axis at T^*. If the $Z \simeq 0$ condition persisted to low densities, something theoretically possible for a polymer liquid, then $T_c \rightarrow T_c^*$.

Table 5.1 divides liquids into the groups determined by Trouton's constant ($\Delta S_{vap}/k$) discussed in Chapter 1. The table summarizes intercepts of both the $Z = 1$ and $Z \simeq 0$ lines for various fluids, and as can be seen, for the many $\rho^* \simeq \rho_B^*$. Although equation (5.7) does not predict a linear dependence of temperature on density, the VDW EOS does predict that as $T \rightarrow 0$, along the $Z \simeq 0$ condition, $\rho \rightarrow \rho_B^*$, the Boyle density intercept of the $Z = 1$ line. Others have come to the same conclusion that the extension of the VDW EOS to zero temperature intersects the density axis at ρ_B^*, but use a different argument[83].

Zeno line and saturated liquid data in the NLR are tabulated for n-decane In Table 5.2 and plotted in Figure 5.4. Coefficient of determination (R^2) values for both the Zeno line and the saturated liquid density line are greater than 0.999. Figure 5.4 illustrates the striking linearity of the two lines and how they approach a common intercept at absolute zero. The convergence to a common density is not perfect ($\rho_B^*/\rho_c = 4.04; \rho^*/\rho_c = 4.12$); usually ρ^* is 1 to 2% larger than ρ_B^*. The linearity of the

saturated density data in the NLR for decane extends over 200K, whereas for xenon it is only about 4K. The extent of the NLR depends on the triple point pressure. Lower triple point pressures, require a greater temperature rise to reach atmospheric pressure. For decane the triple point pressure is $O(10^{-5})$ bar, whereas for xenon it is about 0.8 bar. Data for Table 5.2 and Figure 5.4 were obtained from the NIST webbook of thermophysical properties of fluid systems http://webbook.nist.gov/chemistry/fluid/ [3].

$Z = 1$			$Z \simeq 0$			
T (K)	ρ (mol/L)	P (bar)	T (K)	ρ (mol/L)	P (bar)	Z_{sat}
675	3.35	188	447	4.25	1	6.3×10^{-3}
650	3.47	188	444	4.27	0.932	5.9×10^{-3}
625	3.60	187	424	4.39	0.539	3.5×10^{-3}
600	3.72	186	404	4.51	0.291	1.9×10^{-3}
550	3.96	182	384	4.62	0.145	9.8×10^{-4}
500	4.21	175	364	4.74	6.6×10^{-2}	5×10^{-4}
450	4.44	167	344	4.85	2.7×10^{-2}	2×10^{-4}
400	4.68	156	324	4.96	9.2×10^{-3}	7×10^{-5}
350	4.92	144	304	5.07	2.7×10^{-3}	2×10^{-5}
300	5.16	129	284	5.18	6.4×10^{-4}	5×10^{-6}
275	5.29	121	264	5.29	1.2×10^{-4}	1×10^{-6}
260	5.36	116	244	5.40	1.5×10^{-5}	6×10^{-7}

Table 5.2: Zeno line and saturated liquid data in the NLR are tabulated for n-decane

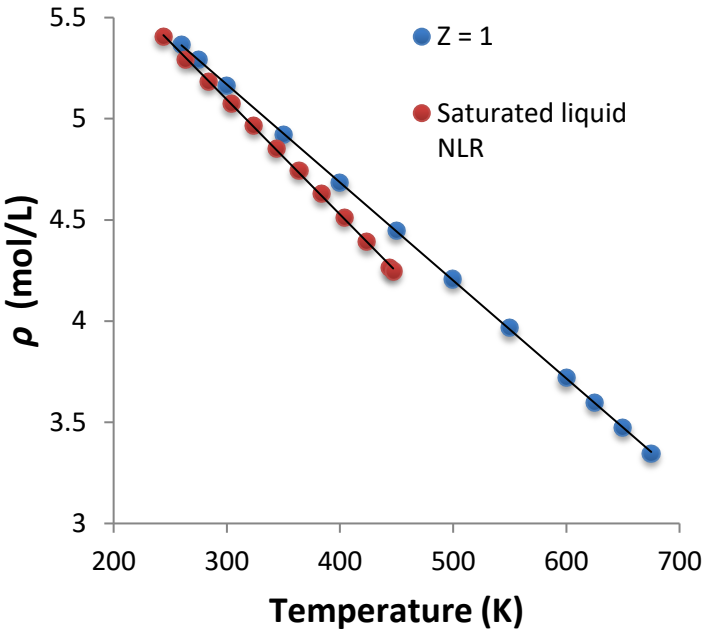

Figure 5.4: Zeno line ($Z = 1$) and saturated liquid data ($Z_{sat} \simeq 0$) for decane

5.2.2 Polymeric, inorganic, ionic, and metallic liquids

Polymer melts should have a large NLR since they have negligible vapor pressures at temperatures well above their melting temperatures. Polymer liquid densities are a linear function of temperature for both non-polar and polar polymers. ρ^* and T^* parameters have been fit and tabulated for many polymers for use in an equation of state that reduces to equation (5.8) at $Z \simeq 0$[82]. The physical interpretations of the ρ^* and T^* parameters are identical to those in Section 5.2.1. Most organic polymers tend to thermally decompose by 300 C.

Molten metals and salts have very low or negligible vapor pressures and large NLRs. The density of liquid metals and salts has been shown to vary linearly with temperature[75,76] In Table 5.3 density and temperature intercepts (ρ_g^*, T_c^*) have been

determined for some molten metals, salts, and sulfur. These intercepts have been used to construct the master plot shown in Figure 5.5. Unless an alternate reference is listed, density and critical point data were obtained from NIST Web Thermo Tables (http://wtt-pro.nist.gov/wttpro/). Critical temperatures in reference [84] are estimated values, and critical densities for these species are unavailable.

liquid	ρ^* (g/cc)	$\frac{\rho^*}{\rho_c^*}$	T^*	$\frac{T^*}{T_c}$
Lithium[85]	0.563	4.7	5590	1.74
Sodium[85]	1.015	4.9	4240	1.65
Potassium[85]	0.919	4.7	3710	1.67
Rubidium[86]	1.62	5.5	3470	1.72
Cesium[86]	2.02	5.3	3390	1.76
Aluminum[87]	2.59	4.6	11,130	1.69
Magnesium[88]	1.8	4.4	7690	3.0
Calcium[84]	1.56	—	8615	2.6
Strontium[84]	2.54	—	11,330	3.7
Barium[84]	3.7	—	10,940	3.0
Iridium[84]	21.8	—	25,600	3.3
Sulfur	2.02	3.7	3490	2.7
$SnCl_4$	2.98	4.0	1150	1.95
$TiCl_4$	2.24	3.9	1290	2.0
$SbCl_3$	3.48	3.9	1516	1.9
$AlCl_3$	2.57	5.0	946	1.5

Table 5.3: Density-temperature parameters for some molten metals and salts.

Unlike organic liquids, density linearity for inorganics can persist to well above the normal boiling point. The data in Figure 5.5 superposes to the same line as Figure 5.2, and the two sets of data could have been combined to a single figure while maintaining the strong corresponding states principle.

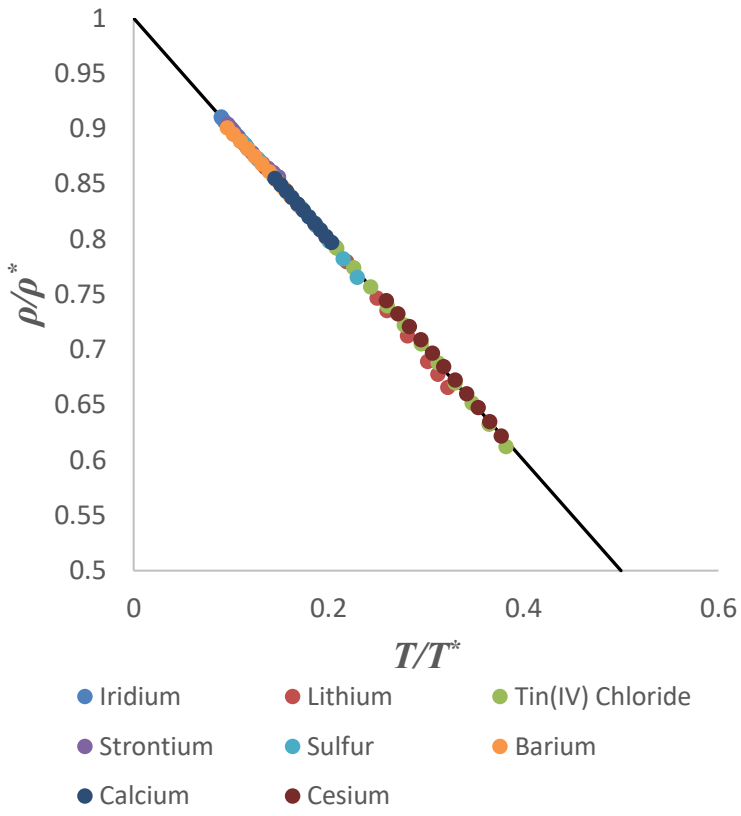

Figure 5.5: Illustrates the linear dependence of density on temperature in the NLR for some liquid metals and inorganics.

5.2.3 Linearity in the configurational energy

As discussed in Chapter 1, the internal energy of vaporization ΔE_{vap} to an excellent approximation equals the liquid configurational energy, U_{liq} in the NLR. Thermal energy contributions to the internal energy for both liquid and vapor phases are equal and cancel in forming ΔE_{vap} and the configurational energy of the dilute gas phase is to a good approximation negligible. In the NLR $\left|U_{liq}\right| = \Delta E_{vap}$. When ΔE_{vap} is plotted against temperature or density, linear plots are obtained with slope m:

$$m = -\frac{T^*}{U^*}\left(\frac{\partial U}{\partial T}\right)_{Z\simeq 0} = \frac{\rho^*}{U^*}\left(\frac{\partial U}{\partial \rho}\right) > 0$$
$$\frac{U}{U^*} = 1 - m\frac{T}{T^*} = 1 - m\left(1 - \frac{\rho}{\rho^*}\right) \tag{5.9}$$

Extension of either line to absolute zero, defines the ground state energy U^* of the disordered liquid. Some energy parameters are tabulated in Table 5.1. Potential energy intercepts for methanol were excluded from Table 5.1 because its configurational energy exhibits a slight negative curvature in the NLR. The potential energy linearity is illustrated in Figure 5.6. Energy of vaporization data were obtained from the NIST webbook[3].

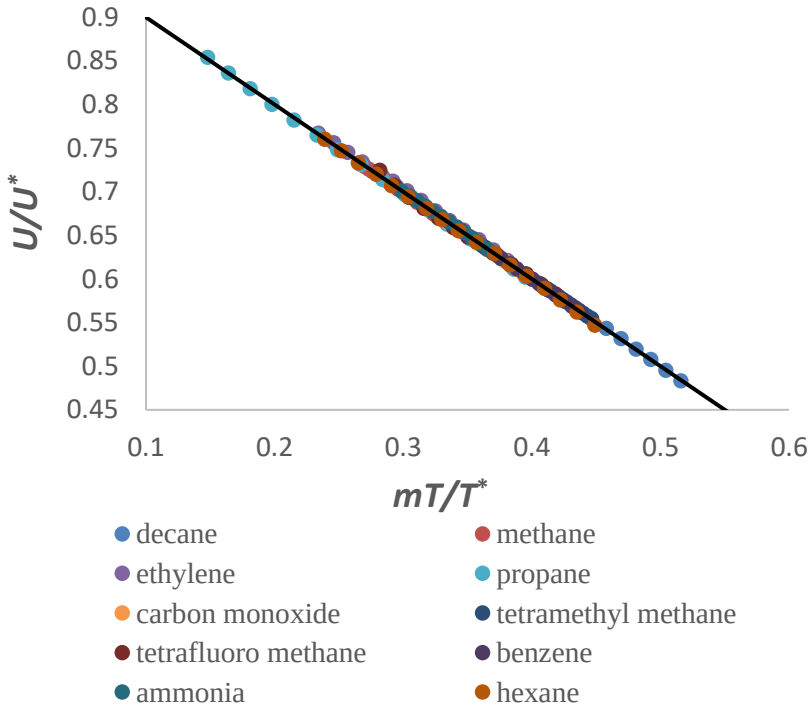

Figure 5.6: Master plot for saturated liquid configurational energy in the NLR.

The configurational energy linearity implies that the classical VDW approximation of a configurational energy that varies directly with density is valid for

liquids in the NLR. In the VDW approximation, $-U_{VDW} = 2a\rho$ where a is the usual VDW parameter that measures the attractive strength of the interaction. From equation (5.9) we see that the VDW parameter can be identified with the following:

$$a = \frac{1}{2}\left(\frac{\partial|U|}{\partial\rho}\right)_{Z\simeq 0} = \frac{m}{2}\frac{U^*}{\rho^*} \tag{5.10}$$

The VDW value for the a parameter is:

$$a = \frac{9}{8}\frac{RT_c}{\rho_c} \tag{5.11}$$

Using the tabulated values for the monoatomic and diatomic Group I liquids given in Table 5.1, the calculated VDW a parameter averages $1.28RT_c/\rho_c$ as compared with $9RT_c/8\rho_c$. The effective a parameter for Group II liquids averages higher at $1.85RT_c/\rho_c$.

5.3 DISCUSSION

Liquids in their NLR ($P_{\text{sat}} \leq 1$ bar) exhibit a linear density behavior with temperature. Figures 5.2 and 5.5 show these data superpose to form a single master curve. Deviations from linearity are typically less than 0.5%, often within the experimental accuracy of the data itself. This linearity, which has been noted for specific liquids, appears to be a broadly applicable property of liquids in general. This ubiquitous linearity implies that the liquid branch of the liquid-vapor coexistence curve is linear in temperature in the NLR and represents a very strong corresponding states principle: *Saturated liquid densities are a linear function of temperature in the NLR for molecular, polymeric, inorganic, ionic, and metallic liquids and when reduced by the intercepts of this line superpose to form a single master curve.* Helium and water currently remain the only outstanding exceptions to this CSP.

As Figure 5.3 schematically illustrates, if this linear behavior where to persist to low density ($\rho \to 0$), the critical temperature would approach the theoretical temperature intercept T^*. The only liquid that might exhibit this density/temperature linearity from the melting point to the critical point is a polymeric liquid of high molecular weight. According to the LF model[17], setting $Z \simeq 0$ gives:

$$\tilde{T} = -\frac{\tilde{\rho}^2}{\ln(1-\tilde{\rho}) + (1-1/r)\tilde{\rho}} \tag{5.12}$$

as $r - \infty$, and $\tilde{\rho} \to 0, \tilde{T} \to 2$ along $Z \simeq 0$. The dimensionless LF critical temperature is given by:

$$\tilde{T}_c = \frac{2r}{\left(1+\sqrt{r}\right)^2} \tag{5.13}$$

as $r \to \infty, \tilde{T}_c \to 2$. While the LF model does not predict a linear density/temperature dependence as $Z \simeq 0$, it does predict that as chain length $r \to \infty$, and $\tilde{\rho} \to 0$ along $Z \simeq 0$, the dimensionless temperature $\tilde{T} \to \tilde{T}_c$ and $T^*/T_c \to 1$ (for T^* defined as the temperature intercept of the $Z \simeq 0$ curve). LF and other chain models predict that as $r \to \infty, \rho_c \to 0$; therefore $\rho^*/\rho_c \to \infty$ for infinite chain lengths. This general trend can already be discerned in Table 5.1 among the normal alkanes from ethane to dodecane. For very long chains, the saturated vapor pressure remains negligibly small at temperatures near the critical point so that the requirement that $Z \simeq 0$ is satisfied over nearly the entire liquid branch of the coexistence curve. Most organic polymers begin to thermally degrade before reaching 300°C. Since $T^* > 1{,}000\ K$ for high molecular weight polymers, and a liquid-vapor critical point has never been observed for these fluids, the suggested equality of the regressed T^* and the hypothetical polymer liquid/vapor critical temperature cannot be confirmed.

In Table 5.3 the five alkali metals from Li to Cs, along with Al have very similar values of $\rho_g^*/\rho_c \sim 5$, which are larger than any organic in Table 5.1, and all have similar values of $T_c^*/T_c \sim 1.7$, which are smaller than any organic. Based on the heuristic arguments above, both ratios suggest that alkali metals should exhibit a larger NLR than organics. The low Z values and persistence of the density/temperature linearity beyond the normal boiling point for inorganics support this suggestion. For sodium, the linearity persists to temperatures at least 450 K above its normal boiling point of 1156 K and likely continues higher temperatures. Overall, the measured linear behavior for Na stretches over 1200 K. For cesium, linearity persists to at least 350 K above its boiling point of 944 K and over 1000 K overall. Based on the behaviors of Na and Cs, similar extended linear density ranges are expected for some of the other alkali metals above their normal boiling points.

While linearity for inorganics can persist several degrees above the normal boiling point, negative deviations of the order of 1% from linear behavior for xenon begin about 50 degrees above its normal boiling point or at $Z_{liq} \simeq 0.02$. Sodium remains linear to 450 degrees above its boiling point where $Z_{liq} \simeq 0.04$, and deviations remain $< 0.5\%$. All density/temperature parameters (ρ^*, T^*) tabulated in Tables 5.1 and 5.3 were determined entirely with data in the NLR where Z_{liq} is usually less than 0.005. If a larger temperature range were to be employed in fitting the data, somewhat different parameters would be obtained and the apparent range of linearity could be extended at the expense of overall accuracy. Because of this decrease in accuracy, and inconsistencies of this decrease from fluid to fluid, a general rule for linearity extent beyond the normal boiling point remains undefined.

For chain molecules, the molar energy of vaporization increases with chain length because the chain molecule attractively interacts with many monomers that belong to

other chains. Although these monomer-monomer interactions are often weak VDW types, there are many interactions per chain and the number of interactions increases linearly with chain length. A consequence of the increase of ΔE_{vap} with chain length is that the equilibrium vapor pressure drops with increasing chain length effectively increasing the NLR. In molten metals, the attractive forces between atoms are much stronger than the VDW forces among organic molecules. Tighter bonding manifests as higher T_c and normal boiling temperatures, as well as much smaller thermal expansion coefficients. The decrease in thermal expansion coefficients corresponds to a larger temperature increase required to go from the triple point to the normal boiling point, which by definition is the NLR. While the ΔE_{vap} differences explain why certain liquids have greater NLRs than others, it does not explain why the density/temperature linearity might persist well beyond the NLR.

Intercepts for the $Z = 1$ locus, are the Boyle temperature T_B^*, where the second virial coefficient vanishes, and the Boyle density is given by[89]:

$$\rho_B^* = \frac{T_B^* \left.\frac{dB_2}{dT}\right|_{T=T_B^*}}{B_3(T_B^*)} \tag{5.14}$$

where B_2 and B_3 are the 2nd and 3rd virial coefficients of the density virial expansion. In normal practice, neither the Boyle temperature nor density is determined from virial coefficients. Instead, $P\rho T$ data are used to establish the $Z = 1$ locus, and if the locus appears linear, it is extended to zero density to determine T_B^* and to zero temperature to obtain the Boyle density. This method used to determine the T_B^* and ρ_B^* values reported in Table 5.1. Similarly, saturated $P\rho T$ data used to determine the $Z \simeq 0$ locus in the NLR were extended to zero temperature to determine ρ^*. According to the VDW model, $\rho^* = \rho_B^*$, but ρ^* values in Table 5.1 tend to be about 1 to 2% greater than the ρ_B^*.

Diverse liquids in terms of interatomic interactions and structure exhibit simple and similar density and configurational energy behavior in their NLRs. The condition $Z = 0$ corresponds to the situation in which attractive forces have become completely dominant, to the extent that molecules in the liquid state can no longer escape to the vapor state. Even at the normal boiling point only about 1 out of 250 molecules is able to escape from liquid to vapor states[1]. The repulsive forces appear to serve as an excluded volume background force that prevents the liquid from collapsing due to the strength of the attractive forces. For many organics, this attractive interaction increases in strength linearly with density, or equivalently through the density/temperature linearity, increases linearly with decreasing temperature. Simultaneous satisfaction of both linear requirements, $Z = 1$, $Z \simeq 0$, linearity with a VDW type interaction energy at high densities are imposing constraints on any model based EOS.

5.4 CONCLUSIONS

Saturated liquid densities are a linear function of temperature in the NLR for molecular, polymeric, inorganic, ionic, and metallic liquids and superpose to form a single master curve. Although others might exist, water and helium are the only known exceptions to this very strong corresponding states principle. Many organics that include some hydrogen bonding liquids such as ammonia, possess a configurational energy in the NLR that varies linearly with density in agreement with the well-known VDW approximation for the interaction energy. Within this dissertation, this chapter demonstrates that these very simple linear property relationships are nearly universal to all liquids at low pressure. In Chapter 6, this linear density/temperature relationship is further applied to all liquids (with the exceptions of water and helium) at NLR temperatures and elevated pressures.

Chapter 6: Universal Linearity of Liquid Density with Temperature

6.1 INTRODUCTION

Although atomic interactions in molten metals differ from the strong coulombic interactions in molten salts and both differ significantly from weak van der Waals interactions present in organic liquids, nearly all liquids appear to display simple, universal empirical property relationships[90]. Chapter 5 discussed the simple linear density/temperature relationship of saturated liquids (with the exceptions of water and helium) at very low pressures and temperatures in the NLR. When reduced by the intercepts of this line, the liquid densities follow a relationship of the form: $(\rho/\rho^*) + (T/T^*) = 1$, and satisfy a strong corresponding states principle[66]. For volatile liquids, this linearity had been observed through the so-called "law of rectilinear diameters" in the limit $\rho_{liq} \gg \rho_{vap}$ [72,73]. In 1968 Bondi noted that $\partial\rho/\partial T$ for liquids was constant over a large temperature range[91]. This relationship has separately been applied to molten metals and salts[75,76], alloys[77–81], and polymer melts[82] at low pressures ($P \leq 1$ bar). In this chapter, the linear relationship is extended to homogeneous mixtures and density/temperature isobars for liquids at elevated pressure.

6.2 LINEARITY OF LIQUID DENSITY/TEMPERATURE ISOBARS AT LOW PRESSURE

Often a linear density/temperature relationship is directly applied as an isobaric, linear Taylor expansion about an average temperature T_0 as is done for simplified buoyancy-driven flow calculations[92–94]:

$$\rho = \rho_0[1 - \alpha_0(T - T_0)] \tag{6.1}$$

ρ_0 is the density at T_0, and $\alpha_0 = -(\partial\rho/\partial T)_p/\rho_0\big|_{T=T_0}$ is the isobaric coefficient of thermal expansion at T_0. The isobaric density expansion in temperature (6.1) is valid over

temperature ranges in which the second and higher order terms in the isobaric Taylor expansion are much less than the linear term over the temperature range. Applying this condition to the second order term gives:

$$\left|\frac{\left(\frac{\partial^2\rho}{\partial T^2}\right)_P\Big|_{T=T_0}}{2\left(\frac{\partial\rho}{\partial T}\right)_P\Big|_{T=T_0}}(T-T_0)\right| = \left|\frac{\alpha_0^2 - \left(\frac{\partial\alpha}{\partial T}\right)_P\Big|_{T=T_0}}{2\alpha_0}(T-T_0)\right| \ll 1 \qquad (6.2)$$

as the condition for near linearity of a density/temperature isobar.

When $|T-T_0|$ is large, condition (6.2) is satisfied when $(\partial^2\rho/\partial T^2)_P|_{T=T_0}$ or equivalently $\left|\alpha_0^2 - (\partial\alpha/\partial T)_P|_{T=T_0}\right|$ is low. For most liquids, $(\partial\alpha/\partial T)_P|_{T_0} > 0$ and $(\partial\alpha/\partial T)_P|_{T_0} \sim \alpha_0^2$ at temperatures far below T_c. With this combination of conditions, (6.2) may be satisfied at large values of $|T-T_0|$. As an example, toluene at 1 bar and $T_0 = 280.5$ (the midpoint of the NLR) is considered. Using data generated from the NIST REFPROP model[95] through the NIST/TRC Web Thermo Tables (WTT) http://wtt-pro.nist.gov/wtt-pro/, the maximum value on the left side of (6.2) at NLR temperatures and 1 bar is 0.0134. Since $0.0134 \ll 1$, the density of liquid toluene at 1 bar, may be considered a linear function of temperature over the NLR temperature range 178–383 K. In Chapter 5, liquid water and helium were the only exceptions noted for this low pressure linearity given by (5.8)[66]. For both helium and water, $(\partial\alpha/\partial T)_P \gg \alpha^2$ at temperatures near the triple point, and condition (6.2) is not met.

If the isobaric expansion were carried out in volume instead of density, the conditions for the validity of a linear expansion in volume analogous to (6.2) is given by:

$$\left|\frac{\left(\frac{\partial^2 V}{\partial T^2}\right)_P\Big|_{T=T_0}}{2\left(\frac{\partial V}{\partial T}\right)_P\Big|_{T=T_0}}(T-T_0)\right| = \left|\frac{\alpha_0^2+\left(\frac{\partial \alpha}{\partial T}\right)_P\Big|_{T=T_0}}{2\alpha_0}(T-T_0)\right| \ll 1 \qquad (6.3)$$

The only difference between criteria (6.3) and (6.2) is the sign modifying $(\partial\alpha/\,\partial\mathrm{T})_P|_{T=T_0}$. Since $(\partial\alpha/\,\partial\mathrm{T})_P$ is positive for most liquids below their critical temperatures, volume/temperature isobars express a greater degree of deviation from linearity than density/temperature isobars. The maximum value of (6.3) for toluene at 1 bar and $T_0 = 280.5$ K is 0.121. While this calculation indicates a linear volume expansion in temperature for toluene may still reasonably apply over short temperature differences, the analogous density expansions is more accurate in that range and better describes the liquid over the NLR.

To show the near linearity of density/temperature isobars, Table 6.1 lists maximum values of the left side of condition (6.2) for liquids at 1 bar, with T_0 set as the midpoint of the temperature range considered. Table 6.1 also list the maximum fractional change in density relative to ρ_0 along the temperature range given by $|\alpha_0(T-T_0|$. Since T_0 is chosen as the midpoint, and the absolute value is taken, maximum values of both quantities occur at either of the endpoints of the temperature range. For small molecule liquids, all values were obtained or derived from the NIST wtt-pro thermos tables[95], and the NLR temperature range as defined earlier in this dissertation was used. Temperature ranges for polymer fluids are those given by Rodgers.[49] who carefully ensured that those temperatures described the polymer melt. α_0 and $(\partial\alpha/\partial T)_P|_{T_0}$ for polymers were calculated from a Tait model with Temperature dependences of Tait parameters for all polymers taken from Rodgers[49] or from Olabisi and Simha.[96].

Liquid	$\lvert\alpha_0(T-T_0)\rvert_{\mathrm{Max}}$	$\left\lvert\frac{\left(\frac{\partial^2\rho}{\partial T^2}\right)_P\Big\rvert_{T=T_0}}{2\left(\frac{\partial\rho}{\partial T}\right)_P\Big\rvert_{T=T_0}}(T-T_0)\right\rvert$
Argon	0.0076	0.0044
Krypton	0.0060	0.0042
Xenon	0.0041	0.0029
Methane	0.0333	0.0238
Oxygen	0.0673	0.0267
Nitrogen	0.0365	0.0273
Carbon Monoxide	0.0345	0.0221
Ethane	0.0886	0.0314
Propane	0.1126	0.0286
n-Butane	0.0980	0.0331
n-Pentane	0.1079	0.0239
n-Hexane	0.1054	0.0241
n-Decane	0.1166	0.0340
n-Dodecane	0.1246	0.0499
Neopentane	0.0215	0.0167
Ethene	0.0705	0.0291
Cyclohexane	0.0472	0.0188
Benzene	0.0471	0.0163
Toluene	0.1084	0.0134
Hydrogen Sulfide	0.0222	0.0109
Trifluoromethane	0.0810	0.0304
Perfluoroethane	0.0289	0.0235
Poly(Styrene)	0.0411	0.0103
Poly(epichlorohydrin)	0.0466	0.0117
Poly(caprolactone)	0.0304	0.0076
Poly(Methyl Methacrylate)	0.0254	0.0226
Poly(Isobutylene)	0.0322	0.0081
Poly(Tetrafluoroethylene)	0.0613	0.0307
Poly(Vinyl acetate)	0.0467	0.0080
Poly(Ethylene) (linear)	0.0453	0.0113

Table 6.1: Near linearity condition and fractional density increases relative to a midpoint density for liquids at 1 bar

6.3 DENSITY/TEMPERATURE LINEARITY IN MOLECULAR AND POLYMERIC LIQUIDS

This linearity can be expressed in the following compact form:

$$\frac{\rho}{\rho_P^*} + \frac{T}{T_P^*} = 1 \tag{6.4}$$

in which the subscripts "P" indicate isobaric data were regressed. As in Chapter 5, ρ_P^* and T_P^* are the density ($T = 0$) and temperature ($\rho = 0$) intercepts of the line, respectively. If the density data lie along a high-pressure isobar, both ρ_P^* and T_P^* will obtain unique values for the isobar different from those at low pressure. ρ_P^* retains its interpretation as the maximum density the fluid may attain along the isobar. Appendix B gives low pressure ρ_P^* and T_P^* values obtained through linear least squares regression of either isobaric or saturated density/temperature data.

6.3.1 Pure Liquids at Low Pressure

For small molecule liquids, densities were regressed at NLR temperatures. Isobaric data at 1 bar were used when available, otherwise saturated densities were regressed. Density data were obtained with models[95,97,98] through the NIST/TRC Web Thermo Tables (WTT) http://wtt-pro.nist.gov/wtt-pro/. Only polymers with tabulated PVT data (unbiased) were regressed[49,96,99–104] with temperature ranges matching those given by Rodgers[49]. Density/temperature lines for molten metals and salts are available elsewhere[75,76]. Coefficient of determination (R^2) values were greater than 0.99 for all 144 liquids. Over the temperature ranges regressed, the linear equation (6.4) correlates the densities and temperature to within the uncertainties of the source data.

Often the nonlinear Rackett equation[105] is employed to estimate liquid densities in the NLR for engineering applications. The Rackett equation requires three parameters,

T_c,ρ_c, and Z_c (or P_c). It returns liquid densities to within 1 or 2% accuracy for a given temperature. While the Rackett equation may apply over a larger temperature range than (6.4), a linear density/temperature correlation only requires two parameters and yields densities within experimental uncertainties (1 part in a 1000 or less) in the NLR.

6.3.2 Density/Temperature Linearity at High Pressures

In Figures 6.1 & 6.2 density/temperature data are plotted along high pressure isobars for pure toluene and poly(vinyl acetate) (PVAc) respectively. Temperature ranges are identical to those used for the low-pressure fits. For toluene in Figure 6.1, data points were generated using the NIST REFPROP model through http://wtt-pro.nist.gov/wtt-pro/[95]. For the PVAc in Figure 6.2, the viscosity-average molecular weight was given as $M_v = 189{,}000$, and PVT data were given by McKinney and Goldstein[100]. Maximum pressure was determined by the source data. Lowest R^2 values for the least squares linear regressions in Figure 6.1 and Figure 6.2 are 0.9966 for toluene and 0.9997 for PVAc, both calculated at the maximum pressures regressed for the liquids, where uncertainties in density measurements are greatest[95,100]. As can be seen in the figures, the slopes, $-\rho_P^*/T_P^*$, and intercepts, ρ^* vary with pressure.

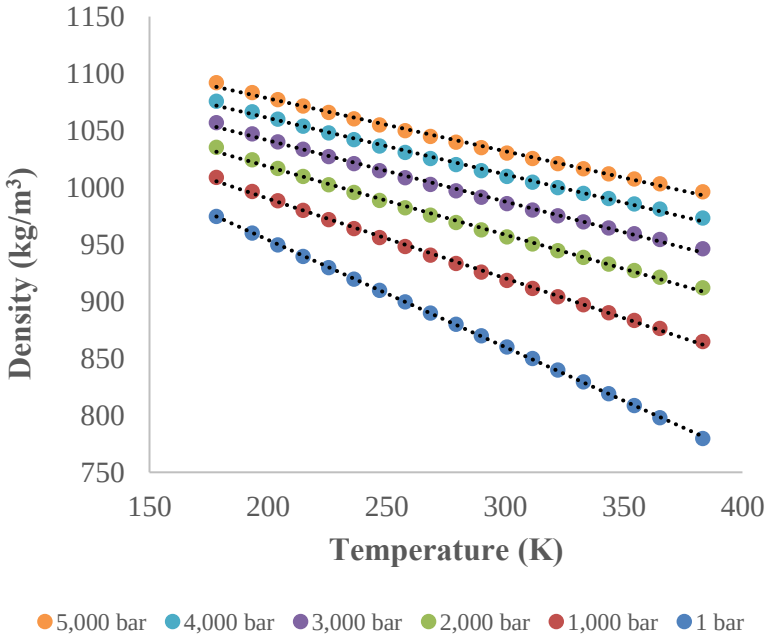

Figure 6.1: ρ vs. T plots and linear fits for toluene at different pressures.

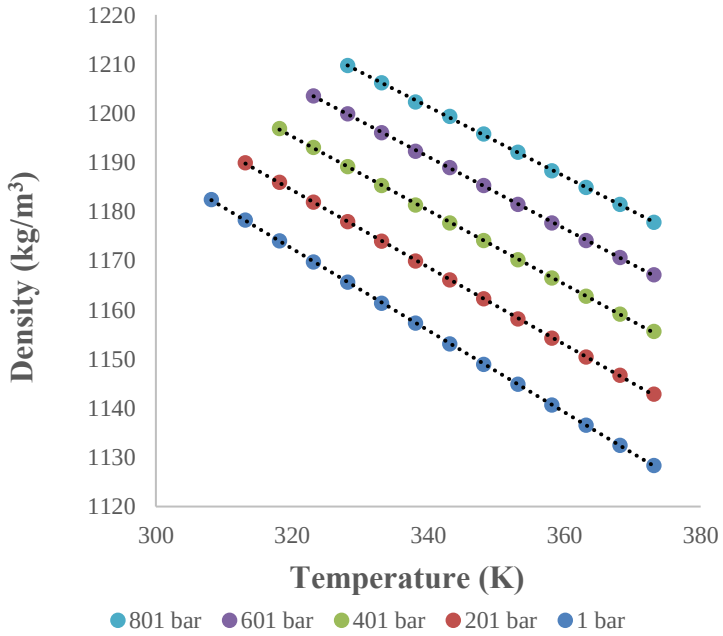

Figure 6.2: ρ vs. T plots and linear fits for Poly(vinyl acetate) at different pressures.

6.2.3 Density/Temperature Linearity of Liquid Mixtures

The PVT behavior of liquid mixtures is similar to that of pure liquids[106–108]. Ramos-Estrada, Iglesias-Silva, and Hall[109] measured densities for binary n-pentane, n-hexane, n-heptane mixtures over a temperature range 273–363 K at atmospheric pressure. Figure 6.3 plots their density/temperature measurements for four compositions of binary n-hexane/n-heptane mixtures. Density/temperature regressions on data by Ramos-Estrada et al. for each mixture and each composition displayed the same linear behavior as pure liquids. Lowest R^2 value was 0.99952 for the n-hexane/n-heptane mixture at 40.07 mole% n-hexane.

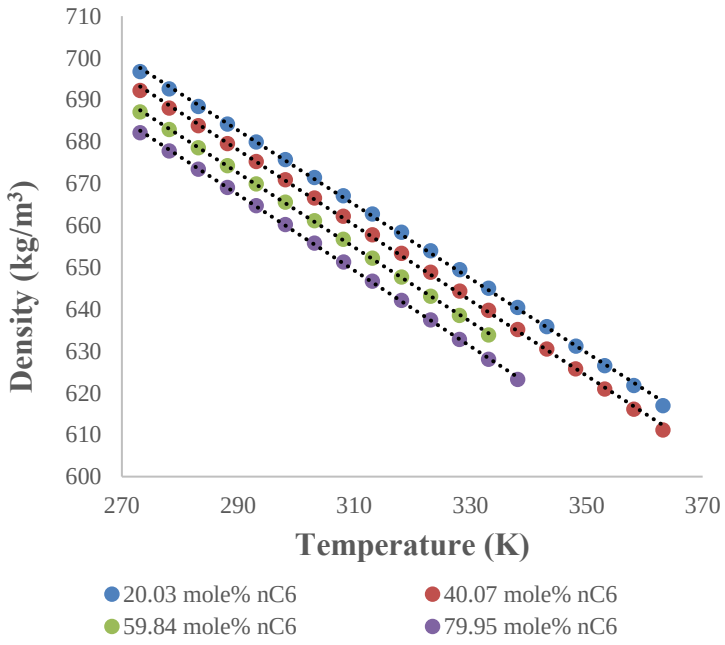

Figure 6.3: ρ vs. T plots and linear fits for binary mixtures of n-hexane and n-heptane for different compositions at atmospheric pressure

When available, PVT measurements for liquid mixtures at elevated pressure suggest that the linear density/temperature relationship is valid. Malhotra and Woolf

measured isothermal volumetric response to pressure at four different temperatures for mixtures of benzene and isooctane[110]. In order to obtain the isobaric regressions and plots for Figure 6.4, the isothermal Secant Bulk Modulus (SBM) equation was used to calculate densities at a given pressure. Malhotra and Woolf fit the SBM coefficients to their measurements[110]. Of the regressed lines in Figure 6.4 the lowest R^2 is 0.9991 at 1,200 bar; however, the linearity is less impressive than the lines in Figures 6.1–6.3 considering only four points were used for the regression.

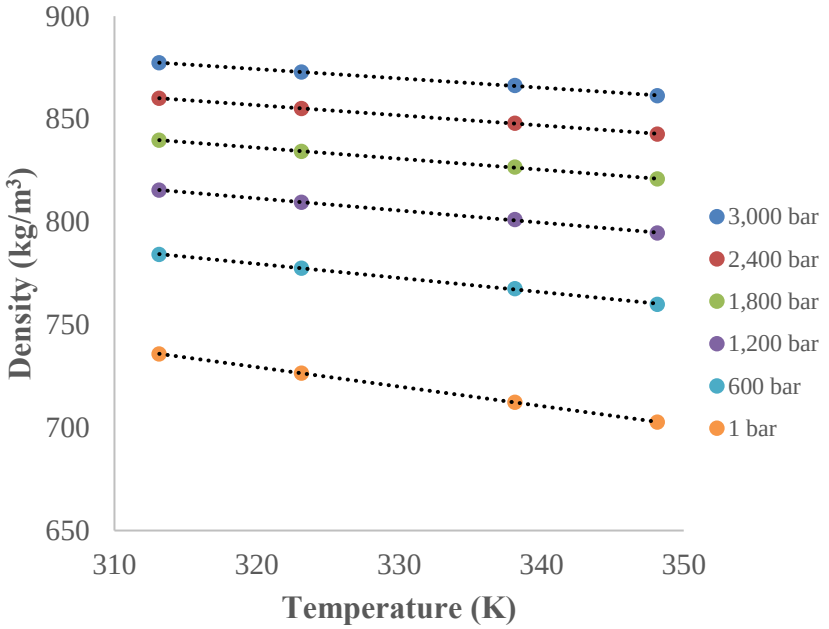

Figure 6.4: ρ vs. T plots and linear fits for liquid binary mixtures of 49.78 mole% benzene/50.22 mole% isooctane at different pressures.

As with pure liquids, the linear density/temperature relationship is observed only at temperatures far below T_c. Figure 6.5 plots the saturated liquid densities of mixtures of n-hexane and benzene from 25°C to 200°C taken by Beg, Tukur, Al-Harbi, and

Hamad[111]. Figure 6.5 also contains lines fit to the densities at NLR temperatures. The linearity becomes less accurate at temperatures above the NLR. Figure 6.5 also shows that plots become less linear as the composition of n-hexane, the species with the lower T_c, increases.

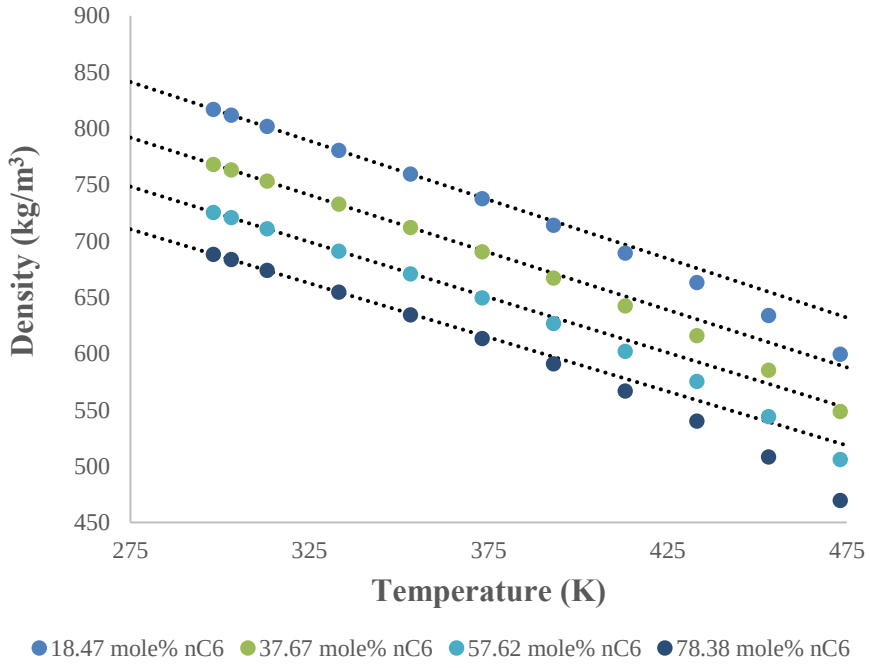

Figure 6.5: ρ vs. T plots for binary liquid mixtures of n-hexane and benzene at saturation pressure. Lines are fit using NLR temperatures only.

Frequently, the volume of a homogeneous mixture is approximated as the ideal additive sum of each component's volume:

$$V_{\text{Ideal}} = \sum x_i V_i \tag{6.5}$$

in which x_i is the mole fraction of species i, V_i is the intensive molar volume of i, and V_{Ideal} is the ideal intensive molar volume of the mixture. For very different liquid

mixtures, the excess volume $V^E = V - V_{Ideal}$ satisfies $|V^E/V_{Ideal}| < 3\%$, and setting $V = V_{Ideal}$ introduces minimal error[77,112–114]. While (6.5) may be used to accurately estimate volumes of liquid mixtures, solving the density/temperature relationship (6.4) for pure component volumes and substituting into (6.5) will not yield a linear density/temperature relationship for the mixture. In order to explicitly preserve a linear density/temperature relationship without additional adjustable parameters, mixing rules for T_P^* and ρ_P^* must be employed.

Several mixing rules have been developed for use in liquid PVT correlations[115]. Many of these are based on a corresponding states analysis and use T_c and the critical volume V_c as characteristic temperature and volume parameters respectively. For many liquids, $T_{P=0}^* \approx 2T_c$[66,73]; therefore a mixing rule which weighs mixture critical temperatures by a composition variable should be appropriate in calculating T_P^* from $T_{i,P}^*$, the pure component temperature intercept of i. Mixing rules involving critical and characteristic volume have successfully been applied to correlations interchangeably[115].

Some characteristic volume mixing rules used in liquid correlations only apply to intensive molar volumes. Characteristic molar volume for the mixture V^* is related to the characteristic mass density ρ^* by:

$$V^* = \left(\rho^* \sum \frac{w_i}{M_i}\right)^{-1} \tag{6.6}$$

in which w_i and M_i are weight fraction and molecular weight of i.

The simplest mixing rule for V^* is that of characteristic volume additivity which averages characteristic molar volume contributions weighted by x_i:

$$V_P^* = \sum x_i V_{i,p}^* \tag{6.7a}$$

or equivalently:

$$\rho_P^* = \sum \phi_i^* \rho_{i,P}^* \tag{6.7b}$$

ϕ_i^* is the occupied volume fraction of i, and is related to w_i by:

$$\phi_i^* = \frac{w_i/\rho_{i,P}^*}{\sum w_i/\rho_{i,P}^*} \tag{6.8}$$

The V_P^* mixing rule for Hankinson and Thomson's correlation is[116]:

$$V_P^* = \frac{1}{4}\left[\sum x_i V_{i,P}^* + 3\left(\sum x_i \left(V_{i,P}^*\right)^{2/3}\right)\left(\sum x_i \left(V_{i,P}^*\right)^{1/3}\right)\right] \tag{6.9}$$

A quadratic mixing rule was also considered:

$$V_P^* = \sum_i \sum_j x_i x_j V_{ij,P}^* \tag{6.10}$$

where $V_{ii,P}^* = V_{i,P}^*$. To avoid requiring additional parameters, $V_{ij,P}^*$was accounted for by:

$$V_{ij,P}^* = \frac{\zeta_{ij}}{8}\left[\left(V_{i,P}^*\right)^{1/3} + \left(V_{i,P}^*\right)^{1/3}\right]^3 \tag{6.11}$$

in which ζ_{ij} scales $V_{ij,P}^*$ with respect to a volume determined by an average characteristic length. Setting $\zeta_{ij} = 1$, and substituting the resulting $V_{ij,P}$ into (6.10) recovers mixing rule (6.9). For $\zeta_{ij} \neq 1$, a mixing rule originally intended for use in scaling a cross characteristic temperature T_{ij}^* for mixtures of alkanes[117],will be used. It is given by:

$$\zeta_{ij} = \frac{8\left(V_{i,P}^{*} V_{j,P}^{*}\right)^{1/2}}{\left[\left(V_{i,P}^{*}\right)^{1/3} + \left(V_{i,P}^{*}\right)^{1/3}\right]^{3}} \tag{6.12}$$

Equation (6.12) ultimately sets V_{ij}^{*} to the geometric mean of V_{i}^{*}, and V_{j}^{*}.

Values of V_{P}^{*} were calculated with the mixing rules described and compared with V_{P}^{*} fit to equations (6.4) and (6.6) for the mixtures in Figure 6.4. This mixture was chosen because of the large difference in pure component $\rho_{P=1\text{ bar}}^{*}$. Figure 6.6 shows these comparisons at 1 bar. At 1 bar, characteristic volume additivity (6.7) best fit regressed V_{P}^{*} with an average absolute percent error (AAPE) of 0.615%. At 150 MPa the Hankinson and Thomson mixing rule (6.9) was best with an AAPE of 0.551%, though characteristic volume additivity only had an AAPE of 0.721% at 150 MPa. Due to its superiority at lower pressures, its simple functional form, and its similar predictive ability to other mixing rules at elevated pressures, characteristic volume additivity (6.7) was selected as the mixing rule for V_{P}^{*} and ρ_{P}^{*}.

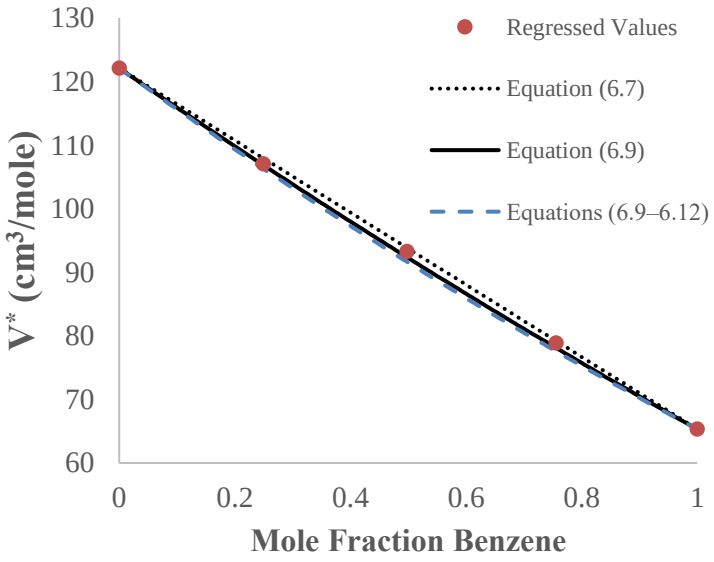

Figure 6.6: Characteristic volume comparison for benzene/isooctane mixtures at 1 bar

The simplest mixing rule for T^* is of a Kay pseudocritical type[118] for which characteristic temperatures are weighted by x_i:

$$T_p^* = \sum x_i T_{i,P}^* \tag{6.13}$$

A similar mixing rule uses a ϕ_i^* weighted average[119]:

$$T_P^* = \sum \phi_i^* T_{i,P}^* \tag{6.14}$$

Quadratic mixing rules include that for the Hankinson and Thomson correlation[116]:

$$T_P^* = \frac{\sum_i \sum_j x_i x_j T_{ij,P}^* V_{ij,P}^*}{V^*} \tag{6.15}$$

in which $T_{ii,P}^* = T_{i,P}^*, V_{ii,P}^* = V_{i,P}^*$ and the cross terms are given by:

$$T_{ij,P}^* V_{ij,P}^* = \left(T_{i,P}^* T_{j,P}^* V_{i,P}^* V_{j,P}^*\right)^{1/2} \tag{6.16}$$

Though equation (6.9) was used in Hankinson and Thomson's original correlation, V^* is here calculated with equation (6.7a).

Other quadratic mixing rules include:

$$T_P^* = \sum_i \sum_j x_i x_j T_{ij,P}^* \tag{6.17}$$

and:

$$T_P^* = \sum_i \sum_j \phi_i^* \phi_j^* T_{ij,P}^* \tag{6.18}$$

$T^*_{ii,P} = T^*_{i,P}$. T^*_{ij} may be calculated as either a scaling of the arithmetic mean:

$$T^*_{ij,P} = \frac{\zeta_{ij}}{2}\left(T^*_{i,P} + T^*_{j,P}\right) \tag{6.19}$$

or a scaling of the geometric mean:

$$T^*_{ij,P} = \zeta_{ij}\left(T^*_{i,P}T^*_{j,P}\right)^{1/2} \tag{6.20}$$

of $T^*_{i,P}$ and $T^*_{j,P}$. To avoid introduction of additional parameters, ζ_{ij} may either be set to unity or determined by equation (6.12). Equation (6.13) is recovered when the arithmetic mean is used for $T^*_{ij,P}$ in equation (6.17), and (6.14) is recovered when the arithmetic mean is used for T^*_{ij} in equation (6.18).

Guided by the success of (6.7) in calculating ρ^*_P, two other mixing rules for T^*_P were considered. The first calculates the density of the mixture as the average of the pure component densities weighted by ϕ^*_i. The corresponding T^*_P mixing rule is:

$$T^*_P = \left(\frac{1}{\rho^*_P}\sum \frac{\phi^*_i \rho^*_{i,P}}{T^*_{i,P}}\right)^{-1} \tag{6.21}$$

The second additional mixing rule corresponds to a linear volume expansion in temperature and gives an average $\left(T^*_{i,P}\right)^{-1}$ weighed by ϕ^*_i:

$$T^*_P = \left(\sum \frac{\phi^*_i}{T^*_{i,P}}\right)^{-1} \tag{6.22}$$

Though both (6.21) and (6.22) are inspired by mixture volume additivity, and calculations using these rules agree well with those assuming volume additive, equations (6.21) and (6.22) predict a negative excess volume ($V^E = V - V_{\text{Ideal}}$) when used with (6.7), corresponding to small contraction on mixing ($\Delta V_m < 0$).

To determine a suitable mixing rule for T_P^*, calculated densities were compared with measurements of binary mixture densities at 25°C and atmospheric pressure[112,113]. Table 6.2 compares the error in measured densities of 582 binary mixtures and densities calculated using equations (6.4), (6.7), and each T_P^* mixing rule. Pure component parameters from Appendix B were used. Table 6.2 also contains average absolute percent error (AAPE) for densities calculated from an ideal mixture volume assumption ($V^E = 0$) for comparison. All T_P^* mixing rules included in Table 6.2 are $< 1\%$, indicating that for liquid mixtures of small molecules, any mixing rule that reasonably averages component $T_{i,P}^*$ is satisfactory in density calculations. The largest AAPE is 0.5504% for the Hankinson and Thomson T_P^* rule.

Equations used for ρ calculation	AAPE (%)	Equations used for ρ calculation	AAPE (%)
$V^E = 0$	0.2535	(6.17), (6.20), (6.12)	0.4817
(6.13)	0.3373	(6.18), (6.19), (6.12)	0.2385
(6.14)	0.3325	(6.18), (6.20), $\zeta_{ij} = 1$	0.3097
(6.15), (6.16)	0.5504	(6.18), (6.20), (6.12)	0.2269
(6.17), (6.19), (6.12)	0.4550	(6.21)	0.2388
(6.17), (6.20), $\zeta_{ij} = 1$	0.3596	(6.22)	0.2604

Table 6.2: Errors of T_P^* mixing rules in calculating densities of mixtures of small organics at atmospheric pressure

While these mixing rules worked well for mixtures of small organics, several are inadequate when differences between component $V^*_{i,P}$ are large, such as in polymer/solvent systems. The characteristic mass densities for both small compounds and polymers in Appendix B are $O(10^3)$ kg/m^3; therefore, since $M_{polymer} \gg M_{solvent}$, the mole intensive characteristic volumes $V^*_{polymer,P} \gg V^*_{solvent,P}$. The T^*_P mixing rules based on x_i calculate T^*_P close to $T^*_{solvent,P}$. Equation (6.12) calculates ζ_{ij} near unity for mixtures of similarly sized molecules, but when $V^*_{i,P} \gg V^*_{j,P}$, equation (6.12) calculates much lower ζ_{ij}; for example, if $V^*_i/V^*_j = 1{,}000$ (a reasonable order of magnitude comparison for a polymer(i)/solvent(j) system), $\zeta_{ij} = 0.19$ by equation (6.12).

The same T^*_P mixing rules examined in Table 6.2 were used to calculate densities of poly(isobutylene) (PIB) and short n-alkanes for comparison with data by Flory, Ellenson, and Eichinger[114]. As with the mixtures of small organics, Table 6.3 contains AAPE for densities calculated using equations (6.4) and (6.7) with each T^*_P. Table 6.3 also includes the AAPE of densities calculated with a $V^E = 0$ assumption. The PIB had a viscosity average molecular weight of 40,000. Pure component parameters are given in Appendix B.

Equations used for ρ calculation	AAPE (%)	Equations used for ρ calculation	AAPE (%)
$V^E = 0$	0.5121	(6.17), (6.20), (6.12)	8.2646
(6.13)	7.9919	(6.18), (6.19), (6.12)	8.7016
(6.14)	2.2870	(6.18), (6.20), $\zeta_{ij} = 1$	1.7801
(6.15), (6.16)	35.9082	(6.18), (6.20), (6.12)	9.0388
(6.17), (6.19), (6.12)	8.2593	(6.21)	0.5500
(6.17), (6.20), $\zeta_{ij} = 1$	8.0092	(6.22)	0.1142

Table 6.3: Errors of T^*_P mixing rules in calculating densities of PIB/alkane solutions at atmospheric pressure

Most of the T^* mixing rules are inadequate at predicting the densities of the polymer/solvent mixtures. Seven mixing rules in Table 6.3 yield AAPE > 5%, with the Hankinson and Thomson T_P^* again providing the worst agreement. This is likely because these mixing rules were developed for a specific, nonlinear liquid density correlation, which does not employ characteristic volume additivity. The only mixing rule in Table 6.3 which better calculates densities than an additive volume assumption is equation (6.22), but (6.21) is satisfactory, and (6.21) is slightly better for mixtures of small organics. If (6.21) were selected as the appropriate T_P^* mixing rule, and both $\rho_{i,P}^*$ and $T_{i,P}^*$ are known for each component species, the density/temperature line for the mixture is given by:

$$\rho = \sum \phi_i^* \rho_i = \sum \left[\phi_i \rho_{i,P}^* \left(1 - \frac{T}{T_{i,P}^*} \right) \right] = \rho_P^* \left(1 - \frac{T}{T_P^*} \right) \tag{6.23}$$

Equation (6.23) is less accurate for molten metal alloys than it is for mixtures of organics. Linear density/temperature relationships have been fit for pure molten metals[75,76] and for some molten alloys at low external pressure[77–81]. The individually fit intercepts do not agree with those calculated from (6.7), (6.22), or other mixing rules, and species specific empirical composition dependences are often given instead[79,81]. Equation (6.23) should only be used for molten alloys as an approximation for the isobaric density/temperature relationship when direct measurements are unavailable.

6.4 Discussion of Density/Temperature Linearity in Liquids

As with any other expansion or regression, the parameters for a given species (T_P^* and ρ_P^*) depend on the fitting method and data points used. Figure 6.7 compares T_P^* of liquid toluene regressed over two different temperature ranges. At a pressure of 1 bar, the

T_P^* differ by 35.0 K while the difference rises to 335 K at 5,000 bar. Even though the difference in T_p^* at 5,000 bar is of the same order of magnitude as the temperature intercept itself, using the T_P^* and ρ_P^* regressed for 322.2–383.2 K to calculate density at 178.2 K produces an error of only 1.22%. The individual intercepts may differ, but properly paired intercepts may be used to extrapolate densities to lower NLR temperatures with reasonable accuracy.

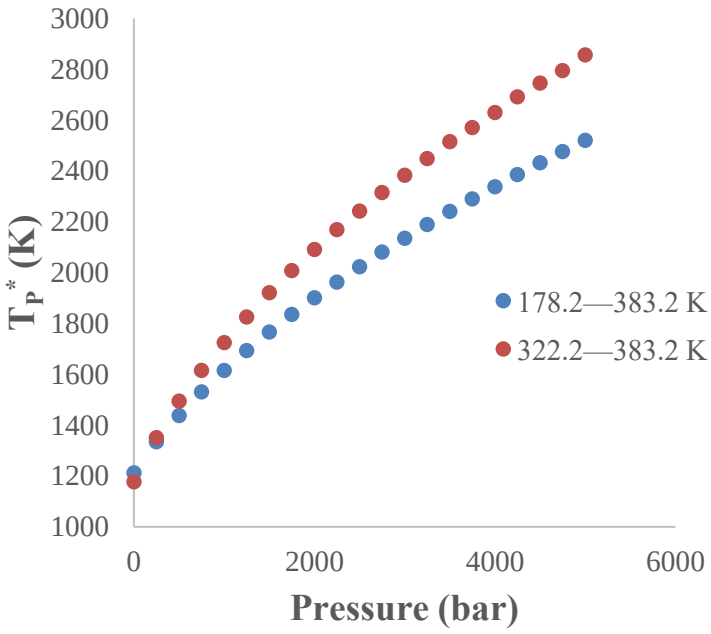

Figure 6.7: Plots of T_P^* for toluene vs. pressure calculated with data spanning two different temperature ranges

This dependence of intercepts on temperature ranges, and the small, but nonzero values of $(\partial\rho/\partial T)_P$ suggest that the isobaric density is a nonlinear function of temperature that exhibits minimal curvature over an extended temperature range. This relationship is, however, accurate over the entire NLR, and an equation for density of the form of (6.223) may be used for liquids under nearly isobaric conditions and NLR

temperatures. A linear density/temperature relationship is particularly useful in linking theoretical volumetric interpretations of mobility properties of liquids with observed temperature dependences.

The specific free volume (SFV) is given by:

$$SFV = V - V_0 \tag{6.24}$$

in which V_0 is the specific occupied volume. Often V_0 is taken as the specific volume of the medium extrapolated to absolute zero[82,120,121], but it may also be generally defined as the specific limiting volume of the system in which $SFV \rightarrow 0$[122,123]. Equation (6.23) provides a simple means of extrapolating the specific volume of liquids and liquid mixtures to absolute zero. With (6.23):

$$V_0 = (\rho_P^*)^{-1} = \left[\sum \phi_i^* \rho_{i,P}^*(P)\right]^{-1} \tag{6.25}$$

Extrapolation methods that account for the curvature of density/temperature isobars above the NLR consistently predict larger V_0 (smaller ρ_P^*)[105,120,124,125], but for Group II liquids, the difference between V_0 calculated with a linear density extrapolation and a nonlinear method is often a small fraction of the liquid specific volume at NLR temperatures[126]. Another means of calculating V_0 (mass intensive) for polymers, popularized by Lee[127], relates V_0 to the van der Waals volume (V_{vdw}) by:

$$V_0 = 1.3V_{\mathrm{vdw}} \tag{6.26}$$

in which V_{vdw} is calculated by a group contribution method[128]. In his investigation into the 1.3 factor, Horn[121] traces its origins to an assertion by Van Krevelen[129] which

was likely based on an approximation for polymer models. Comparison of calculated V_{vdw} with extrapolated density data for polymers show that 1.3 is a decent estimate, but deviation is significant enough that the factor should not be considered a universal constant[82]. Horn concludes that direct extrapolation is preferable to the 1.3 factor.

The fractional free volume (FFV) is defined as the ratio of SSV to specific system volume. Setting $\rho_P^* = V_0^{-1}$ and using equation (6.23) for $\rho = V^{-1}$ gives for FFV:

$$FFV = \rho SFV = 1 - \frac{\rho}{\rho_P^*} = \frac{T}{T_P^*} \tag{6.27}$$

When density is a linear function of temperature, FFV is directly proportional to temperature, with a proportionality constant of $1/T_P^*$. Sanchez and Cho observed this FFV dependence for pure, amorphous polymers at low pressures[82], but they calculated FFV at elevated pressures through their equation of state, and neither small molecules nor solutions were considered. At a given pressure, mixing rule (6.21) and equation (6.27) offer direct composition and temperature dependences of FFV.

Free volume correlations are frequently used to explain the effects of density on mobility properties in amorphous media, particularly in polymers[120,123,127,130,131]. The empirical relationship by Doolittle[120] and Williams, Landel, and Ferry[132] for viscosity η_v (the subscript is only to distinguish viscosity from occupied volume fraction), and the related theoretical expression by Cohen and Turnbull[123] for the diffusion coefficient $\mathcal{D}$ in liquids, both have the functional form:

$$\eta_v, \mathcal{D} = A \exp[B/SFV] \tag{6.28}$$

in which B (positive for η, negative for $\mathcal{D}$) depends on composition and accounts for both free volume overlap and the minimum volume required for either molecular or segment motion. A has different theoretical interpretations depending on the property it correlates. A depends on composition and temperature, but its temperature dependence is weaker than the exponential contribution[133,134].

When FFV is directly proportional to temperature, as in (6.27), equation (6.28) and similar hybrid free volume/activation models[133,134] yield:

$$\eta_v, \mathcal{D} = A \exp[-B\rho_P^*] \exp[B\rho_P^* T_P^*/T] \tag{6.29}$$

Since $\exp[-B\rho^*(P)]$ is independent of temperature it may be absorbed into A without changing the overall temperature dependence of (6.29). With $\exp[-B\rho^*(P)]$ absorbed into A, (6.29) adopts an Arrhenius type temperature dependence, a relationship frequently invoked to correlate the effects of temperature on mobility properties[133,135,136].

6.5 SUMMARY AND CONCLUSIONS

Isobaric plots of density vs. temperature are linear for liquids over a large temperature range. For small molecule liquids, this temperature range extends from the melting to at least the normal boiling temperatures. This linearity, discussed in Chapter 5 for liquids at low pressure, was shown to be the general, nearly universal behavior of liquid density/temperature isobars. It accurately describes the density/temperature relationship of small molecular liquids, polymer melts, and liquids mixtures, at both low and elevated pressures. Appendix B contains low pressure line parameters for 140 pure liquids for the simple and accurate calculation of densities in the normal liquid range. Values in Table B1 used with the mixing rules developed can calculate liquid density

while maintaining the density/temperature linearity. Due to the strong dependence of the line parameters on the fitting conditions (particularly at elevated pressures), this linearity cannot be developed into a consistent thermodynamic model, like the SPT model. In Chapter 7, a new thermodynamic model for small, weakly attractive molecules is developed. This new model exhibits negligible curvature over much of the $Z \simeq 0$ isobar, and it emphasizes the role of occupied volume through the interrelation between a limited coordination number/occupied volume fraction and potential energy saturation.

Chapter 7: Quasi-Chemical Square Well Model of Fluids*

While much of [125] focuses on the thermodynamics of glasses and the implications of this model, the model itself was developed to more realistically describe the potential energy of an attractive sphere by limiting the attraction range of each sphere.

7.1 INTRODUCTION

Ideas and models of the glass transition remain engaging subjects[137,138] decades after the introduction of theories and concepts[139]. In 1948 Kauzmann noted that when the metastable liquid entropy line is extended to low temperatures, the extrapolation falls to the crystal entropy at what is now known as the "Kauzmann temperature"[140], motivating interest in the nature of the glass transition. The liquid-to-glass transition intervenes before the extension of this line reaches the crystal entropy, resolving the "entropy catastrophe." Though the glass transition resolves a thermodynamic issue, the resolution in and of itself does not answer whether or not it is a true thermodynamic transition. A review of this subject is given in reference [141].

In 1958 Gibbs and DiMarzio argued that the glass transition was a thermodynamic, second-order phase transition with a statistical lattice model of polymer liquids that they developed[142]. They proposed that the observed liquid-to-glass transition in polymeric systems is a kinetically controlled manifestation of this underlying thermodynamic transition, a dogma which prevails, but with occasional criticism[143]. The Gibbs-DiMarzio interpretation was developed for long chain polymers, but simple molecules such as toluene or elemental sulfur also exhibit glass transitions. In this chapter

* This material was published as: Isaac C. Sanchez, and Sean O'Keefe, "Theoretical Rationale for a Thermodynamic Glass State" *J. Phys. Chem. B* 120 (35), 9443 (2016)[125]. For the article Sean Patrick O'Keefe contributed the appendix and refined the model and its approximations. For the purposes of this dissertation Sean Patrick O'Keefe recalculated all values and corrected the excess entropy equation.

physical principles of glasses are addressed within the context of a quasi-chemical square well model developed for small molecules, with short-ranged attractive interactions.

Like the models discussed in Chapter 1–4, hard sphere (HS) contributions to this model are considered using Scaled Particle Theory (SPT), but this SPT model is treated as a square-well (SW) fluid in a quasi-chemical (QC) approximation. A SW potential includes both attractive and repulsive interactions:

$$u(R) = \begin{cases} \infty & R < \sigma \\ -\varepsilon & \sigma \leq R \leq \lambda\sigma \\ 0 & R > \lambda\sigma \end{cases} \tag{7.1}$$

Others have developed QC type approximations for a SW fluid[144–147]. Those studies concentrated on calculating the effective coordination number of a HS and using that result to calculate the free energy by isothermal integration of the energy, or by simply adding the calculated energy to a HS equation of state. The present approach proceeds via the chemical potential route discussed in Chapter 2 for the SPT chain model. This model clearly defines what additional approximations must be made within the context of a QC approach.

7.2 QUASI-CHEMICAL APPROXIMATION

Because of excluded volume crowding, a HS can attract at most a maximum number $n_{\max}$ of other spheres into its attractive domain. When $\lambda = 1$, the excluded volume around the central sphere equals eight times the HS volume of $v_0 = \pi\sigma^3/6$. The shell volume V_S accessible for the placement of spheres within the attractive domain of a central sphere is given by:

$$V_S = 8(\pi\sigma^3/6)(\lambda^3 - 1) \tag{7.2}$$

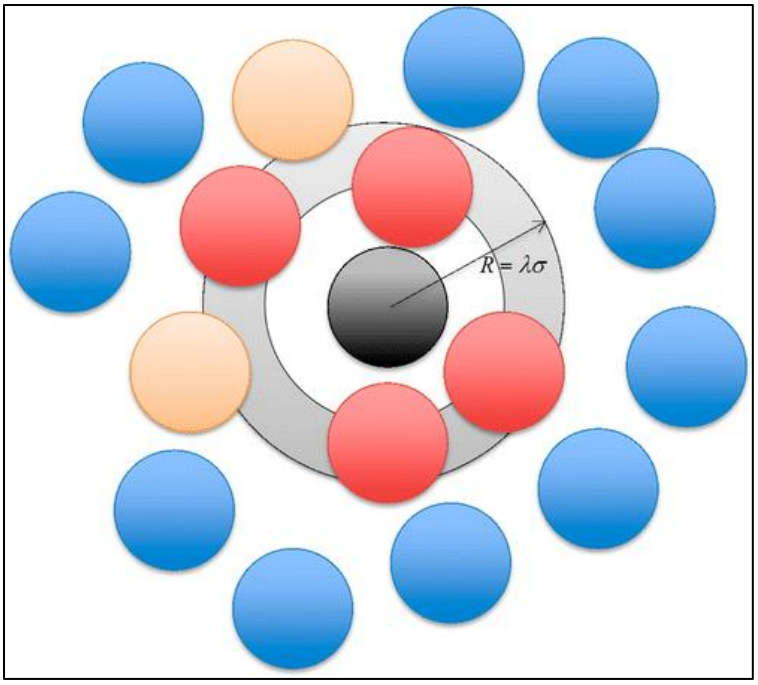

Figure 7.1: Two-dimensional schematic illustrates the contribution of hard spheres (HS) to the occupied volume in the attraction shell around the central sphere

The fraction of space occupied by $n_{\max}$ spheres within the shell volume is approximately given by:

$$\frac{n_{\max}(\pi\sigma^3/6)}{V_S} = \frac{n_{\max}}{8(\lambda^3 - 1)} = \eta_{\max} \tag{7.3}$$

in which $\eta_{\max}$ is the maximum possible occupied volume fraction within the attraction shell. For random close packing, $\eta_{\max} \simeq 0.64$[148], but $\eta_{\max}$ is a parameter fixed by λ and the choice of $n_{\max}$.

Figure 7.1 schematically illustrates the HS contribution to the occupied volume in the attraction shell (the gray annulus) around the black sphere. The volume of the attraction shell is $8(\lambda^3 - 1)v_0$. Although portions of a HS can enter the unoccupied excluded volume region (the white annulus), HS centers cannot. Each red sphere center

in the attraction shell experiences an attractive energy of $-\varepsilon$, but each sphere itself only partially contributes to the occupied volume in the attraction shell. In contrast, an orange sphere whose center lies outside the attraction shell can still contribute to the occupied volume in the attraction shell. In Figure 7.1, $\lambda = 3/2$ and the volume of the attractive shell is $19v_0$, but shrinks to $7.625v_0$ for $\lambda = 1.25$. As $\lambda \to \infty$, a SW fluid approaches a van der Waals (VDW) limit[149]. Equation (7.3) better approximates $\eta_{\max}$ as λ increases.

In the spirit of a QC approximation, the probability $\mathbf{P}_n$ that n sphere centers are within the attraction domain of a given sphere is given by a binomial distribution[150]:

$$\begin{aligned} \mathbf{P}_n &= \binom{n_{\max}}{n} \left(ze^{\beta\varepsilon}\right)^n / Q \\ Q &= \sum_{n=0}^{n_{\max}} \binom{n_{\max}}{n} \left(ze^{\beta\varepsilon}\right)^n = \left(1 + ze^{\beta\varepsilon}\right)^{n_{\max}} \end{aligned} \tag{7.4}$$

where $\beta = (kT)^{-1}$ and z is a QC parameter to be determined self-consistently. The average number of interacting spheres within the attractive shell volume V_S is given by:

$$\langle n \rangle = \sum_{n=0}^{n_{\max}} n\mathbf{P}_n = \frac{\partial \ln Q}{\partial(\beta\varepsilon)} = n_{\max} \frac{ze^{\beta\varepsilon}}{1 + ze^{\beta\varepsilon}} \tag{7.5}$$

η_S is given by:

$$\eta_S = \frac{\langle n \rangle (\pi\sigma^3/6)}{V_S} = \eta_{\max} \frac{ze^{\beta\varepsilon}}{1 + ze^{\beta\varepsilon}} \tag{7.6}$$

Equation (7.6) is not rigorously correct. Figure 7.1 shows that spheres with centers that lie outside the attractive domain ($R > \lambda\sigma$) can also contribute to the local occupied fraction, and spheres with centers within the attraction zone may not contribute their entire volume to the occupied fraction. From geometry, a local occupied volume

fraction can be defined and measured in computer simulations[151], but for simplicity this is not employed here.

For large λ, the occupied volume fraction in the attractive shell must approach the global volume fraction, $\lim_{\lambda\to\infty} \eta_S = \eta$, where η retains the definition $\eta = (\pi\sigma^3/6)\rho$, with ρ as the number density. This corresponds to the VDW limit where $\lambda \to \infty$ and $\varepsilon \to 0$, but the product $\lambda\varepsilon$ remains fixed. Using this as an approximation for all values of λ yields a self-consistent value for the z parameter:

$$\lim_{\beta\varepsilon\to 0} \eta_S = \eta = \eta_{\max} \frac{z}{1+z}$$
$$z = \frac{\eta}{\eta_{\max} - \eta} \equiv \frac{\theta}{1-\theta} \tag{7.7}$$

where $\theta = \eta/\eta_{\max}$ is the average occupied fraction in the attraction shell in the high temperature limit. In application of the model, λ is set to small, finite values $(1.25 \le \lambda \le 2)$, the interaction energy is nonzero, and equation (7.7) accurately calculates the local occupied volume fraction at low densities only. Rigorously, a SW fluid behaves like a HS fluid in the limit $\beta\varepsilon \to 0$. A HS fluid has a local density greater than the global density[152], but this local HS density lacks a simple, analytical solution, and its use would require complicated numerical implementation to calculate thermodynamic properties. Despite its approximate origin, equation (7.7) is preferred to a numerical HS solution for the purposes of this model. Substituting this result into equation (7.5) yields:

$$\frac{\langle n \rangle}{n_{\max}} = \frac{\theta e^{\beta\varepsilon}}{1 + \theta(e^{\beta\varepsilon} - 1)} \tag{7.8}$$

This interpretation of θ always holds providing λ is large, but becomes an approximation for small λ. Notice that as $\beta\varepsilon \to \infty$, $\langle n\rangle/n_{\max} \to 1$.

Number fluctuations within the attractive shell are given by:

$$\langle n^2\rangle - \langle n\rangle^2 = \frac{\partial\langle n\rangle}{\partial(\beta\varepsilon)} = n_{\max}\frac{\theta(1-\theta)e^{\beta\varepsilon}}{[1+\theta(e^{\beta\varepsilon}-1)]^2} \tag{7.9}$$

and fluctuations relative to the mean are:

$$\frac{\sqrt{\langle n^2\rangle - \langle n\rangle^2}}{\langle n\rangle} = e^{-\beta\varepsilon/2}\sqrt{\frac{(1-\theta)/\theta}{n_{\max}}} \tag{7.10}$$

There are two limits where the fluctuations vanish: as $T \to 0$ and as $n_{\max} \to \infty$. The latter occurs at all temperatures and is characteristic of a VDW type model.

7.3 QCSW THERMODYNAMIC PROPERTIES

7.3.1 Configurational Energy

Let $\psi = -n\varepsilon$ be the attractive interaction energy of a HS with n other HSs in its interaction domain. The average interaction energy per HS is

$$\langle\psi\rangle = -\langle n\rangle\varepsilon = -n_{\max}\varepsilon\frac{\theta e^{\beta\varepsilon}}{1+\theta(e^{\beta\varepsilon}-1)} \tag{7.11}$$

The configurational energy contribution to the constant volume heat capacity is given by:

$$\frac{C_V}{k} = (\beta\varepsilon)^2\frac{\partial\langle n\rangle}{\partial(\beta\varepsilon)} = (\beta\varepsilon)^2[\langle n^2\rangle - \langle n\rangle^2] \tag{7.12}$$

7.3.2 Equation of State and Chemical Potential

Now let $\mathbf{P}_0(\psi)d\psi$ be the probability that a random insertion of a HS yields interaction energy ψ and $\mathbf{P}(\psi)d\psi$ be the probability that any HS already in the fluid exhibits interaction energy ψ. These two distributions are related by[32]:

$$\mathbf{P}(\psi) = \frac{\mathbf{P}_0(\psi)e^{-\beta\psi}}{\mathbf{B}} \tag{7.13}$$

in which $\mathbf{B}$ is the insertion factor. Noting $\mathbf{P}_0(\psi > 0) = \mathbf{P}(\psi > 0) = 0$, equation (7.13) provides a useful and insightful definition for the insertion factor:

$$\begin{aligned}\mathbf{B} &= \frac{\int_{-\infty}^{\infty}\mathbf{P}_0(\psi)d\psi}{\int_{-\infty}^{\infty}\mathbf{P}(\psi)e^{\beta\varepsilon}d\psi} = \frac{\int_{-\infty}^{0}\mathbf{P}_0(\psi)d\psi + \int_{0}^{\infty}\mathbf{P}_0(\psi)d\psi}{\int_{-\infty}^{0}\mathbf{P}(\psi)e^{\beta\varepsilon}d\psi + \int_{0}^{\infty}\mathbf{P}(\psi)e^{\beta\varepsilon}d\psi} \\ &= \frac{\int_{-\infty}^{0}\mathbf{P}_0(\psi)d\psi + 0}{\int_{-\infty}^{0}\mathbf{P}(\psi)e^{\beta\varepsilon}d\psi + 0} = \frac{\int_{-\infty}^{0}\mathbf{P}_0(\psi)d\psi}{\int_{-\infty}^{0}\mathbf{P}(\psi)e^{\beta\varepsilon}d\psi} = \frac{\mathbf{P}_{ins}}{\langle e^{\beta\psi}\rangle}\end{aligned} \tag{7.14}$$

where $\mathbf{P}_{ins}$ is the insertion probability for a successful random insertion of a HS into a HS fluid with an average interaction energy per sphere of $\langle\psi\rangle$. Taking the logarithm of (7.14) gives:

$$\ln\mathbf{B} = \ln\mathbf{P}_{ins} - \ln\langle\exp[-\beta\varepsilon n]\rangle \tag{7.15}$$

$\langle\exp[-\beta\varepsilon n]\rangle$ can be calculated exactly in the QC approximation:

$$\begin{aligned}\langle\exp[-\beta\varepsilon n]\rangle &= \sum_{n=0}^{n_{\max}}\mathbf{P}_n\exp[-\beta\varepsilon n] = \frac{\sum_{n=0}^{n_{\max}}\binom{n_{\max}}{n}z^n}{Q} \\ &= \left[1+\theta\left(e^{\beta\varepsilon}-1\right)\right]^{-n_{\max}}\end{aligned} \tag{7.16}$$

Substituting equation (7.16) into (7.15) gives:

$$\ln \mathbf{B} = \ln \mathbf{P}_{ins} + n_{\max} \ln\left[1 + \theta\left(e^{\beta\varepsilon} - 1\right)\right] \tag{7.17}$$

The required insertion probability can be approximated with the SPT model[10]:

$$\ln \mathbf{P}_{ins} = \ln(1-\eta) - \frac{\eta(14 - 13\eta + 5\eta^2)}{2(1-\eta)^3} \tag{7.18}$$

Equation (7.18) is equivalent to (2.6) for a pure HS fluid ($\sigma_{-k} = \sigma^{-k}$). To within a function of temperature, the chemical potential is given by[32]:

$$\begin{aligned} \beta\mu &= \ln \rho - \ln \mathbf{B} \\ &= \mu_{ig}(T,P) - \ln(Z\mathbf{B}) = \mu_{ig}(T,\rho) - \ln \mathbf{B} \end{aligned} \tag{7.19}$$

$\mu_{ig}(T,P)$ is the chemical potential of an ideal gas at the same temperature and pressure of the QCSW fluid, and $\mu_{ig}(T,\rho)$ is the chemical potential of an ideal gas at the same temperature and density as the QCSW fluid.

The EOS is given through isothermal integration of the Gibbs-Duhem equation:

$$Z = 1 - \ln \mathbf{B} + \frac{1}{\eta}\int_0^{\eta} \ln \mathbf{B}\, d\eta = Z_{SPT} + Z_{\text{int}} \tag{7.20}$$

where Z_{SPT} is the SPT contribution to the EOS that arises from $\ln \mathbf{P}_{ins}$ and Z_{int} is the contribution from attractive interactions:

$$Z_{\text{int}} = n_{\max}\left\{\frac{\ln[1 + \theta\left(e^{\beta\varepsilon} - 1\right)}{\theta(e^{\beta\varepsilon} - 1)} - 1\right\} \tag{7.21}$$

The complete EOS is:

$$Z = \frac{1+\eta+\eta^2}{(1-\eta)^3} + n_{\max}\left\{\frac{\ln\left[1+\theta\left(e^{\beta\varepsilon}-1\right)\right]}{\theta\left(e^{\beta\varepsilon}-1\right)} - 1\right\} \qquad (7.22)$$

$$Z = 1 + b_2\eta + b_3\eta^2 \ldots$$

The dimensionless virial coefficients are given by:

$$b_k = 1 + \frac{3}{2}k(k-1) + n_{\max}\frac{(-1)^{k+1}}{k}\left[\frac{e^{\beta\varepsilon}-1}{\eta_{\max}}\right]^{k-1} \quad k \geq 2 \qquad (7.23)$$

b_2 is the correct dimensionless second virial coefficient for the SW potential:

$$b_2 = 4\left[1 - (\lambda^3 - 1)\left(e^{\beta\varepsilon}-1\right)\right] \qquad (7.24)$$

7.3.3 Critical Properties

The critical point is determined by:

$$\left.\frac{\partial(\eta Z)}{\partial\eta}\right)_T = \left.\frac{\partial^2(\eta Z)}{\partial\eta^2}\right)_T = 0 \qquad (7.25)$$

The critical temperature is given by:

$$\exp[\beta_c\varepsilon] = 1 + \frac{1}{\theta_c\left[\frac{n_{\max}(1-\eta_c)^4}{(1+2\eta_c)^2} - 1\right]} \qquad (7.26)$$

in which η_c, β_c, and θ_c are values of η, β, and θ at the critical point. η_c is given by the single positive root of the polynomial:

$$(1+2\eta_c)^3 + n_{\max}(1-\eta_c)^3[6\eta_c^2 + 7\eta_c - 1] = 0 \qquad (7.27)$$

The critical volume fraction is determined by the maximum number of sphere centers that can be accommodated within the accessible shell volume $n_{\max}$. As $n_{\max} \to \infty$, or equivalently as $\lambda \to \infty$, η_c reaches the SPT value given in Table 2.1:

$$\lim_{n_{\max}\to\infty} \eta_c = \frac{\sqrt{73}-7}{12} = 0.1287 \tag{7.28}$$

At the other extreme, as $n_{\max} \to 1$, $\eta_c \to 0$, and the critical temperature $T_c \to 0$ by equation (7.26); as a consequence, the liquid-vapor transition vanishes as $n_{\max} \to 1$.

7.3.4 VDW Limit

The SPT model uses a VDW type energy in which every HS attractively interacts with ever other HS in the system, or equivalently $n_{\max}, \lambda \to \infty$. The effect of the interaction range on the model can be seen by keeping the product $n_{\max}\varepsilon$ constant while letting $\varepsilon \to 0$ and $n_{\max} \to \infty$. In this VDW limit, the interaction energy per HS remains constant as the attractive interaction range, as measured by λ, approaches ∞.

$$\begin{aligned} Z &= \frac{1+\eta+\eta^2}{(1-\eta)^3} - \frac{n_{\max}\varepsilon}{2}\theta\beta[1 + O(\beta\varepsilon) + O(\beta\varepsilon)^2 \dots] \\ \lim_{\substack{n_{\max}\to\infty \\ \varepsilon\to 0}} Z &= \frac{1+\eta+\eta^2}{(1-\eta)^3} - \eta\frac{n_{\max}\varepsilon}{2kT\eta_{\max}} \end{aligned} \tag{7.29}$$

From (7.29), the SPT T^* is related to the QCSW parameters through:

$$T^*_{SPT} = \frac{n_{\max}\varepsilon}{2k\eta_{\max}} \tag{7.30}$$

This SW to VDW transitional behavior has been observed in MC simulations where the phase diagram shifts from a cubic (non-classical) to a parabolic (classical) type as λ increases[153,154]. Attractive contributions to the EOS behave differently in the VDW limit. In equation (7.29) the attractive contribution to Z diverges as $T \to 0$, while in equation (7.22) it does not.

7.4 MODEL PARAMETERS

Three parameters characterize the SW potential: the well depth ε, the HS diameter σ, and the well width $\lambda\sigma$; ε establishes the temperature scale ($\beta\varepsilon$) and $\pi\sigma^3\rho/6$ defines the HS volume fraction, η. Monte Carlo (MC) studies of the SW potential[145,153–155] have primarily focused on the range =$1.25 \leq \lambda \leq 2$ with $\lambda = 3/2$ a popular choice. For $\lambda > 7/4$ the SW model begins to exhibit mean-field (VDW) like character[153,154].

The QCSW model introduces an additional parameter, $n_{\max}$, the maximum number of atoms that can be accommodated in the attraction zone around a HS. MC studies indicate that $n_{\max} \simeq 12$ as a high-density limit for $\lambda = 3/2$[156]. It also agrees with a calculation using pair distribution functions for HS fluids (see Appendix C). A choice of $n_{\max} = 12$ and $\lambda = 3/2$ defines the maximum packing fraction $\eta_{\max}$ within the attraction shell:

$$\eta_{\max} = \frac{n_{\max}}{8(\lambda^3 - 1)} = \frac{12}{19} = 0.63 \tag{7.31}$$

An $\eta_{\max}$ of 0.63 agrees well with what is believed to be a good estimate of random close packing of spheres of the same size[148]; however, MC simulations indicate that the triple point for $\lambda = 3/2$ occurs at $\eta = 0.437$[157], suggesting the SW fluid will crystallize well before the high-density limit of 0.63 is reached.

7.5 EVIDENCE FOR A THERMODYNAMIC GLASS STATE

Figure 7.2 plots calculated saturated liquid density in the NLR ($Z \simeq 0$) for $\lambda = 3/2$ and $n_{\max} = 12$. For the purposes of the calculations here, the NLR was defined such that $T_R \equiv T/T_c = \beta_c\varepsilon/\beta\varepsilon \leq 0.8$. This roughly corresponds to the temperature range at which $Z \simeq 0$ for saturated liquids[1]. For $\lambda = 3/2$ and $n_{\max} = 12$, equations (7.26) and (7.26) give $\beta_c\varepsilon = 0.89$.

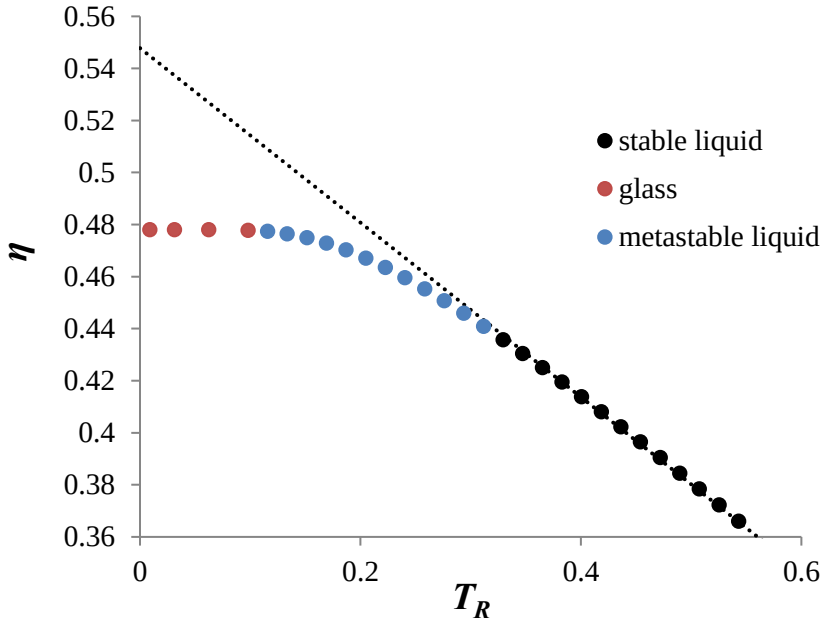

Figure 7.2: Variation of occupied volume fraction with reduced temperature for the QCSW and the η, T_R line for the stable liquid extrapolated to low temperatures

In Figure 7.2, the stable liquid was defined such that η along the $Z \simeq 0$ isobar was less than the simulated liquid density of 0.437 at the SW triple point from simulation[157]. As $Z \to 0$, the QCSW EOS reduces to a temperature independent equation:

$$\lim_{\beta\varepsilon\to\infty} Z = \frac{1+\eta+\eta^2}{(1-\eta)^3} - n_{\max} = 0 \tag{7.32}$$

The solution of this equation for $n_{\max} = 12$ is $\eta = 0.478$. In Figure 7.2, glass states are operationally defined by $\langle n \rangle / n_{\max} > 0.999$. The metastable liquid is defined in Figure 7.2 as fluids for which $0.437 < \eta < 0.478$ along $Z \simeq 0$. In Figure 7.2 the density indeed approaches $\eta = 0.478$ as the temperature approaches zero. Mean-field (VDW type) equations of state do not display this behavior. Physically, the attraction shell, which can only accommodate $n_{\max}$ HS centers, begins to saturate well before zero temperature is reached. For example, equation (7.8) calculates $\langle n \rangle / n_{\max} > 0.99$ at $\beta\varepsilon = 4$ (or T/T_c=0.22) along the $Z \simeq 0$ isobar. Once the attraction shell saturates, further lowering of temperature no longer influences the EOS.

This limiting density is the global density; the local density in the attraction shell around a HS at saturation as given by equation (7.7) approaches $\eta_{\max} = 0.63$. If the central atom and its excluded volume were included in local density calculations, the local density of a 13 HS cluster increases to $13/(8\lambda^3) = 13/27 = 0.481$, which is within two significant figures of the global density of 0.478. This reflects well on the self-consistency of the QCSW model for the choices $\lambda = 3/2$ and $n_{\max} = 12$.

For a completely repulsive system, such as a HS fluid, density is controlled by βP where P is the pressure. In a system with attractive interactions of strength ε, both βP and $\beta\varepsilon$ control the density with density increasing as either variable increases, but for a liquid in equilibrium with its vapor at temperatures below its normal boiling point, only $\beta\varepsilon$ controls the density with repulsive forces acting to keep the liquid from completely collapsing. At some condensed state, the liquid may become so dense that its density no longer responds to an increase in $\beta\varepsilon$. For example, if attractive interactions were added to a metastable HS fluid ($\eta > 0.494$), intuitively the density would not be expected to change much provided that the system remained disordered (density would noticeable

increase if crystallization intervened). From a qualitative viewpoint, the QCSW model is consistent with the idea that attractive interactions become ineffective in controlling liquid density at high densities, and a hypothetical limiting density, defined by the force balance, might be reached. The observed limiting density of 0.478 is in the metastable liquid regime, at a greater occupied volume fraction than the triple point η of 0.437 for an SW fluid at $\lambda = 3/2$. It represents a density defined through equation (7.32) where the liquid gets "stuck." Once attractive forces become ineffective, the liquid approaches a density that defines a balance of attractive and repulsive (packing) forces. If the more accurate Carnahan-Starling EOS[157] is used, this limiting density becomes 0.488, about 2% greater[52] than 0.478.

Some insight can also be gained by calculating the liquid entropy:

$$-\ln(Z\mathbf{B}) = \beta\left[\mu - \mu_{ig}(T,P)\right] = \beta[U^E - TS^E] \tag{7.33}$$

where the superscript E denotes an excess property relative to an ideal gas at the same temperature and density. The excess internal energy may be taken as:

$$\beta U^E = \beta\langle\psi\rangle \tag{7.34}$$

With (7.33) and (7.34) the excess entropy of the fluid relative to an ideal gas at the same density and temperature is given by:

$$S^E/k = \ln(\mathbf{B}) + \beta\langle\psi\rangle \tag{7.35}$$

At low temperatures where $Z \to 0$, S^E becomes a function of density only:

$$\lim_{\beta\varepsilon\to\infty} S^E/k = \ln \mathbf{P}_{ins} + n_{\max} \ln \theta \\ = -19 \quad \text{for } \eta = 0.478 \tag{7.36}$$

Figure 7.3 illustrates this excess entropy as a function of temperature. Equation (7.36) indicates that S^E asymptotes to a finite value at low temperatures and avoids the "entropy catastrophe." At about $T_R < 0.1$, the liquid becomes a glass.

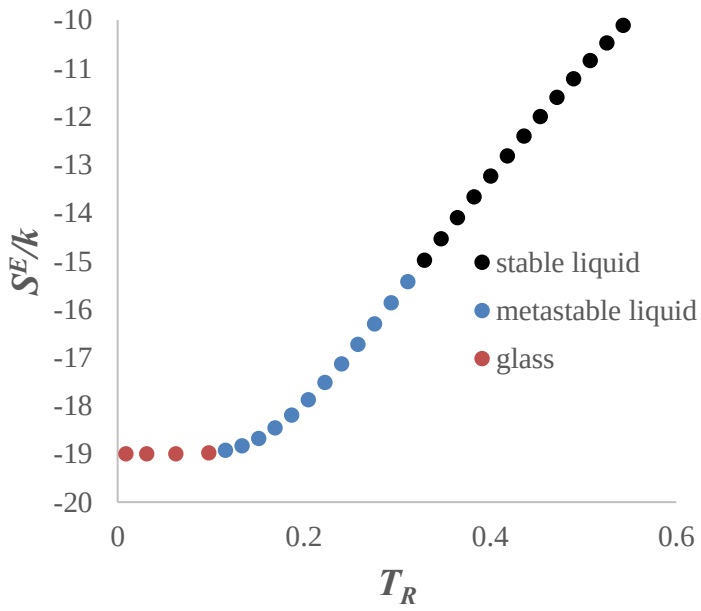

Figure 7.3: Plot of excess configurational entropy calculated from equation (7.35) against T_R. The densities in Figure 7.2 were used here

For comparison, this entropy change for a HS fluid is given by:

$$S^E/k = \ln \mathbf{P}_{ins} = -15.7 \quad \text{for } \eta = 0.478 \tag{7.37}$$

This reveals that adding attractive interactions to a HS fluid causes an additional lowering of the entropy. Attractive interactions act to restrict the available configuration space. This loss of configuration space corresponds to an entropy loss. A lowering of the configurational energy compensates for this entropy loss (energy-entropy compensation).

7.6 APPROXIMATE NATURE OF THE QCSW MODEL

Although the QCSW model provides a new physical insight, it remains an imperfect model. As an example, the predicted QCSW critical properties for $\lambda = 3/2$ and $n_{\max} = 12$ are $\eta_c = 0.1043$ and $kT_c/\varepsilon = 1.136$, both lower than the exact MC values of $\eta_c = 0.16$ and $kT_c/\varepsilon = 1.218$[155]. The QC approximation used to calculate $\langle \exp(-n\beta\varepsilon) \rangle$ in (7.15) takes into account short-range fluctuations in energy, but fails to account for the long wavelength density fluctuations that occur near the critical point.

In equation (7.14), the insertion probability for a SW fluid will have a finite number of contributions:

$$\mathbf{P}_{ins} = \mathbf{P}_0(0) + \mathbf{P}_0(-\varepsilon) + \mathbf{P}_0(-2\varepsilon) \tag{7.38}$$

$\mathbf{P}_0(-n\varepsilon)$is the probability that a random insertion of a HS into the SW fluid system of density η will result in n attractive interactions. These probabilities will depend on the average interaction energy, $\langle \psi \rangle$, at the given fluid density. In deriving the QCSW chemical potential, the approximation is made that $\mathbf{P}_{ins} = \mathbf{P}_0(0)$ where $\mathbf{P}_0(0)$ is approximated as the HS fluid insertion probability given by equation (7.18). This approximation is most applicable at high densities since the void distribution in a SW fluid at high densities should not differ much from that of a HS fluid.

7.7 SUMMARY

As a liquid becomes dense, repulsive forces control its structure and density, while attractive forces play a minor role. Mean-field models in the VDW genre do not yield this qualitative result. Instead, attractive force contributions to the EOS increase with decreasing temperature and diverge as $T \to 0$ as $1/T$. This negative divergence requires the repulsive contribution to the EOS to diverge positively and sometimes at a nonphysical value of density. The mean-field SPT model predicts $\eta \to 1$ as $T \to 0$, a physically impossible occupied volume fraction for a HS mixture. In contrast, the QCSW model indicates that this tug-of-war between attractive and repulsive forces results in a unique and physically realistic limiting density at low temperatures. For $\lambda = 3/2$ and $n_{\max} = 12$, this limiting density is $\eta = 0.478$, which is greater than the triple point density determined from MC simulations (0.437)[157], but less than equilibrium fluid-to-solid transition density of a HS system ($\eta = 0.494$)[158]. Using the MC value of the critical occupied volume fraction ($\eta_c = 0.16$) to reduce the QCSW η, the QCSW reduced density at the low temperature limit is $\rho_R \equiv \eta/\eta_c = 3.0$. Many simple liquids such as the inert elements, methane, and Lennard-Jones fluids[159] begin to freeze at reduced densities of about 2.6. A reduced density of 3 would place the QCSW limiting density in the metastable liquid range for simple fluids.

The are other checks on the physical reasonableness of the QCSW model. The stable liquid points in Figure 7.2 more than span much of the NLR and were used to form the dotted line shown in the figure ($R^2 > 0.999$). If this line is extended to zero temperature, it intersects at $\eta = 0.548$, or at a reduced density of $0.548/0.16 = 3.4$. Extrapolation of experimental density data for Ar, Kr, Xe, CH_4, S, O_2, and N_2 to zero temperature yields an average intercept of $\rho_R = 3.6227$ in reasonable agreement with the QCSW value of 3.4. As an additional observation of interest, the density $\eta \simeq 0.54$ also

corresponds to the estimated Kauzmann density for the putative fluid-to-glass transition for hard spheres[151].

The QCSW model does not exhibit a second order phase transition to define a clear boundary between glass and liquid states; however, with decreasing temperature both the thermal expansion coefficient and the QCSW contribution to the heat capacity dramatically decrease and asymptote to zero at zero temperature. The QCSW configurational energy contribution to the heat capacity calculated with equation (7.12) is illustrated in Figure 7.4. This behavior might be termed a pseudo second order phase transition and tends to mimic what is often observed experimentally. The QCSW model predicts that on cooling the liquid gets "stuck" at a density where the configurational energy has saturated. This causes other thermodynamic properties, such as the configurational entropy, to also saturate. Without the clearly defined thermodynamic definition of the liquid-to-glass transition, for the purposes of the QCSW, the liquid-to-glass transition is operationally defined as occurring when the configurational energy reaches 99.9% of its saturated value. For $\lambda = 3/2$ and $n_{\max} = 12$, this occurs near $\beta\varepsilon = 10$ (or about $T/T_c = 0.1$).

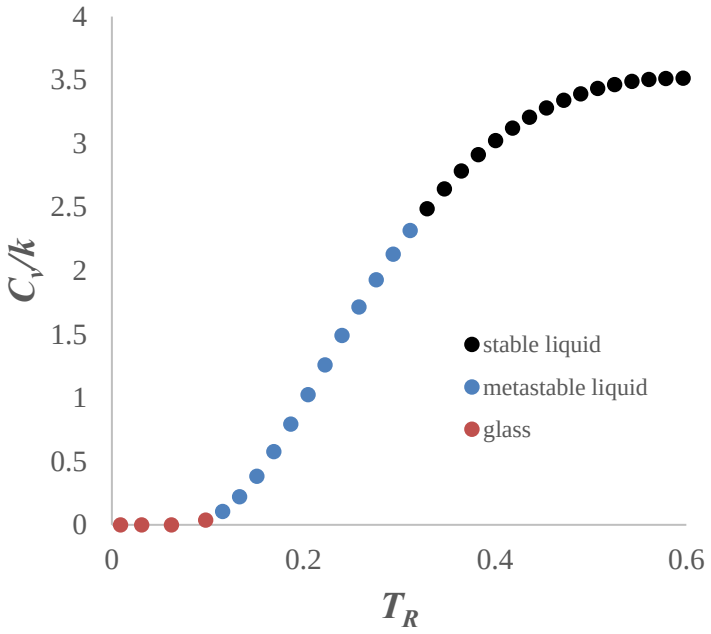

Figure 7.4: Variation of the QCSW contribution to the constant volume heat capacity with temperature.

This view of the glass transition differs from the prevailing interpretation that the ideal thermodynamic liquid-to-glass transition occurs when the configurational entropy reaches zero (or a constant) via a second order phase transition. Similarity exists in the sense that the configurational entropy of the QCSW model reaches a limiting value, but the limiting entropy property of the QCSW model is a direct consequence of configurational energy saturation. For short-range attractive interactions, excluded volume limits the number of other spheres within the attractive domain of a given sphere. At high densities, this limiting number is quickly approached. In real molecular systems with short-range interactions, whether monomeric or polymeric, the same limited attractive interactions between atoms or group of atoms are expected to prevail.

7.8 CONCLUSION

The QCSW model endorses the intuitive concept that at high densities, the short-ranged attractive contribution to the configurational energy begins to saturate before zero temperature is reached. As a consequence of this saturation, the balance between repulsive and attractive forces defines a unique liquid density, which effectively becomes temperature independent. This fixed density in turn establishes the value of the configurational entropy and all other density dependent thermodynamic properties. These low temperature, force-stabilized states are identified as glass states.

This physical insight offered by the QCSW model appears to be widely applicable to liquids with short-range attractive forces. Extensions to longer chains and direct application of the model are discussed in Chapter 8.

Chapter 8: Extension and Application of QCSW Model to Polymers

8.1 Introduction

Chapter 7 presented the QCSW model in terms of an unchained SW fluid, but glass formation occurs in a wide variety of molecular and polymeric liquids. The QCSW phenomenon of configurational energy at high densities may be extended to molecules of all sizes in general. This new mechanism of energy saturation does not vitiate the prevailing dogma that the number of ways that molecules can randomly pack into a disordered array reaches a limiting value with decreasing temperature which defines the ideal glass[142,160–163]. A HS fluid without attractive interactions exhibits a putative glass transition[151] near the "random loose packing" limit of about 0.55[164]. This "packing mechanism" of glass formation is still expected to control for liquids with high glass transition temperatures T_g for which the QCSW model does not predict the polymer has yet reached energy saturation, but when parameters are fit to polymer melts, many do appear to reach an energy saturation limit at the measured value of T_g.

8.2 QCSW Extension to Chains

Figure 8.1 shows a two-dimensional schematic of a segment of a QCSW chain. The gray annuli are the attractive domains of the two black spheres with λ set to 3/2. Each attractive shell has a volume $V_S = 8(\lambda^3 - 1)(\pi/6)\sigma^3 = 19v_0$ in which $v_0 = (\pi/6)\sigma^3$ for $(\lambda = 3/2)$. The white annuli around the black spheres are the excluded volume regions where no other sphere center may enter. The red sphere centers lie within the attractive domains of the black spheres, and one red sphere lies in both domains. These red spheres might belong to other chains or to the same chain. The two blue spheres directly connected to the black spheres do not contribute to the attractive interaction. Because neighboring spheres along a chain do not contribute to the attractive

domain, but do reduce the available space around a central sphere, the $n_{\max}$ of Chapter 7 must be reduced by two, and the maximum number of spheres that can be accommodated in an attractive domain of a chained sphere is here set at $n_{\max} = 10$. $n_{\max}$ now functions as an effective coordination number per monomer. The nearest-neighbor connected spheres still contribute to the local packing density; therefore $\eta_{\max}$ retains the value $\eta_{\max} = 12/19 = 0.63$, which corresponds to the random close-packing value for hard spheres[148,164].

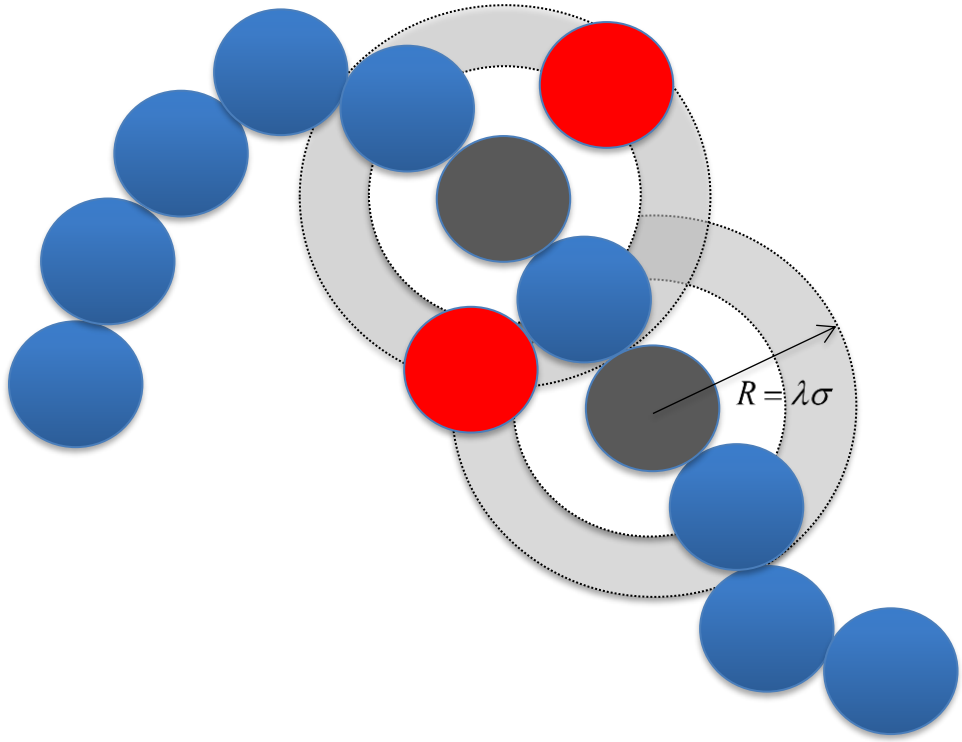

Figure 8.1: Two-dimensional schematic of a tangent sphere chain

A QCSW chains is modeled a tangent sphere chain of r HS monomers attractively interacting with other monomers through SW potentials. The maximum

possible interaction energy/chain is $-rn_{\max}\varepsilon$. This may involve both intermolecular interactions from spheres on different chains and intramolecular monomer-monomer interactions from non-neighbor spheres on the same chain. The probability $\mathbf{P}_n$ that n spheres are within the attraction domain of a single, given monomer is given by the binomial distribution of equation (7.4). The assumed average attraction felt by a monomer is $-\langle n\rangle\varepsilon$, where $\langle n\rangle$ is the average number of non-bonded spheres within its attractive domain given by equation (7.5). Assuming statistical independence of each sphere in the chain, the average energy of the r-mer chain is $-r\langle n\rangle\varepsilon$.

The volume fraction of space occupied by the spheres in the attraction shell of a given sphere η_S (which includes the two bonding neighbors) is given by:

$$\eta_S = \frac{(\langle n\rangle + 2)v_0}{V_S} = \eta_{\max}\frac{\theta e^{\beta\varepsilon}}{1+\theta(e^{\beta\varepsilon}-1)} \tag{8.1}$$

where again $\theta = \eta/\eta_{\max}$. All approximations stated in Chapter 7 for solving for the quasi-chemical parameter z and the local occupied volume fraction η_S are retained here. The insertion factor for a QCSW chain is given by:

$$\ln \mathbf{B} = \ln \mathbf{P}_{ins} - r\ln\langle\exp[-\beta\varepsilon n]\rangle \tag{8.2}$$

$\mathbf{P}_{ins}$ is approximated with the SPT single sphere insertion probability[10], and the means of extending the insertion probability to chains given by equation (2.5), and $\langle\exp[-\beta\varepsilon n]\rangle$ is given by (7.16). Through isothermal integration of the Gibbs-Duhem equation, the QCSW chain equation of state is given as:

$$\frac{Z}{r}=\frac{Pv_0}{\eta kT}=\frac{1}{r}+\left[\frac{1+\eta+\eta^2}{(1-\eta)^3}-1\right]-n_{\max}\left[1-\frac{\ln\left[1+\theta\left(e^{\beta\varepsilon}-1\right)\right]}{\theta(e^{\beta\varepsilon}-1)}\right] \tag{8.3}$$

The SPT equation is recovered as attractive shell approaches ∞ while $n_{\max}\varepsilon$ is held constant:

$$\lim_{\substack{n_{\max}\to\infty\\ \varepsilon\to 0\\ n_{\max}\varepsilon=\text{const.}}} \frac{Pv_0}{\eta kT}=\frac{1}{r}-1+\frac{1+\eta+\eta^2}{(1-\eta)^3}-\eta\frac{n_{\max}\varepsilon}{2kT\eta_{\max}} \tag{8.4}$$

in which the SPT T^* is given in relation to the QCSW ε/k by equation (7.30). The potential energy contribution to the EOS in the VDW limit diverges as $1/T$ while in the QCSW chain equation it reaches an asymptotic limit.

The occupied volume fraction for the QCSW chain EOS in equation (8.3) and the VDW limit of (8.4) are plotted in Figure 8.2 for $n_{\max}=10$, $\lambda=3/2$j, and $r\to\infty$ along the $Z\simeq 0$ isobar. The intercepts for the QCSW linear density/temperature extrapolation are $\eta=0.515$ at zero temperature and $kT/\varepsilon=2.124$ at zero density.

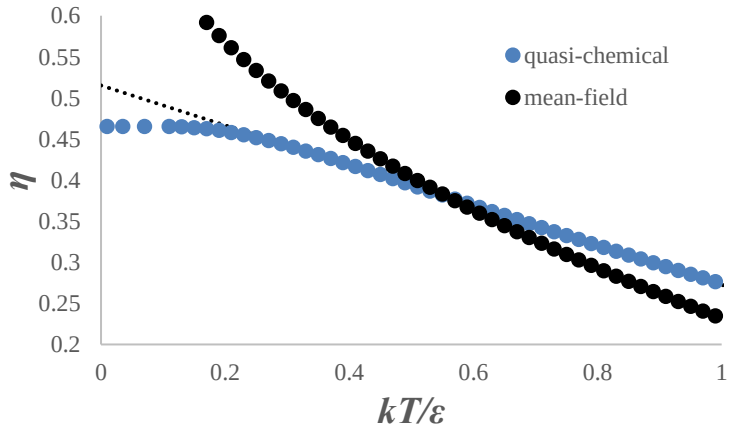

Figure 8.2: Comparison of density predictions of the QC and mean field (VDW type) equations of state.

In Figure 8.2, as $T \to 0$, the QCSW predicts $\eta \to 0.465$, while the mean-field (VDW) model predicts $\eta \to 1$ as $T \to 0$ (a physically unrealistic limit for the occupied volume fraction). The QC approximation also yields a linear density/temperature relationship over a large temperature range in agreement with the observations in Chapters 5 and 6.

The saturated liquid approaches energy saturation along the plateau region of the density/temperature curve defined by $\beta\varepsilon \to \infty$ where the equation of state in the NLR for the infinitely long chain is given by:

$$\frac{1 + \eta_g + \eta_g^2}{\left(1 - \eta_g\right)^3} - (1 + n_{\max}) = 0 \tag{8.5}$$

(8.5) defines the ideal glass density η_g. η_g is a function of $n_{\max}$ only, and for $n_{\max} = 10$, $\eta_g = 0.465$.

Equations (7.33–36) may be used to calculate the excess entropy per monomer of the QCSW chain relative to an ideal gas at the same density and temperature. In the low temperature limit, the excess entropy per monomer is given by:

$$\begin{aligned} \lim_{\beta\varepsilon\to\infty} S^E/k &= \ln \mathbf{P}_1 + n_{\max} \ln \theta \\ &= -17.4 \quad \text{at} \quad \eta = 0.465 \end{aligned} \tag{8.6}$$

where $\mathbf{P}_1$ is the insertion probability of the single unchained HS. The excess entropy per monomer as a function of temperature is plotted in Figure 8.3.

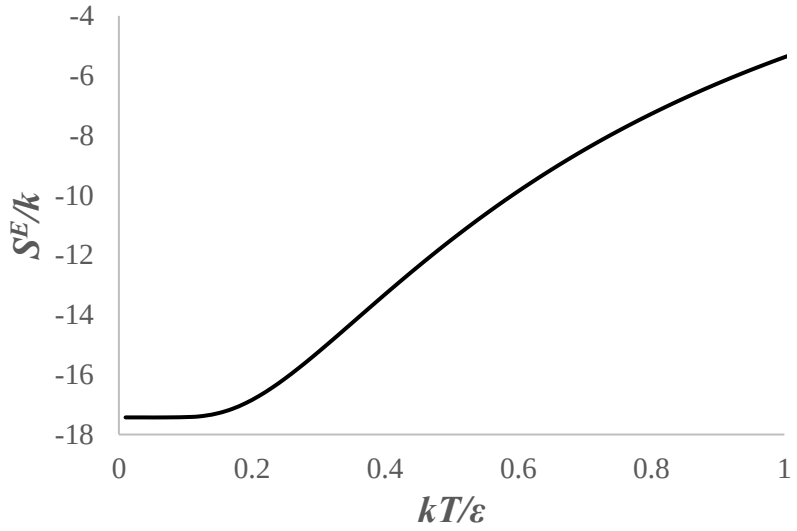

Figure 8.3: Plot of excess entropy per monomer against reduced temperature

This excess entropy asymptotes at low temperatures to a fixed value, $S^E/k = -17.4$. The QC model avoids the "Kauzmann entropy catastrophe"[161]. This limiting entropy property of the QC model is a direct consequence of configurational energy saturation. This view of the glass transition differs from the idea that the ideal thermodynamic liquid-to-glass transition occurs when the configurational entropy reaches zero (or a constant) via a second order phase transition[142], the packing saturation method mentioned in 8.1. Like the QCSW the configurational entropy of this packing mechanism method reaches a limiting value, but the cause and effect relationship is different.

Increasing density through any constraint causes $\langle n \rangle / n_{\max}$ to approach unity. Chapter 7 did not discuss the effects of pressure on potential energy saturation and glass formation. The application of pressure increases the probability of attractive interactions, which promotes energy saturation at a higher temperature, and the observed glass temperature T_g should increase at elevated pressures. Crosslinking a polymer and increasing its molecular weight all increase the polymer density and should promote

energy saturation at higher temperatures. These predictions are in qualitative accord with experimental observations.

8.3 Density/Temperature Linearity and QCSW Parameters

Though the equation of state clearly does not functionally obey a linear density/temperature relationship, Figure 8.2 shows that the QCSW chain density is linear over a substantial temperature range. The equation of the linear region of Figure 8.2 for QCSW with $n_{\max} = 10$, $r \to \infty$ along $Z \simeq 0$ may be written as:

$$\frac{\eta}{0.515} + \frac{kT}{2.124\varepsilon} = 1 \tag{8.7}$$

η is proportional to the mass density by $\eta = \rho r v_0 / M$ in which M is the molecular weight. From the regressed linear density/temperature intercepts (ρ_P^*, T_P^*), the parameters rv_0/M and ε/k may be calculated. Values of ε/k and the corresponding ρ_P^* for some polymers are given in Table 8.1. These values were fit with empirical expressions of low pressure mass intensive volume given by Rodgers[49]. Rodgers carefully ensured that the temperature ranges applied to polymer melts only; therefore, parameters in Table 8.1 are not biased by experimental T_g values. Figure 8.4 plots some of the density/temperature data against the QCSW $Z, P \simeq 0$ isobar. Most glass temperatures in Table 8.1 were retrieved from the Polymer Properties Database:

http://polymerdatabase.com/polymer%20physics/Polymer%20Tg.html

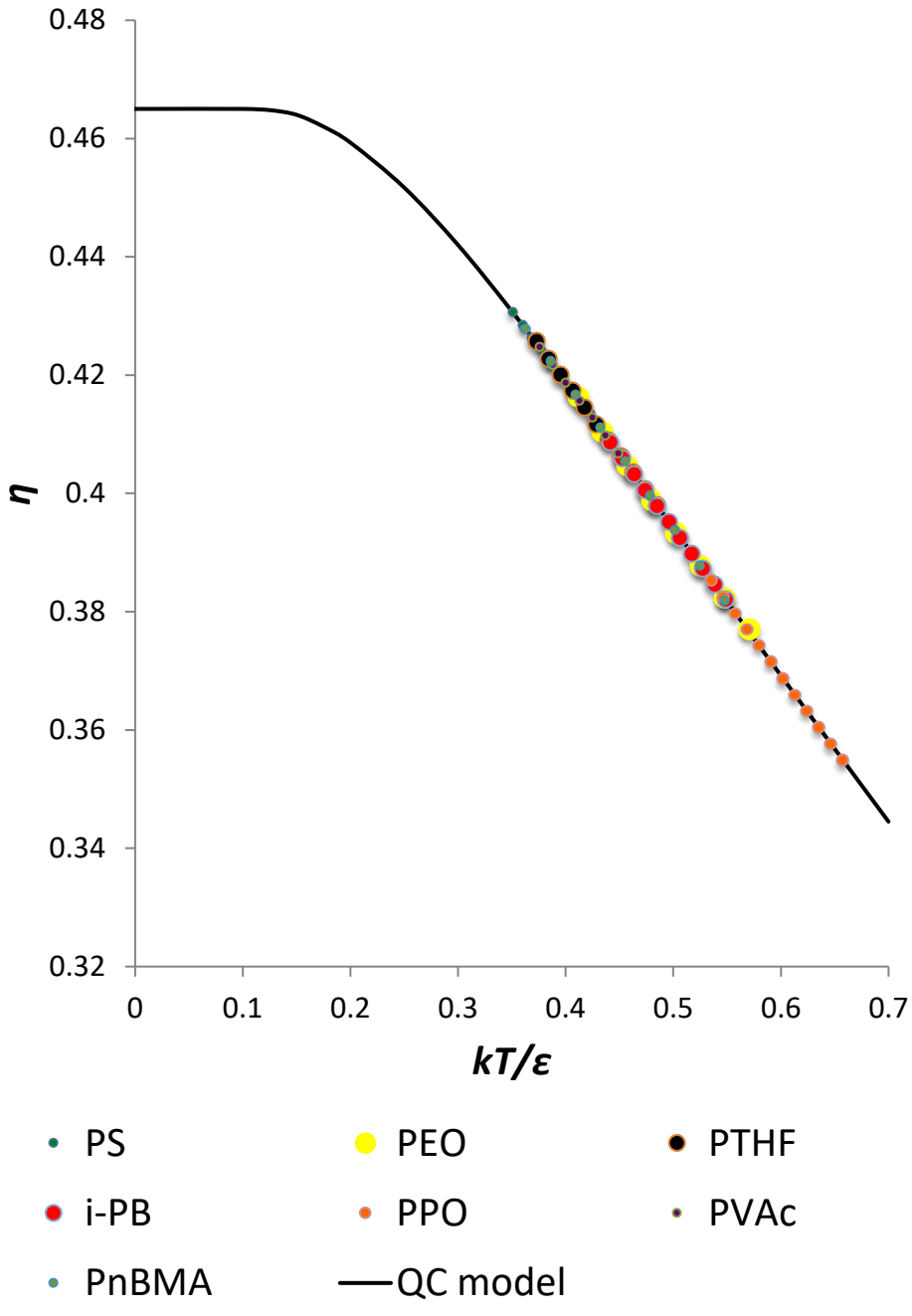

Figure 8.4: Polymer density data at low pressure fit to the QCSW model

Polymer	Poly-	T_g (K)	ε/k (K)	ρ_P^* (g/cm^3)	ρ_g (g/cm^3)	$\frac{\langle n \rangle_g}{n_{\max}}$
PPO	p-phenylene oxide	487	902.1	1.367	1.02	0.908
TMPC	tetramethyl bisphenol-A PC	467	942.8	1.358	1.04	0.926
PEEK	ether ether ketone	421	1025	1.555	1.25	0.956
PC	carbonate	418	1011	1.442	1.16	0.955
PAr	arylate	385	1114	1.442	1.21	0.975
PCHMA	cyclohexyl methacrylate	382	980	1.316	1.07	0.962
PMMA	methyl methacrylate	378	1025	1.403	1.16	0.969
PH	phenoxy	363	996	1.381	1.14	0.970
PET	ethylene terephthalate	343	987.7	1.596	1.33	0.974
PEMA	ethyl methacrylate	336	842.2	1.362	1.1	0.959
PVAc	vinyl acetate	305	819.3	1.42	1.17	0.968
PnBMA	n-butyl methacrylate	293	863	1.262	1.06	0.976
PMA	methyl acrylate	283	886.6	1.396	1.18	0.981
PEA	ethyl acrylate	250	846.9	1.343	1.15	0.986
PVME	vinyl methyl ether	245	890.6	1.219	1.05	0.989
PEO	ethylene oxide	215	881.8	1.328	1.16	0.993
PCL	caprolactone	207	932.2	1.279	1.13	0.996
PTHF	tetrahydrofuran	187	893	1.161	1.03	0.997
PoMS	ortho methylstyrene	409	1094	1.203	0.989	0.967
PS	styrene	373	1106	1.206	1.022	0.977
a-PP	propylene(atactic)	253	802.1	1.045	0.888	0.982
i-PB	1-butene (isotactic)	244	934.3	1.007	0.877	0.991
PIB	isobutylene	203	972.1	1.074	0.952	0.997
LPE	ethylene (linear)	193	831.7	1.033	0.909	0.995
PBD	cis-1,4 butadiene	170	831	1.081	0.959	0.997

Table 8.1: Fit QCSW ε/k and glass properties for some polymers

8.4 THERMODYNAMIC GLASS TRANSITION MECHANISM

The QC model is based on hard sphere packing with maximum random close packing of 12/19 = 0.632. Mixtures of differently sized spheres, and ellipsoid objects can randomly pack to higher densities[165]. In a real polymer, the structure of the chain backbone and pendant side groups dictate chain stiffness and molecular packing. The QC

model does not explicitly incorporate chain stiffness, nor does it consider packing objects of different sizes and shapes.

In Figure 8.5, η_g (the occupied volume fraction at T_g) are plotted against reciprocal temperature (ε/kT_g) for the polymers in Table 8.1. Excluding PPO and TMPC, the average is $\eta_g = 0.44 \pm 0.02$. Table 8.1 contains values of $\langle n \rangle / n_{\max}$ at T_g which may be considered the fraction of energy saturation reached. At $\eta_g = 0.44$ along $Z \simeq 0$, $\langle n \rangle / n_{\max} > 98\%$.

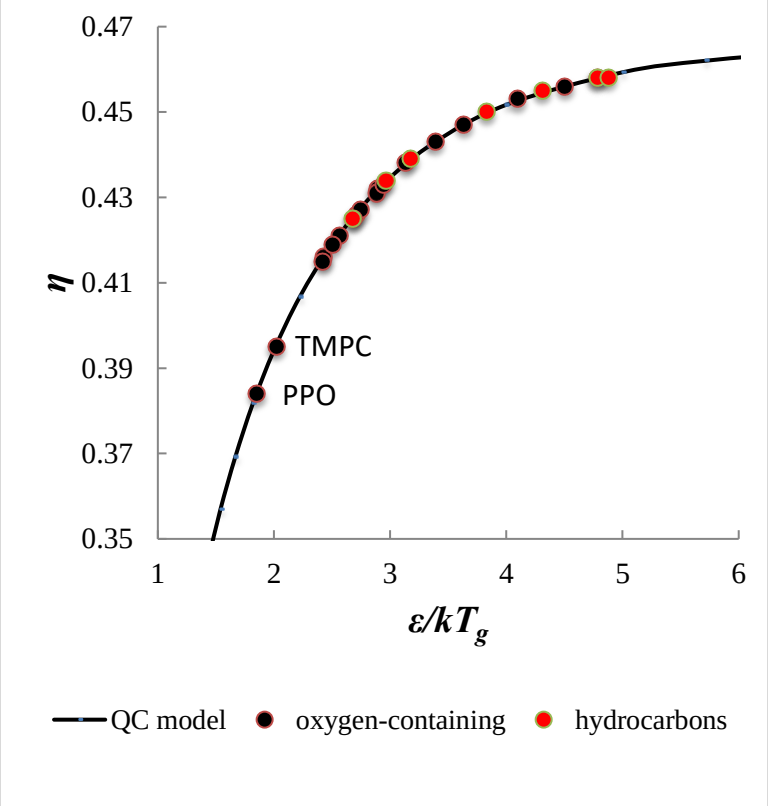

Figure 8.5: Plot of the occupied volume fraction at T_g versus reciprocal temperature for the polymers listed in Table 8.1

Although not absolutely conclusive or rigorous, this QCSW analysis suggests energy saturation, and not packing saturation, is controlling glass formation, with PPO

and TMPC as exceptions. For PPO, $\varepsilon/kT_g = 1.85$, and $\langle n\rangle/n_{\max} = 0.908$. If energy saturation were controlling, $\langle n\rangle/n_{\max}$ would be closer to unity. The QC model can accommodate inefficient packing by adjusting $\eta_{\max}$ or $n_{\max}$. Reduction of $\eta_{\max}$ signifies less efficient packing around a monomer. With a maximum number of monomers allowed within the attraction zone set to $n_{\max} = 10$, a fixed $\lambda = 3/2$, and two neighboring monomers contributing to the local density, $\eta_{\max} = 12/19 = 0.632$. If inefficient packing limits the coordination number to 8, then the maximum packing fraction around any monomer becomes 10/19. For PPO, lowering $n_{\max}$ to 8 increases the $\langle n\rangle/n_{\max}$ from 90% to 93%, insufficient to infer energy saturation.

8.5 THERMODYNAMICS, KINETICS, AND FRAGILITY

Experimentally observed glass transitions are kinetic phenomena. Computer simulations on various model systems support the idea of a direct connection between dynamics and excess entropy. This connection has been invoked for simple fluids[166,167] as well as for polymers[168]. Fragile polymers are kinetically characterized as those whose temperature dependent dynamics near T_g deviate substantially from Arrhenius behavior[169]. In general, polymers with rigid or sterically hindered backbones exhibit the greatest fragility and have high T_gs[170,171]; however, fragility does not always scale with T_g and other structural factors such as inflexible/flexible pendant groups to explain deviations[172] have been invoked[173].

Among 14 polymers for which fragility indices have been measured, a decent correlation between fragility and saturation degree is observed and plotted in Figure 8.6. This trend is more apparent in Figure 8.7 where T_g is plotted against η_g. All polymers included in Figure 8.7 have reached at least 95% saturation as determined by $\langle n\rangle/n_{\max}$. Like PPO and TMPC, PTFE glass may have reached packing saturation. In Figure 8.6,

the solid blue circles are fragility indices from Qin & McKenna[171]. Black circles use WLF constants calculated at T_g from Berry-Fox[174] using $m = C_1 T_g / C_2$.

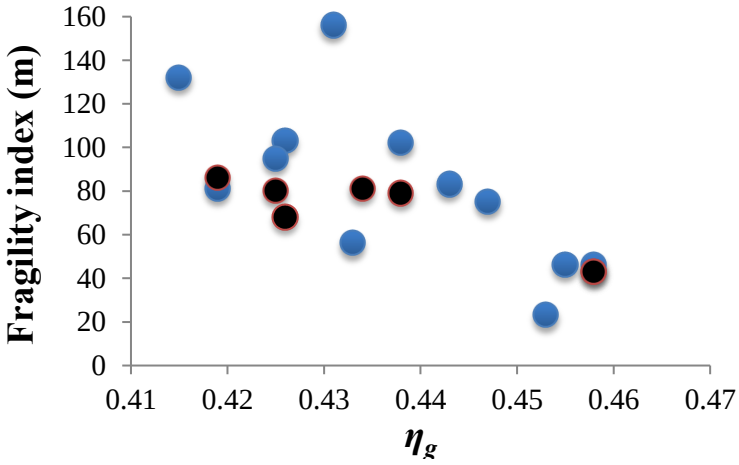

Figure 8.6: Plot of fragility index (m) against occupied volume fraction (η_g) at T_g that illustrates that fragility decreases with increasing saturation

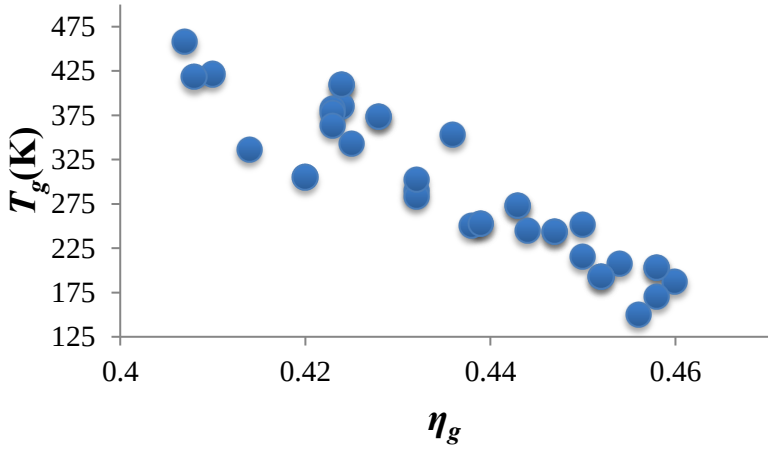

Figure 8.7: Plot illustrates that low T_g polymers saturate more completely (complete saturation at $\eta_g = 0.465$)

8.6 SUMMARY AND CONCLUSIONS

Treating the monomer-monomer energetics of a tangent sphere chain model as a square well potential in a quasi-chemical approximation yields configurational energy saturation prior to reaching zero temperature. Energy saturation is 99.7% complete at $kT/\varepsilon = 0.2$. Among the polymers in Tables 8.1, all but PPO and TMPC appear near energy saturation at their reported T_gs. Incomplete saturation of PPO and TMPC (90.8 and 92.6%, respectively) may indicate inefficient molecular packing with a "packing saturation limit" interrupting energy saturation. Low T_g polymers systematically saturate more completely than high T_g polymers. Average saturation reaches 98% for the tabulated polymers at an average occupied volume fraction of $\eta = 0.44 \pm 0.02$. Calculated occupied volume fractions at T_g, a measure of saturation degree, correlate with polymer fragility. Fragile polymers tend to be less saturated. In Figure 8.7, correlation of T_g with saturation is demonstrated with a broad polymer set Excess entropy per monomer (S^E/k) relative to an ideal gas at the same temperature and density asymptotes at low temperatures to a value of -17.4 per monomer. This limiting entropy property is a direct consequence of energy saturation, but does not deny "packing saturation" as a glass formation mechanism.

The QCSW model uses a more physically realistic potential energy than the SPT model introduced in Chapter 2, yet it is still easily implemented and analyzed. Only a few implications and applications of the model were discussed. The QCSW model, or even the concept of configurational energy saturation independent of the model, has the potential to describe properties of liquids in general.

Appendix A: SPT Equation of State Parameters*

In the SPT model, like the LF model, a pure fluid is completely determined by three parameters. For small molecule fluids, these parameters can be estimated from known saturation and vaporization properties at a corresponding temperature. Details of implementation are given in Appendix A of reference [19] for the LF model and the same procedure can be adopted for SPT model.

Since $\Delta S_{vap}/R = \Delta H_{vap}/RT$, equation (2.23) may be rearranged for a liquid in equilibrium with its vapor to solve for r:

$$r = \frac{\Delta H_{vap}/RT - \ln\left(\eta_{liq}/\eta_{vap}\right)}{\ln\left(\frac{1+y_{liq}}{1+y_{vap}}\right) + 3\left(y_{liq} - y_{vap}\right) + \frac{3}{2}\left(y_{liq}^2 - y_{vap}^2\right)} \tag{A1}$$

in which Experimental mass density at saturation $\rho_{liq,vap}$ may be converted to the occupied volume fraction $\eta_{liq,vap}$, by:

$$\eta_{liq,vap} \equiv \frac{rv^*}{V} = \frac{rv^*}{M}\rho_{liq,vap} \equiv \frac{\rho_{liq,vap}}{\rho^*} \tag{A2}$$

where ρ^* for the SPT model is here defined as the ratio of the mass of a given molecule to the HS volume the molecule occupies. Since thermal contributions to ΔE_{vap} cancel, equation (2.21) may be rearranged to give:

$$T^* = \frac{\Delta E_{vap}}{rR\left(\eta_{liq} - \eta_{vap}\right)} \tag{A3}$$

The SPT chain EOS for a pure liquid is given by:

$$\eta_{liq}^2 + \tilde{P}_{\text{sat}} - \eta_{liq}\tilde{T}\left[\frac{1}{r} + 4y_{liq} + 6y_{liq}^2 + 3y_{liq}^3\right] = 0 \tag{A4}$$

* This material was partly published as Appendix A in: Sean P. O'Keefe, and Isaac C. Sanchez, "Scaled Particle Theory of solutions: Comparison with Lattice Fluid model" *Fluid Phase Equilibria* 433, 67 (2017)[16]. Sean Patrick O'Keefe is the primary author.

With knowledge of $\Delta H_{vap}, \Delta E_{vap}, \rho_{liq}, \rho_{vap},$ and P_{sat} for a given temperature, with identity (A2), equations (A1), (A3), and (A.4) form a system of three equations of three independent variables (r, v^*, T^*). All other pure component parameters may be derived from these.

Equation of state parameters for 80 fluids calculated in this manner are tabulated in Table A1. With the exception of carbon dioxide, these parameters were chosen such that saturated pressure was near atmospheric. For CO_2, pressure was increased to 6 bar to ensure liquid/vapor equilibrium. As this is a single point fit, differences in calculated properties from measured values at the temperature and pressure at which the fit was performed are identically zero.

Fluid	T^*(K)	P^* (MPa)	ρ^*(g/cm^3)	v^*(cc/mol)	r
methane	2160	1110	1.01	16.18	0.979
ethane	2623	1832	1.59	11.90	1.623
propane	3477	1662	1.59	17.39	1.600
n-butane	3862	1682	1.71	19.09	1.790
n-pentane	4097	1739	1.81	19.59	2.035
n-hexane	4291	1772	1.89	20.13	2.263
n-heptane	4437	1815	1.97	20.33	2.505
n-octane	4521	1884	2.04	19.95	2.800
n-nonane	4653	1888	2.09	20.49	2.993
n-decane	4747	1906	2.14	20.70	3.216
n-undecane	4911	1773	2.05	23.03	3.315
n-dodecane	4893	1950	2.22	20.86	3.671
n-tridecane	5205	1802	2.22	24.01	3.455
n-tetradecane	4926	2179	2.38	18.80	4.435
n-pentadecane	5358	1768	2.25	25.19	3.747
isobutane	3693	1593	1.70	19.27	1.776
2-methylbutane	4090	1586	1.75	21.45	1.917
neopentane	3836	1462	1.75	21.81	1.886

Table A1: SPT equation of state parameters for small molecules

Fluid	T^*(K)	P^* (MPa)	ρ^*(g/cm^3)	v^*(cc/mol)	r
2-methylpentane	4237	1678	1.87	20.99	2.190
2,2-dimethylbutane	4370	1532	1.90	23.72	1.910
2,3-dimethylbutane	4363	1591	1.87	22.80	2.022
ethylene	2819	1636	1.46	14.33	1.339
propene	3444	1766	1.65	16.22	1.576
1-butene	3840	1749	1.76	18.26	1.749
trans-2-butene	3947	1806	1.76	18.17	1.757
cis-2-butene	3947	1911	1.81	17.17	1.809
1,3-butadiene	3969	1809	1.76	18.24	1.686
isoprene	4285	1873	1.91	19.02	1.876
propyne	3892	2361	1.86	13.71	1.567
cyclopentane	4643	1929	1.96	20.01	1.787
cyclohexane	4866	1929	2.07	20.98	1.938
cycloheptane	5253	1920	2.13	22.75	2.029
cyclooctane	5505	1923	2.19	23.81	2.157
cyclohexene	5924	1528	1.89	32.23	1.349
benzene	5012	2254	2.23	18.49	1.893
toluene	5236	2143	2.25	20.32	2.016
ethylbenzene	5323	2094	2.28	21.13	2.199
p-xylene	5307	2107	2.27	20.94	2.236
m-xylene	5284	2156	2.29	20.38	2.272
o-xylene	5455	2148	2.30	21.11	2.189
styrene	5614	2254	2.40	20.71	2.098
chloromethane	4033	2675	2.63	12.53	1.534
dichloromethane	4639	2917	3.53	13.22	1.822
chloroform	4911	2384	3.89	17.12	1.791
carbon tetrachloride	5142	1972	4.10	21.68	1.732
1-chlorobutane	4729	2099	2.40	18.74	2.062
1,1 dichloroethane	4623	2398	3.17	16.03	1.949
1,2 dichloroethane	5098	2662	3.24	15.93	1.917
1,1,1 trichloroethane	4852	2051	3.54	19.67	1.913
1,1 dichloroethylene	4564	2175	3.27	17.45	1.702
trans-1,2-dichloroethylene	4761	2371	3.31	16.69	1.756
cis-1,2-dichloroethylene	4971	2491	3.33	16.59	1.752
trichloroethylene	5193	2264	3.76	19.08	1.834

Table A1 cont.

Fluid	T^*(K)	P^* (MPa)	ρ^*(g/cm^3)	v^*(cc/mol)	r
fluorobenzene	4986	2277	2.69	18.21	1.959
chlorobenzene	5637	2287	2.80	20.50	1.961
bromobenzene	5984	2307	3.72	21.56	1.959
perfluorobutane	3020	1628	5.40	15.43	2.855
perfluoroheptane	3537	1611	5.85	18.26	3.632
perfluorooctane	3655	1684	6.21	18.05	3.906
acetone	4800	2628	2.07	15.19	1.845
2-butanone	4807	2457	2.14	16.27	2.068
diethyl ether	4048	2005	2.07	16.79	2.133
tetrahydrofuran	4929	2415	2.32	16.97	1.831
1,4 -Dioxane	5054	2801	2.73	15.00	2.152
ethyl formate	4297	2770	2.54	12.9	2.266
methyl acetate	4373	2851	2.60	12.75	2.235
ethyl acetate	4367	2604	2.55	13.94	2.478
propyl acetate	4494	2431	2.52	15.37	2.638
butyl acetate	4639	2291	2.47	16.83	2.790
aniline	5910	3313	2.61	14.83	2.407
2,6-dimethylpyridine	5214	2435	2.47	17.80	2.438
phenol	5644	4164	3.12	11.27	2.675
carbon dioxide	2657	3839	3.79	5.76	2.018
carbon disulfide	5693	2401	2.54	19.71	1.278
nitrogen	1329	937	2.06	11.8	1.154
oxygen	1696	1281	2.76	11.01	1.052
argon	1699	1157	3.35	12.21	0.976
krypton	2407	1277	5.67	15.67	0.943
xenon	3296	1407	6.96	19.47	0.969
carbon monoxide	1362	1018	2.04	11.12	1.232

Table A1 cont.

For polymers of high molecular weight, $r \to \infty$,$1/r \to 0$, and the equation of state reduces to a simple form:

$$\eta^2 + \tilde{P} - \eta\tilde{T}[4y + 6y^2 + 3y^3] = 0 \qquad \text{(A5)}$$

and satisfies a corresponding states principle, a property that is well established for polymers[82]. The characteristic T^*, P^*, and ρ^* for several polymeric fluids shown in Table A2 were obtained using a least squares fitting of equation (A5) to the empirical Modified Tait equation:

$$\frac{V}{V_0(T)} = 1 - C \ln\left(1 + \frac{1}{C}\frac{P}{B_0(T)}\right) \tag{A6}$$

with C set to Cutler's constant of 0.0894. Functional forms of $V_0(T)$ and $B_0(T)$ were taken from reference [82]. Details on the ranges of applicability and references to the data used to fit $B_0(T)$ and $V_0(T)$ for the polymer liquids is given in reference [49].

For each polymer, temperature ranges over which SPT parameters were fit correspond to those given by Rodgers[49], who carefully selected conditions that avoid glass formation or crystallization. Pressures ranged from 0.1 to 1 MPa for the same reason. Considering (A5) can analytically be solved for temperature, and liquid densities are more sensitive to changes in temperature than to changes in pressure, parameters were fit to minimize differences in measured and calculated temperature. Table A2 contains the average absolute percent error (AAPE) between the SPT calculated temperature for a given intensive volume, and a temperature which yields the same intensive volume by equation (A6) at that specified pressure.

Poly-	T^* (K)	P^* (MPa)	ρ^* (g/cm^3)	v^* (cm^3/mol)	AAPE (%)
dimethyl siloxane	10860	736	1.75	123	0.028
styrene	22860	833	1.63	228	0.065
o-methyl styrene	21140	959	1.63	183	0.034
methyl methacrylate	20010	1232	1.90	135	0.088
n-butyl methacrylate	14260	755	1.78	157	0.748
cyclohexyl methacrylate	16720	1066	1.84	130	0.097
ethyl acrylate	13780	977	1.90	117	0.324
ethyl methacrylate	12950	1501	1.97	72	0.021
methyl acrylate	15080	1088	1.95	115	0.372
vinyl acetate	15210	1211	1.97	104	0.085
ethylene (linear)	11780	1211	1.89	81	0.023
ethylene (branched)	12950	1070	1.81	101	0.042
butadiene	19070	892	1.41	178	0.062
1-butene	14200	826	1.46	143	0.086
arylate	17910	1118	2.05	133	0.266
caprolactone	16690	964	1.77	144	0.026
carbonate	14660	1133	2.12	108	0.506
bisphenol chloral PC	15420	1346	2.46	95	0.333
hexafluoro bisphenol-A PC	11370	1367	2.87	69	0.078
tetramethyl bisphenol-A PC	12920	1348	2.04	80	0.053
ethylene terephthalate	13010	2031	2.43	53	0.012
isobutylene	22200	753	1.41	245	0.054
propylene (isotactic)	13220	787	1.47	140	0.015
propylene (atactic)	12690	780	1.50	135	0.228
Phenoxy	16150	933	1.96	144	1.066
sulfone	16040	1699	2.18	78	0.293
ethylene oxide	15130	1200	1.86	105	0.047
ether ether ketone	12900	1957	2.41	55	0.005
tetrahydrofuran	15750	882	1.61	148	0.128
4-methyl-1-pentene	12750	601	1.49	176	0.357
amide 6	22750	896	2.01	211	0.021
epichlorohydrin	20260	929	2.13	181	0.092
vinyl chloride	20220	853	2.21	197	0.220
phenylene oxide	11760	1327	2.09	74	0.162

Table A2: SPT Equation of state parameters for polymeric liquids

Only an interaction parameter P_{12}^* (or equivalently, $\Delta P_{12}^* = P_1^* + P_2^* - 2P_{12}^*$) is required to characterize a binary mixture. All other parameters either are pure component parameters as given in Tables A1 and A2 or can be directly derived from pure component parameters. Often with nonpolar mixtures, as with the calculations in Section 3.3, a geometric mean is assumed for P_{12}^*:

$$P_{12}^* = \sqrt{P_1^* P_2^*} \tag{A7}$$

in which case the mixture properties are completely determined by pure component equation of state parameters and:

$$\Delta P_{12}^* = \left[\sqrt{P_1^*} - \sqrt{P_2^*}\right]^2 \tag{A8}$$

In practice, calculations using the geometric mean often yield unsatisfactory results and adjustment of the interaction parameter is required. It is convenient to define a dimensionless parameter ζ_{12} which indicates the extent to which P_{12}^* deviates from the geometric mean:

$$\zeta_{12} = P_{12}^* / \sqrt{P_1^* P_2^*} \tag{A9}$$

ζ_{12} may be obtained from any mixture thermodynamic property such as a heat of mixing or a mixture's upper critical solution temperature. Table A3 lists values of ζ_{12} used in calculations for some of the binary mixtures discussed in Chapter 3 and the type of experimental data used to obtain ζ_{12}. The table also gives recalculated ζ_{12} for the LF model for these mixtures. In reference [18], ζ_{12} was originally calculated as $\zeta_{12} = \varepsilon_{12}^* / \sqrt{\varepsilon_1^* \varepsilon_2^*}$, but in order to make equivalent comparisons to the SPT model, ζ_{12} values for the LF model in Table A3 were recalculated using equation (A9).

Mixture	SPT	LF	Data type
methane/n-butane	0.93390	0.97720	Boiling point
benzene/cyclohexane	0.96986	0.96340	Heat of mixing
benzene/n-heptane	0.97120	0.97220	Heat of mixing
cyclohexane/n-heptane	0.99080	0.99327	Heat of mixing
aniline/n-butane	0.99396	0.98641	UCST
aniline/n-pentane	0.98837	0.99147	UCST
aniline/n-hexane	0.98498	0.99860	UCST
aniline/n-heptane	0.98181	0.99574	UCST
aniline/cyclohexane	0.97421	0.97013	UCST
acetone/carbon disulfide	0.93740	0.93413	UCST
acetone/n-hexane	0.96183	0.97799	UCST
acetone/cyclohexane	0.94453	0.94892	UCST
n-perfluorooctane/ n-octane	0.92486	0.92975	liquid/liquid solubility
2,6-Dimethylpyridine/ phenol	1.11535	1.14239	azeotrope temperature

Table A3: Interaction pressure scale parameter parameter ζ_{12} for various binary mixtures

Appendix B: Line Parameters for Liquids at Low Pressure

Table B1 contains low pressure regressed intercepts (T^*, ρ^*) and coefficients of determination (R^2) fit to the line:

$$\frac{\rho}{\rho_P^*} + \frac{T}{T_P^*} = 1 \tag{B1}$$

for 140+ small molecule liquids and polymer melts. Temperature ranges of fits are described in Chapter 6. Data for small (non-polymer) liquids were obtained from models[95,97,98] through the NIST/TRC Web Thermo Tables (WTT) http://wtt-pro.nist.gov/wtt-pro/. Data for polymer melts were obtained directly from the references cited in the table. An asterisk indicates saturated liquid data were used and not isobaric density data at 1bar.

Liquid	ρ^*(kg/m^3)	T^*(K)	R^2	Model/ Data source
argon	1930	315.0	1.0000	[95]
krypton	3327	437.5	1.0000	[95]
xenon	4040	609	0.999	[95]
oxygen	1558	338.5	0.9996	[95]
nitrogen	1140	265	1.000	[95]
carbon monoxide	1135	271	1.000	[95]
hydrogen sulfide	1310	768	1.000	[95]
carbon disulfide*	1690	1160	1.000	[97]
methane	578	416	1.000	[95]
ethane	755.4	663.5	0.9997	[95]
propane	822.4	793.6	0.9998	[95]
n-butane	866	901	1.000	[95]
n-pentane	893	981	1.000	[95]
n-hexane	922	1030	1.000	[95]
n-heptane	931	1100	1.000	[95]
n-octane	942	1150	1.000	[95]
n-nonane	955	1180	1.000	[95]

Table B1: Regressed line parameters for liquids at low pressure

Liquid	ρ^*(kg/m^3)	T^*(K)	R^2	Model/ Data source
n-decane	965	1210	1.000	[95]
n-undecane*	971	1240	0.999	[97]
n-dodecane	978	1260	0.999	[95]
n-tridecane	981	1290	0.999	[98]
n-tetradecane*	970	1380	0.999	[97]
n-pentadecane*	992	1310	0.999	[97]
n-hexadecane*	995	1330	0.999	[97]
n-heptadecane	999	1350	0.998	[98]
isobutane	852.9	870.2	0.9996	[95]
isopentane	892.4	964.3	0.9999	[95]
neopentane	891	870	1.000	[95]
2,3-dimethylbutane*	903	1090	0.999	[97]
2-methylpentane	912	1030	1.000	[95]
3-methylpentane*	934	1010	1.000	[97]
2,2-dimethylpentane*	924	1080	1.000	[97]
2,3-dimethylpentane*	942	1110	1.000	[97]
isooctane	935.5	1123	0.9998	[98]
2-2-dimethylhexane*	946	1100	1.000	[97]
2,5-dimethylhexane*	935	1130	0.999	[97]
ethene	793.7	597.2	0.9997	[95]
propene	868	763	1.000	[95]
1-butene	911	855	1.000	[95]
trans-2-butene	911	882	1.000	[95]
cis-2-butene	930	892	1.000	[95]
1,3-butadiene*	944	867	1.000	[97]
isoprene*	959	999	0.994	[97]
cyclopentane	1020	1100	1.000	[95]
cyclohexane	1060	1100	1.000	[95]
methylcyclohexane	1020	1180	1.000	[95]
cis-1,2-dimethylcyclohexane*	1040	1250	0.998	[97]
trans-1,2-dimethylcyclohexane*	1010	1270	0.998	[97]
cycloheptane*	1070	1210	1.000	[97]
cyclooctane	1080	1300	1.000	[98]
cyclohexene*	1080	1170	0.999	[97]
trans-decalin*	1090	1440	1.000	[97]
cis-decalin*	1120	1460	1.000	[97]

Table B1 cont.

Liquid	ρ^*(kg/m^3)	T^*(K)	R^2	Model/ Data source
tetralin*	1210	1480	1.000	[97]
benzene	1200	1100	1.000	[95]
toluene	1140	1210	1.000	[95]
ethylbenzene*	1120	1290	1.000	[97]
o-xylene	1140	1290	1.000	[98]
m-xylene	1120	1290	1.000	[98]
p-xylene	1130	1240	1.000	[98]
fluorobenzene*	1380	1140	1.000	[97]
chlorobenzene*	1430	1290	1.000	[97]
bromobenzene	1900	1370	1.000	[98]
phenol*	1350	1460	1.000	[97]
phenanthrene*	1340	1800	0.9901	[97]
chloromethane*	1398	909.0	0.9981	[97]
dichloromethane*	1850	1033	1.0000	[97]
chloroform*	2070	1045	0.9989	[97]
carbon tetrachloride*	2165	1110	1.0000	[97]
chloroethane*	1280	980	0.999	[97]
1,1 dichloroethane*	1620	1060	0.999	[97]
1,2 dichloroethane*	1690	1140	1.000	[97]
1,1,1 trichloroethane	1820	1100	0.998	[97]
1-chlorobutane*	1190	1150	0.998	[97]
1-chlorohexane	1160	1200	1.000	[98]
1-chlorohexadecane*	1080	1500	0.999	[97]
1,1 dichloroethylene*	1710	1010	0.997	[97]
trans-1,2-dichloroethene*	1750	1040	0.998	[97]
cis-1,2-dichloroethene*	1740	1120	1.000	[97]
trichloroethylene*	1920	1220	0.997	[97]
fluoromethane	1268	639.4	0.9998	[95]
difluoromethane	1775	703.0	0.9997	[95]
trifluoromethane	2118	605.3	0.9996	[95]
carbon tetrafluoride	2341	461.3	0.9999	[95]
perfluoroethane	2430	573	1.000	[95]
perfluoropropane	2450	692	1.000	[95]
perfluorobutane	2340	857	0.999	[95]
perfluoropentane	2520	836	0.995	[95]
perflurorhexane*	2500	895	0.998	[97]

Table B1 cont.

Liquid	ρ^*(kg/m^3)	T^*(K)	R^2	Model/ Data source
perflurorhexane*	2500	895	0.998	[97]
perfluoroheptane*	2490	953	0.998	[97]
perfluorooctane*	2550	957	0.999	[97]
perfluorononane*	2490	1040	0.997	[97]
perfluorodecane*	2520	1090	0.997	[97]
acetone	1106	1025	0.9999	[95]
methyl ethyl ketone*	1102	1083	0.9993	[97]
vinyl methyl ketone*	1140	1130	0.998	[97]
diethyl ketone*	1110	1110	1.000	[97]
ethyl vinyl ketone*	1110	1210	0.999	[97]
ethyl propyl ketone*	1080	1190	0.998	[97]
dimethyl ether*	1050	838	1.000	[95]
diethyl ether*	1030	963	0.999	[97]
divinyl ether*	1100	988	0.999	[97]
tetrahydrofuran*	1180	1200	0.996	[97]
1,4-dioxane*	1370	1190	1.000	[97]
methyl formate*	1390	974	1.000	[97]
acetic acid*	1380	1220	1.000	[97]
methyl acetate*	1290	1070	0.998	[97]
ethyl acetate*	1250	1040	1.000	[97]
propyl acetate*	1210	1100	1.000	[97]
n-butyl acetate*	1180	1150	0.994	[97]
propyl propionate*	1190	1120	1.000	[97]
methanol	1072	1119	0.9999	[95]
ethanol	1040	1210	0.999	[95]
1-propanol	1040	1300	0.999	[98]
isopropanol	1020	1260	0.995	[98]
1-butanol	1040	1330	0.999	[98]
tert-butanol*	1110	1010	1.000	[97]
1-hexanol*	1040	1350	0.998	[97]
ammonia	959.4	831.2	0.9996	[95]
triethylamine*	984	1120	0.999	[97]
nitromethane*	1540	1130	1.000	[97]
aniline*	1290	1430	1.000	[97]
β-picoline*	1230	1320	1.000	[97]
γ-picoline*	1220	1330	1.000	[97]

Table B1 cont.

Liquid	ρ^*(kg/m^3)	T^*(K)	R^2	Model/ Data source
2,6-dimethylpyridine*	1200	1280	0.998	[97]
n-palmitic acid*	1110	1480	0.997	[97]
n-stearic acid*	1110	1480	0.997	[97]
Polymer melts				
polystyrene	1213	2377	1.000	[99]
poly(o-methylstyrene)	1201	2327	1.000	[99]
poly(vinyl acetate)	1438.7	1729.2	0.99997	[100]
poly(methyl methacrylate)	1400	2185	0.9998	[96]
poly(cyclohexyl methacrylate)	1319	2051	0.9994	[96]
poly(n-butyl methacrylate)	1265	1807	0.9999	[96]
branched polyethylene	1020	1798	0.9970	[96]
linear polyethylene	1038	1726	0.9997	[96]
high MW linear polyethylene	1051	1618	0.9996	[96]
poly(isobutylene)	1067.0	2121.2	0.99997	[101]
poly(dimethylsiloxane)	1218.3	1456.3	0.99981	[102]
poly(4-methyl- 1-pentene)	982.12	1923.7	0.99613	[103]
poly(tetrafluoroethylene)	2907.1	1311.9	0.99840	[104]
poly(epichlorohydrin)	1592	2090	0.9999	[49]
poly (c-caprolactone)	1280	1962	0.9992	[49]
poly(vinyl chloride)	1633	2173	0.9975	[49]
atactic-polypropylene	1050	1669	0.9956	[49]

Table B1 cont.

Appendix C: SPT Equation of State Parameters*

In the high density limit (or the high temperature limit) the QCSW model behaves structurally like a HS fluid. In this limit, $\langle n \rangle$ can be approximated as the number of HS centers between σ and $\lambda\sigma$ of a given central sphere. Using the pair distribution function $g(r/\sigma)$, $\langle n \rangle$ may be calculated for a HS fluid through:

$$\langle n \rangle = 4\pi\rho\sigma^3 \int_1^{\lambda} (r/\sigma)^2 g(r/\sigma;\eta) d(r/\sigma) \qquad \text{(C1)}$$

Tabulated values of $g(r;\rho)$ are available in the literature[152] as a function of r/σ at selected values of $\rho\sigma^3 = 6\eta/\pi$, and $g(1;\eta)$ may be approximated through the Percus-Yevick radial distribution function at contact for the HS fluid[48].

$$g(1,\eta) = \frac{1+\frac{1}{2}\eta}{(1-\eta)^2} \qquad \text{(C2)}$$

The integral (C2) was evaluated numerically with a simple trapezoid integration for $\lambda = 3/2$ at four different η in Table C1. At $\eta = 0.484$, the largest η given, the calculated coordination number of 12.6 is in good agreement with the approximate $n_{\max} = 12$.

η	0.340	0.393	0.445	0.484
$\langle n \rangle$	9.0	10.5	11.8	12.6

Table C1: Average number of hard spheres with centers between a distance σ and $3\lambda\sigma/2$ of a central sphere in a HS fluid

* This material was published as Appendix in: Isaac C. Sanchez, and Sean O'Keefe, "Theoretical Rationale for a Thermodynamic Glass State" *J. Phys. Chem. B* 120 (35), 9443 (2016)[125]. Sean Patrick O'Keefe performed the calculations that appear in this appendix both in the article and in the present dissertation.

References

[1] I.C. Sanchez, Dimensionless Thermodynamics: A New Paradigm for Liquid State Properties, J. Phys. Chem. B. 118 (2014) 9386–9397. doi:10.1021/jp504140z.

[2] I.C. Sanchez, T.M. Truskett, P.J. in 't Veld, Configurational Properties and Corresponding States in Simple Fluids and Water, J. Phys. Chem. B. 103 (1999) 5106–5116. doi:10.1021/jp9904668.

[3] E.W. Lemmon, M.O. McLinden, D.G. Friend, Thermophysical properties of fluid systems, NIST Chem. Webbook NIST Stand. Ref. Database. 69 (2005).

[4] A. Ben-Naim, Solvation Thermodynamics, Springer Science & Business Media, 2013.

[5] B. Guillot, Y. Guissani, A computer simulation study of the temperature dependence of the hydrophobic hydration, J. Chem. Phys. 99 (1993) 8075–8094. doi:10.1063/1.465634.

[6] M.T. Stone, P.J. in 't Veld, Y. Lu, I.C. Sanchez, Hydrophobic/hydrophilic solvation: inferences from Monte Carlo simulations and experiments, Mol. Phys. 100 (2002) 2773–2792. doi:10.1080/00268970210139912.

[7] I.C. Sanchez, K.L. Boening, Universal Thermodynamics at the Liquid–Vapor Critical Point, J. Phys. Chem. B. 118 (2014) 13704–13710. doi:10.1021/jp510096e.

[8] J.W. Cahn, J.E. Hilliard, Free Energy of a Nonuniform System. I. Interfacial Free Energy, J. Chem. Phys. 28 (1958) 258–267. doi:10.1063/1.1744102.

[9] C.I. Poser, I.C. Sanchez, Interfacial tension theory of low and high molecular weight liquid mixtures, Macromolecules. 14 (1981) 361–370. doi:10.1021/ma50003a026.

[10] H. Reiss, H.L. Frisch, J.L. Lebowitz, Statistical Mechanics of Rigid Spheres, J. Chem. Phys. 31 (1959) 369–380. doi:10.1063/1.1730361.

[11] M.S. Wertheim, Exact Solution of the Percus-Yevick Integral Equation for Hard Spheres, Phys. Rev. Lett. 10 (1963) 321–323. doi:10.1103/PhysRevLett.10.321.

[12] J.K. Johnson, J.A. Zollweg, K.E. Gubbins, The Lennard-Jones equation of state revisited, Mol. Phys. 78 (1993) 591–618. doi:10.1080/00268979300100411.

[13] J. Kolafa, I. Nezbeda, The Lennard-Jones fluid: an accurate analytic and theoretically-based equation of state, Fluid Phase Equilibria. 100 (1994) 1–34. doi:10.1016/0378-3812(94)80001-4.

[14] G.S. Boltachev, V.G. Baidakov, Equation of State for Lennard-Jones Fluid, High Temp. 41 (2003) 270–272. doi:10.1023/A:1023394122000.

[15] P.A. Egelstaff, B. Widom, Liquid Surface Tension near the Triple Point, J. Chem. Phys. 53 (1970) 2667–2669. doi:10.1063/1.1674388.

[16] S.P. O'Keefe, I.C. Sanchez, Scaled Particle Theory of solutions: Comparison with Lattice Fluid model, Fluid Phase Equilibria. 433 (2017) 67–78. doi:10.1016/j.fluid.2016.11.014.

[17] I.C. Sanchez, R.H. Lacombe, An elementary molecular theory of classical fluids. Pure fluids, J. Phys. Chem. 80 (1976) 2352–2362. doi:10.1021/j100562a008.

[18] R.H. Lacombe, I.C. Sanchez, Statistical thermodynamics of fluid mixtures, J. Phys. Chem. 80 (1976) 2568–2580. doi:10.1021/j100564a009.

[19] I.C. Sanchez, R.H. Lacombe, Statistical Thermodynamics of Polymer Solutions, Macromolecules. 11 (1978) 1145–1156. doi:10.1021/ma60066a017.

[20] J. Chmelař, K. Smolná, K. Haškovcová, M. Podivinská, J. Maršálek, J. Kosek, Equilibrium sorption of ethylene in polyethylene: Experimental study and PC-SAFT simulations, Polymer. 59 (2015) 270–277. doi:10.1016/j.polymer.2015.01.012.

[21] M. Galizia, Z.P. Smith, G.C. Sarti, B.D. Freeman, D.R. Paul, Predictive calculation of hydrogen and helium solubility in glassy and rubbery polymers, J. Membr. Sci. 475 (2015) 110–121. doi:10.1016/j.memsci.2014.10.009.
[22] S.J. Alesaadi, F. Sabzi, Hydrogen storage in a series of Zn-based MOFs studied by Sanchez–Lacombe equation of state, Int. J. Hydrog. Energy. 40 (2015) 1651–1656. doi:10.1016/j.ijhydene.2014.12.008.
[23] A. Noorjahan, P. Choi, Prediction of self diffusion coefficients of selected solvents in poly(vinyl alcohol) using lattice-free volume theory, Polymer. 58 (2015) 53–59. doi:10.1016/j.polymer.2014.12.023.
[24] L. Sun, H. Zhao, S.B. Kiselev, C. McCabe, Predicting Mixture Phase Equilibria and Critical Behavior Using the SAFT-VRX Approach, J. Phys. Chem. B. 109 (2005) 9047–9058. doi:10.1021/jp044413o.
[25] M.J. Pratas de Melo, A.M.A. Dias, M. Blesic, L.P.N. Rebelo, L.F. Vega, J.A.P. Coutinho, I.M. Marrucho, Liquid–liquid equilibrium of (perfluoroalkane + alkane) binary mixtures, Fluid Phase Equilibria. 242 (2006) 210–219. doi:10.1016/j.fluid.2006.02.003.
[26] K.S. Schweizer, J.G. Curro, Integral Equation Theories of the Structure, Thermodynamics, and Phase Transitions of Polymer Fluids, in: I. Prigogine, S.A. Rice (Eds.), Adv. Chem. Phys., John Wiley & Sons, Inc., 1997: pp. 1–142.
[27] J. Dudowicz, K.F. Freed, Effect of monomer structure and compressibility on the properties of multicomponent polymer blends and solutions: 1. Lattice cluster theory of compressible systems, Macromolecules. 24 (1991) 5076–5095. doi:10.1021/ma00018a014.
[28] S.H. Huang, M. Radosz, Equation of state for small, large, polydisperse, and associating molecules, Ind. Eng. Chem. Res. 29 (1990) 2284–2294. doi:10.1021/ie00107a014.
[29] W.G. Chapman, K.E. Gubbins, G. Jackson, M. Radosz, New reference equation of state for associating liquids, Ind. Eng. Chem. Res. 29 (1990) 1709–1721. doi:10.1021/ie00104a021.
[30] J.G. Curro, A. Yethiraj, K.S. Schweizer, J.D. McCoy, K.G. Honnell, Microscopic equations-of-state for hydrocarbon fluids: effect of attractions and comparison with polyethylene experiments, Macromolecules. 26 (1993) 2655–2662. doi:10.1021/ma00063a002.
[31] J.L. Lebowitz, E. Helfand, E. Praestgaard, Scaled Particle Theory of Fluid Mixtures, J. Chem. Phys. 43 (1965) 774–779. doi:10.1063/1.1696842.
[32] B. Widom, Potential-distribution theory and the statistical mechanics of fluids, J. Phys. Chem. 86 (1982) 869–872. doi:10.1021/j100395a005.
[33] I.C. Sanchez, Volume fluctuation thermodynamics of polymer solutions, Macromolecules. 24 (1991) 908–916. doi:10.1021/ma00004a016.
[34] R.M. Masegosa, M.G. Prolongo, A. Horta, The g interaction parameter of polymer-solvent systems, Macromolecules. 19 (1986) 1478–1486. doi:10.1021/ma00159a033.
[35] I.C. Sanchez, P.A. Rodgers, Solubility of gases in polymers, Pure Appl. Chem. 62 (1990) 2107–2114. doi:10.1351/pac199062112107.
[36] P. Munk, T.M. Aminabhavi, Introduction to Macromolecular Science, 2 edition, Wiley-Interscience, New York, 2002.
[37] P. Munk, Z.Y. Al-Saigh, T.W. Card, Inverse gas chromatography. 3. Dependence of retention volume on the amount of probe injected, Macromolecules. 18 (1985) 2196–2201. doi:10.1021/ma00153a023.

[38] L.I. Stiel, D.F. Harnish, Solubility of gases and liquids in molten polystyrene, AIChE J. 22 (1976) 117–122. doi:10.1002/aic.690220114.
[39] Q. Du, P. Hattam, P. Munk, Inverse gas chromatography. 7. Polymer-solvent interactions of hydrocarbon polymers, J. Chem. Eng. Data. 35 (1990) 367–371. doi:10.1021/je00061a039.
[40] J. Chu, R.J. Getty, L.F. Brennecke, R. Paul, Distillation equilibrium data, Reinhold, New York, 1950.
[41] C.P. Brown, A.R. Mathieson, J.C.J. Thynne, Thermodynamics of hydrocarbon mixtures. Part I. The heats of mixing of the binary and ternary systems formed by benzene, cyclohexane, and n-heptane, J. Chem. Soc. Resumed. (1955) 4141–4146. doi:10.1039/JR9550004141.
[42] A.R. Mathieson, J.C.J. Thynne, 720. Thermodynamics of hydrocarbon mixtures. Part II. The heats of mixing of the binary mixtures formed by benzene, cyclohexane, n-heptane, toluene, and n-hexane, J. Chem. Soc. Resumed. (1956) 3708–3713. doi:10.1039/JR9560003708.
[43] A.R. Mathieson, J.C.J. Thynne, 721. Thermodynamics of hydrocarbon mixtures. Part III. The heats of mixing of ternary, quaternary, and quinary mixtures formed by benzene, cyclohexane, heptane, toluene, and hexane, J. Chem. Soc. Resumed. (1956) 3713–3716. doi:10.1039/JR9560003713.
[44] A.W. Francis, Critical solution temperatures, American Chemical Society, 1961. http://pubs.acs.org/doi/book/10.1021/ba-1961-0031 (accessed May 9, 2016).
[45] L.H. Horsley, Table of Azeotropes and Nonazeotropes, Anal. Chem. 19 (1947) 508–600. doi:10.1021/ac60008a002.
[46] D.F. Othmer, S.A. Savitt, Composition of Vapors from Boiling Binary Solutions, Ind. Eng. Chem. 40 (1948) 168–174. doi:10.1021/ie50457a042.
[47] P.I. Freeman, J.S. Rowlinson, Lower critical points in polymer solutions, Polymer. 1 (1960) 20–26. doi:10.1016/0032-3861(60)90004-5.
[48] J.L. Lebowitz, Exact Solution of Generalized Percus-Yevick Equation for a Mixture of Hard Spheres, Phys. Rev. 133 (1964) A895–A899. doi:10.1103/PhysRev.133.A895.
[49] P.A. Rodgers, Pressure–volume–temperature relationships for polymeric liquids: A review of equations of state and their characteristic parameters for 56 polymers, J. Appl. Polym. Sci. 48 (1993) 1061–1080. doi:10.1002/app.1993.070480613.
[50] W.-C. Hu, Monte Carlo Simulations of Model Molecular and Polymer Fluids, Ph.D. Dissertation, The University of Texas at Austin, 1994.
[51] A. Santos, S.B. Yuste, M.L. de Haro, Equation of state of a multicomponent d-dimensional hard-sphere fluid, Mol. Phys. 96 (1999) 1–5. doi:10.1080/00268979909482932.
[52] N.F. Carnahan, K.E. Starling, Equation of state for nonattracting rigid spheres, J. Chem. Phys. 51 (1969) 635–636.
[53] A. Malijevský, J. Veverka, New equations of state for pure and binary hard-sphere fluids, Phys. Chem. Chem. Phys. 1 (1999) 4267–4270. doi:10.1039/A902831E.
[54] T. Boublík, Hard-Sphere Equation of State, J. Chem. Phys. 53 (1970) 471–472.
[55] G.A. Mansoori, N.F. Carnahan, K.E. Starling, T.W. Leland Jr, Equilibrium thermodynamic properties of the mixture of hard spheres, J. Chem. Phys. 54 (1971) 1523–1525.
[56] T. Kihara, K. Miyoshi, Geometry of three convex bodies applicable to three-molecule clusters in polyatomic gases, J. Stat. Phys. 13 (1975) 337–345. doi:10.1007/BF01012012.

[57] T. Coussaert, M. Baus, Demixing vs freezing of binary hard-sphere mixtures, J. Chem. Phys. 109 (1998) 6012–6020.
[58] F. Saija, G. Fiumara, P.V. Giaquinta, Fourth virial coefficient of hard-body mixtures in two and three dimensions, Mol. Phys. 87 (1996) 991–998. doi:10.1080/00268979600100671.
[59] M. Barošová, M. Malijevský, S. Labík, W.R. Smith, Computer simulation of the chemical potentials of binary hard-sphere mixtures, Mol. Phys. 87 (1996) 423–439. doi:10.1080/00268979600100281.
[60] L.E. de Souza, A. Stamatopoulou, D. Ben-Amotz, Chemical potentials of hard sphere solutes in hard sphere solvents. Monte Carlo simulations and analytical approximations, J. Chem. Phys. 100 (1994) 1456–1459.
[61] A.O. Malakhov, E.B. Brun, Multicomponent hard-sphere heterochain fluid: equations of state in a continuum space, Macromolecules. 25 (1992) 6262–6269. doi:10.1021/ma00049a024.
[62] Y.C. Chiew, Percus-Yevick integral-equation theory for athermal hard-sphere chains, Mol. Phys. 70 (1990) 129–143. doi:10.1080/00268979000100891.
[63] R.J. Baxter, Percus–Yevick Equation for Hard Spheres with Surface Adhesion, J. Chem. Phys. 49 (1968) 2770–2774. doi:10.1063/1.1670482.
[64] Y. Song, S.M. Lambert, J.M. Prausnitz, Equation of state for mixtures of hard-sphere chains including copolymers, Macromolecules. 27 (1994) 441–448. doi:10.1021/ma00080a018.
[65] W.G. Chapman, G. Jackson, K.E. Gubbins, Phase equilibria of associating fluids, Mol. Phys. 65 (1988) 1057–1079. doi:10.1080/00268978800101601.
[66] I.C. Sanchez, S. O'Keefe, J.F. Xu, New Zeno-Like Liquid States, J. Phys. Chem. B. 120 (2016) 3705–3712. doi:10.1021/acs.jpcb.6b01364.
[67] J.G. Powles, The Boyle line, J. Phys. C Solid State Phys. 16 (1983) 503. doi:10.1088/0022-3719/16/3/012.
[68] A. Batschinski, Abhandlungen über Zustandsgleichung; Abh. I: Der orthometrische Zustand, Ann. Phys. 324 (1906) 307–309. doi:10.1002/andp.19063240205.
[69] J. Xu, D.R. Herschbach, Correlation of Zeno line with acentric factor and other properties of normal fluids, J. Phys. Chem. 96 (1992) 2307–2312. doi:10.1021/j100184a053.
[70] D. Ben-Amotz, D.R. Herschbach, Correlation of Zeno (Z = 1) Line for Supercritical Fluids with Vapor-Liquid Rectilinear Diameters, Isr. J. Chem. 30 (1990) 59–68. doi:10.1002/ijch.199000007.
[71] E.M. Holleran, Linear relation of temperature and density at unit compressibility factor, J. Chem. Phys. 47 (1967) 5318–5324.
[72] L. Cailletet, E. Mathias, Recherches sur les densités des gaz liquéfiés et de leurs vapeurs saturées, J Phys Theor Appl. 5 (1886) 549–564. doi:10.1051/jphystap:018860050054900.
[73] J.J. van Laar, Über eine einfache Formel zur Bestimmung der kritischen Temperatur aus dem Ausdehnungskoeffizient in der flüssigen Phase, und die Ursache ihrer Nichtanwendbarkeit bei vielen geschmolzenen Salzen, Z. Für Anorg. Allg. Chem. 146 (1925) 263–280. doi:10.1002/zaac.19251460119.
[74] J.A. Zollweg, G.W. Mulholland, On the Law of the Rectilinear Diameter, J. Chem. Phys. 57 (1972) 1021–1025. doi:10.1063/1.1678352.
[75] P.M. Nasch, S.G. Steinemann, Density and Thermal Expansion of Molten Manganese, Iron, Nickel, Copper, Aluminum and Tin by Means of the Gamma-Ray Attenuation Technique, Phys. Chem. Liq. 29 (1995) 43–58. doi:10.1080/00319109508030263.

[76] G.J. Janz, Molten Salts Handbook, Academic Press, 1967.
[77] J. Brillo, I. Egry, Density Determination of Liquid Copper, Nickel, and Their Alloys, Int. J. Thermophys. 24 (2003) 1155–1170. doi:10.1023/A:1025021521945.
[78] J. Brillo, I. Egry, I. Ho, Density and Thermal Expansion of Liquid Ag–Cu and Ag–Au Alloys, Int. J. Thermophys. 27 (2006) 494–506. doi:10.1007/s10765-005-0011-4.
[79] W. Gąsior, Z. Moser, J. Pstruś, Density and surface tension of the Pb-Sn liquid alloys, J. Phase Equilibria. 22 (2001) 20. doi:10.1007/s11669-001-0051-9.
[80] S. Gruner, M. Köhler, W. Hoyer, Surface tension and mass density of liquid Cu–Ge alloys, J. Alloys Compd. 482 (2009) 335–338. doi:10.1016/j.jallcom.2009.04.005.
[81] L. Fang, F. Xiao, Y.F. Wang, Z.N. Tao, K. MuKai, Density and molar volume of liquid Ni–Co binary alloys, Mater. Sci. Eng. B. 132 (2006) 174–178. doi:10.1016/j.mseb.2006.02.015.
[82] I.C. Sanchez, J. Cho, A universal equation of state for polymer liquids, Polymer. 36 (1995) 2929–2939. doi:10.1016/0032-3861(95)94342-Q.
[83] E.M. Apfelbaum, V.S. Vorob'ev, G.A. Martynov, Triangle of Liquid−Gas States, J. Phys. Chem. B. 110 (2006) 8474–8480. doi:10.1021/jp057327c.
[84] D.S. Gates, G. Thodos, The critical constants of the elements, AIChE J. 6 (1960) 50–54. doi:10.1002/aic.690060110.
[85] I.G. Dillon, P.A. Nelson, B.S. Swanson, Measurement of Densities and Estimation of Critical Properties of the Alkali Metals, J. Chem. Phys. 44 (1966) 4229–4238. doi:10.1063/1.1726611.
[86] S. Jüngst, B. Knuth, F. Hensel, Observation of Singular Diameters in the Coexistence Curves of Metals, Phys. Rev. Lett. 55 (1985) 2160–2163. doi:10.1103/PhysRevLett.55.2160.
[87] V. Morel, A. Bultel, B.G. Chéron, The Critical Temperature of Aluminum, Int. J. Thermophys. 30 (2009) 1853. doi:10.1007/s10765-009-0671-6.
[88] P.J. McGonigal, A.D. Kirshenbaum, A.V. Grosse, THE LIQUID TEMPERATURE RANGE, DENSITY, AND CRITICAL CONSTANTS OF MAGNESIUM1, J. Phys. Chem. 66 (1962) 737–740. doi:10.1021/j100810a038.
[89] E.M. Holleran, Interrelation of the virial coefficients, J. Chem. Phys. 49 (1968) 39–43.
[90] A. Boushehri, F.M. Tao, E.A. Mason, Common bulk modulus point for compressed liquids, J. Phys. Chem. 97 (1993) 2711–2714. doi:10.1021/j100113a037.
[91] A.A. Bondi, Physical properties of molecular crystals liquids, and glasses, (1968).
[92] E.A. Spiegel, G. Veronis, On the Boussinesq Approximation for a Compressible Fluid., Astrophys. J. 131 (1960) 442. doi:10.1086/146849.
[93] J.M. Mihaljan, A Rigorous Exposition of the Boussinesq Approximations Applicable to a Thin Layer of Fluid., Astrophys. J. 136 (1962) 1126. doi:10.1086/147463.
[94] D.D. Gray, A. Giorgini, The validity of the boussinesq approximation for liquids and gases, Int. J. Heat Mass Transf. 19 (1976) 545–551. doi:10.1016/0017-9310(76)90168-X.
[95] E.W. Lemmon, M.L. Huber, M.O. McLinden, REFPROP: Reference fluid thermodynamic and transport properties, NIST Stand. Ref. Database. 23 (2013).
[96] O. Olabisi, R. Simha, Pressure-Volume-Temperature Studies of Amorphous and Crystallizable Polymers. I. Experimental, Macromolecules. 8 (1975) 206–210. doi:10.1021/ma60044a022.
[97] M. Frenkel, R.D. Chirico, V. Diky, X. Yan, Q. Dong, C. Muzny, ThermoData Engine (TDE): Software Implementation of the Dynamic Data Evaluation Concept, J. Chem. Inf. Model. 45 (2005) 816–838. doi:10.1021/ci050067b.

[98] J.H. Dymond, R. Malhotra, The Tait equation: 100 years on, Int. J. Thermophys. 9 (1988) 941–951. doi:10.1007/BF01133262.
[99] A. Quach, R. Simha, Pressure-Volume-Temperature Properties and Transitions of Amorphous Polymers; Polystyrene and Poly (orthomethylstyrene), J. Appl. Phys. 42 (1971) 4592–4606. doi:10.1063/1.1659828.
[100] J.E. McKinney, M. Goldstein, PVT relationships for liquid and glassy poly (vinyl acetate), J. Res. Natl. Bur. Stand. Sect. A. 78 (1974) 331.
[101] B.E. Eichinger, P.J. Flory, Determination of the Equation of State of Polyisobutylene, Macromolecules. 1 (1968) 285–286. doi:10.1021/ma60003a016.
[102] H. Shih, P.J. Flory, Equation-of-State Parameters for Poly(dimethylsiloxane), Macromolecules. 5 (1972) 758–761. doi:10.1021/ma60030a018.
[103] P. Zoller, The specific volume of poly(4-methylpentene-1) as a function of temperature (30°–320°C) and pressure (0–2000 kg/cm2), J. Appl. Polym. Sci. 21 (1977) 3129–3137. doi:10.1002/app.1977.070211123.
[104] P. Zoller, The specific volume of poly(tetrafluoroethylene) as a function of temperature (30°–372°C) and pressure (0–2000 kg/cm2), J. Appl. Polym. Sci. 22 (1978) 633–641. doi:10.1002/app.1978.070220305.
[105] H.G. Rackett, Equation of state for saturated liquids, J. Chem. Eng. Data. 15 (1970) 514–517. doi:10.1021/je60047a012.
[106] T. Takagi, H. Teranishi, Third International Conference on Thermodynamics of Solutions of Nonelectrolytes held at Universit'e de Clermont-Ferrand 2Ultrasonic speeds and thermodynamics for binary solutions of n-alkanes under high pressures, Fluid Phase Equilibria. 20 (1985) 315–320. doi:10.1016/0378-3812(85)90050-0.
[107] D. Pečar, V. Doleček, Isothermal compressibilities and isobaric expansibilities of pentane, hexane, heptane and their binary and ternary mixtures from density measurements, Fluid Phase Equilibria. 211 (2003) 109–127. doi:10.1016/S0378-3812(03)00154-7.
[108] J.H. Dymond, J. Robertson, J.D. Isdale, (p, ρ, T) of some pure n-alkanes and binary mixtures of n-alkanes in the range 298 to 373 K and 0.1 to 500 MPa, J. Chem. Thermodyn. 14 (1982) 51–59. doi:10.1016/0021-9614(82)90123-9.
[109] M. Ramos-Estrada, G.A. Iglesias-Silva, K.R. Hall, Experimental measurements and prediction of liquid densities for n-alkane mixtures, J. Chem. Thermodyn. 38 (2006) 337–347. doi:10.1016/j.jct.2005.05.020.
[110] R. Malhotra, L.A. Woolf, Volumetric measurements under pressure for 2,2,4-trimethylpentane at temperatures up to 353.15 K and for benzene and three of their mixtures at temperatures up to 348.15 K, Int. J. Thermophys. 14 (1993) 1153–1172. doi:10.1007/BF02431281.
[111] S.A. Beg, N.M. Tukur, D.K. Al-Harbi, E.Z. Hamad, Densities and Excess Volumes of Benzene + Hexane between 298.15 and 473.15 K, J. Chem. Eng. Data. 40 (1995) 74–78. doi:10.1021/je00017a016.
[112] P.J. Petrino, Y.H. Gaston-Bonhomme, J.L.E. Chevalier, Viscosity and Density of Binary Liquid Mixtures of Hydrocarbons, Esters, Ketones, and Normal Chloroalkanes, J. Chem. Eng. Data. 40 (1995) 136–140. doi:10.1021/je00017a031.
[113] J.L.E. Chevalier, P.J. Petrino, Y.H. Gaston-Bonhomme, Viscosity and density of some aliphatic, cyclic, and aromatic hydrocarbons binary liquid mixtures, J. Chem. Eng. Data. 35 (1990) 206–212. doi:10.1021/je00060a034.
[114] P.J. Flory, J.L. Ellenson, B.E. Eichinger, Thermodynamics of Mixing of n-Alkanes with Polyisobutylene, Macromolecules. 1 (1968) 279–284. doi:10.1021/ma60003a015.

[115] M. Aalto, K.I. Keskinen, J. Aittamaa, S. Liukkonen, An improved correlation for compressed liquid densities of hydrocarbons. Part 2. Mixtures, Fluid Phase Equilibria. 114 (1996) 21–35. doi:10.1016/0378-3812(95)02824-2.
[116] R.W. Hankinson, G.H. Thomson, A new correlation for saturated densities of liquids and their mixtures, AIChE J. 25 (1979) 653–663. doi:10.1002/aic.690250412.
[117] P.L. Chueh, J.M. Prausnitz, Vapor-liquid equilibria at high pressures: Calculation of partial molar volumes in nonpolar liquid mixtures, AIChE J. 13 (1967) 1099–1107. doi:10.1002/aic.690130612.
[118] W. Kay, Gases and Vapors At High Temperature and Pressure - Density of Hydrocarbon, Ind. Eng. Chem. 28 (1936) 1014–1019. doi:10.1021/ie50321a008.
[119] C.C. Li, Critical temperature estimation for simple mixtures, Can. J. Chem. Eng. 49 (1971) 709–710. doi:10.1002/cjce.5450490529.
[120] A.K. Doolittle, Studies in Newtonian Flow. II. The Dependence of the Viscosity of Liquids on Free-Space, J. Appl. Phys. 22 (1951) 1471–1475. doi:10.1063/1.1699894.
[121] N.R. Horn, A critical review of free volume and occupied volume calculation methods, J. Membr. Sci. 518 (2016) 289–294. doi:10.1016/j.memsci.2016.07.014.
[122] I.C. Sanchez, Towards a theory of viscosity for glass-forming liquids, J. Appl. Phys. 45 (1974) 4204–4215. doi:10.1063/1.1663037.
[123] M.H. Cohen, D. Turnbull, Molecular Transport in Liquids and Glasses, J. Chem. Phys. 31 (1959) 1164–1169. doi:10.1063/1.1730566.
[124] S. Sugden, CCXXXIII.—Molecular volumes at absolute zero. Part I. Density as a function of temperature, J. Chem. Soc. Resumed. (1927) 1780–1785. doi:10.1039/JR9270001780.
[125] I.C. Sanchez, S.P. O'Keefe, Theoretical Rationale for a Thermodynamic Glass State, J. Phys. Chem. B. 120 (2016) 9443–9449. doi:10.1021/acs.jpcb.6b06653.
[126] A.P. Mathews, The Relation of Molecular Cohesion to Surface Tension and Gravitation; a Method of Determining "a" of van der Waals' Equation without Assumptions; and the Explanation of the Meaning of the Constants in the Surface Tension Law of Eötvös, and the Latent Heat Formulas of Dieterici and Mills, J. Phys. Chem. 20 (1915) 554–596. doi:10.1021/j150169a002.
[127] W.M. Lee, Selection of barrier materials from molecular structure, Polym. Eng. Sci. 20 (1980) 65–69. doi:10.1002/pen.760200111.
[128] A. Bondi, van der Waals Volumes and Radii, J. Phys. Chem. 68 (1964) 441–451. doi:10.1021/j100785a001.
[129] D.W. Van Krevelen, K. Te Nijenhuis, Properties of polymers: their correlation with chemical structure; their numerical estimation and prediction from additive group contributions, Elsevier, 2009.
[130] Y. Maeda, D.R. Paul, Effect of antiplasticization on gas sorption and transport. III. Free volume interpretation, J. Polym. Sci. Part B Polym. Phys. 25 (1987) 1005–1016. doi:10.1002/polb.1987.090250503.
[131] J.S. Vrentas, J.L. Duda, Diffusion in polymer–solvent systems. II. A predictive theory for the dependence of diffusion coefficients on temperature, concentration, and molecular weight, J. Polym. Sci. Polym. Phys. Ed. 15 (1977) 417–439. doi:10.1002/pol.1977.180150303.
[132] M.L. Williams, R.F. Landel, J.D. Ferry, The Temperature Dependence of Relaxation Mechanisms in Amorphous Polymers and Other Glass-forming Liquids, J. Am. Chem. Soc. 77 (1955) 3701–3707. doi:10.1021/ja01619a008.

[133] P.B. Macedo, T.A. Litovitz, On the Relative Roles of Free Volume and Activation Energy in the Viscosity of Liquids, J. Chem. Phys. 42 (1965) 245–256. doi:10.1063/1.1695683.
[134] J.S. Vrentas, J.L. Duda, Diffusion in polymer—solvent systems. I. Reexamination of the free-volume theory, J. Polym. Sci. Polym. Phys. Ed. 15 (1977) 403–416. doi:10.1002/pol.1977.180150302.
[135] K.K. Innes, L. Albright, Effect of Temperature and Solute Volume on Liquid Diffusion Coefficients, Ind. Eng. Chem. 49 (1957) 1793–1794. doi:10.1021/ie50574a051.
[136] D.W. McCall, D.C. Douglass, E.W. Anderson, Self-Diffusion in Liquids: Paraffin Hydrocarbons, Phys. Fluids 1958-1988. 2 (1959) 87–91. doi:10.1063/1.1724398.
[137] J. Langer, The mysterious glass transition, Phys. Today. 60 (2007) 8–9. doi:10.1063/1.2711621.
[138] L. Berthier, M. Ediger, Facets of glass physics, Phys. Today. 69 (2015) 40–46. doi:10.1063/PT.3.3052.
[139] L. Berthier, G. Biroli, Theoretical perspective on the glass transition and amorphous materials, Rev. Mod. Phys. 83 (2011) 587–645. doi:10.1103/RevModPhys.83.587.
[140] W. Kauzmann, The Nature of the Glassy State and the Behavior of Liquids at Low Temperatures., Chem. Rev. 43 (1948) 219–256. doi:10.1021/cr60135a002.
[141] P.G. Debenedetti, F.H. Stillinger, Supercooled liquids and the glass transition, Nature. 410 (2001) 259–267. doi:10.1038/35065704.
[142] J.H. Gibbs, E.A. DiMarzio, Nature of the glass transition and the glassy state, J. Chem. Phys. 28 (1958) 373–383.
[143] F.H. Stillinger, Supercooled liquids, glass transitions, and the Kauzmann paradox, J. Chem. Phys. 88 (1988) 7818–7825.
[144] M. Guo, W. Wang, H. Lu, Equations of state for pure and mixture square-well fluids. II. Equations of state, Fluid Phase Equilibria. 60 (1990) 221–237. doi:10.1016/0378-3812(90)85054-E.
[145] D.M. Heyes, Coordination number and equation of state of square-well and square-shoulder fluids: simulation and quasi-chemical model, J. Chem. Soc., Faraday Trans. 87 (1991) 3373–3377. doi:10.1039/FT9918703373.
[146] A. Haghtalab, S.H. Mazloumi, A new coordination number model for development of a square-well equation of state, Fluid Phase Equilibria. 280 (2009) 1–8. doi:10.1016/j.fluid.2009.02.019.
[147] K.-H. Lee, M. Lombardo, S.I. Sandler, The generalized van der Waals partition function. II. Application to the square-well fluid, Fluid Phase Equilibria. 21 (1985) 177–196. doi:10.1016/0378-3812(85)87001-1.
[148] R.J. Speedy, On the reproducibility of glasses, J. Chem. Phys. 100 (1994) 6684–6691.
[149] D. Henderson, O.H. Scalise, W.R. Smith, Monte Carlo calculations of the equation of state of the square-well fluid as a function of well width, J. Chem. Phys. 72 (1980) 2431–2438.
[150] K. Huang, Statistical Mechanics, 2nd, Ed. N. Y. John Wiley Sons. (1987).
[151] I.C. Sanchez, J.S. Lee, On the Asymptotic Properties of a Hard Sphere Fluid, J. Phys. Chem. B. 113 (2009) 15572–15580. doi:10.1021/jp901041b.
[152] J.A. Barker, D. Henderson, Theories of Liquids, Annu. Rev. Phys. Chem. 23 (1972) 439–484. doi:10.1146/annurev.pc.23.100172.002255.
[153] L. Vega, E. de Miguel, L.F. Rull, G. Jackson, I.A. McLure, Phase equilibria and critical behavior of square-well fluids of variable width by Gibbs ensemble Monte Carlo simulation, J. Chem. Phys. 96 (1992) 2296–2305.

[154] P. Orea, S. Varga, G. Odriozola, A heuristic rule for classification of classical fluids: Master curves for Mie, Yukawa and square-well potentials, Chem. Phys. Lett. 631–632 (2015) 26–29. doi:10.1016/j.cplett.2015.04.025.
[155] G. Orkoulas, M.E. Fisher, A.Z. Panagiotopoulos, Precise simulation of criticality in asymmetric fluids, Phys. Rev. E. 63 (2001) 051507. doi:10.1103/PhysRevE.63.051507.
[156] K.N. Khanna, A. Tewari, D.K. Dwivedee, A new coordination number model and heat capacity of square-well fluids of variable width, Fluid Phase Equilibria. 243 (2006) 101–106. doi:10.1016/j.fluid.2006.01.016.
[157] H. Liu, S. Garde, S. Kumar, Direct determination of phase behavior of square-well fluids, J. Chem. Phys. 123 (2005) 174505.
[158] W.G. Hoover, F.H. Ree, Melting transition and communal entropy for hard spheres, J. Chem. Phys. 49 (1968) 3609–3617.
[159] E.A. Mastny, J.J. de Pablo, Melting line of the Lennard-Jones system, infinite size, and full potential, J. Chem. Phys. 127 (2007) 104504.
[160] G. Adam, J.H. Gibbs, On the temperature dependence of cooperative relaxation properties in glass-forming liquids, J. Chem. Phys. 43 (1965) 139–146.
[161] J. Dudowicz, K.F. Freed, J.F. Douglas, Generalized entropy theory of polymer glass formation, Adv. Chem. Phys. 137 (2008) 125.
[162] S. Sastry, The relationship between fragility, configurational entropy and the potential energy landscape of glass-forming liquids : Abstract : Nature, Nature. 409 (2001) 164–167. doi:10.1038/35051524.
[163] J.H. Wu, Q. Jia, Thermodynamic universality of configurational entropy in glass-forming liquids, J. Alloys Compd. 692 (2017) 698–704. doi:10.1016/j.jallcom.2016.09.124.
[164] C. Song, P. Wang, H.A. Makse, A phase diagram for jammed matter, Nature. 453 (2008) 629–632. doi:10.1038/nature06981.
[165] W. Man, A. Donev, F.H. Stillinger, M.T. Sullivan, W.B. Russel, D. Heeger, S. Inati, S. Torquato, P.M. Chaikin, Experiments on Random Packings of Ellipsoids, Phys. Rev. Lett. 94 (2005) 198001. doi:10.1103/PhysRevLett.94.198001.
[166] M. Dzugutov, A universal scaling law for atomic diffusion in condensed matter, Nature. 381 (1996) 137–139. doi:10.1038/381137a0.
[167] J. Mittal, J.R. Errington, T.M. Truskett, Relationships between Self-Diffusivity, Packing Fraction, and Excess Entropy in Simple Bulk and Confined Fluids, J. Phys. Chem. B. 111 (2007) 10054–10063. doi:10.1021/jp071369e.
[168] E. Voyiatzis, F. Müller-Plathe, M.C. Böhm, Excess entropy scaling for the segmental and global dynamics of polyethylene melts, Phys. Chem. Chem. Phys. 16 (2014) 24301–24311. doi:10.1039/C4CP03559C.
[169] C.A. Angell, Relaxation in liquids, polymers and plastic crystals — strong/fragile patterns and problems, J. Non-Cryst. Solids. 131 (1991) 13–31. doi:10.1016/0022-3093(91)90266-9.
[170] K.L. Ngai, C.M. Roland, Chemical structure and intermolecular cooperativity: dielectric relaxation results, Macromolecules. 26 (1993) 6824–6830. doi:10.1021/ma00077a019.
[171] Q. Qin, G.B. McKenna, Correlation between dynamic fragility and glass transition temperature for different classes of glass forming liquids, J. Non-Cryst. Solids. 352 (2006) 2977–2985. doi:10.1016/j.jnoncrysol.2006.04.014.
[172] K. Kunal, C.G. Robertson, S. Pawlus, S.F. Hahn, A.P. Sokolov, Role of Chemical Structure in Fragility of Polymers: A Qualitative Picture, Macromolecules. 41 (2008) 7232–7238. doi:10.1021/ma801155c.

[173] A.P. Sokolov, V.N. Novikov, Y. Ding, Why many polymers are so fragile, J. Phys. Condens. Matter. 19 (2007) 205116. doi:10.1088/0953-8984/19/20/205116.
[174] G.C. Berry, T.G. Fox, The viscosity of polymers and their concentrated solutions, in: Fortschritte Hochpolym.-Forsch., Springer, Berlin, Heidelberg, 1968: pp. 261–357. doi:10.1007/BFb0050985.